TECHNISCHE
UNIVERSITÄT
WIEN
Vienna University of Technology

DISSERTATION

Magnetically Functionalized Star Polymers and Polymer Melts in MPCD Simulations

Ausgeführt zum Zwecke der Erlangung des akademischen Grades eines Doktors der technischen Wissenschaften, unter der Leitung von

Prof. Dr. Gerhard Kahl
Institut für Theoretische Physik (E136)

eingereicht an der Technischen Universität Wien,
Fakultät für Physik

von

David Toneian
(Matrikelnummer 00926125)

Wien, 2019-04-02

Unterschrift Student

Abstract

Star polymers are macromolecules which consist of a central core, to which a number of linear polymer chains are attached. In this work, the free ends of those polymer chains are decorated, or *functionalized*, with super-paramagnetic particles, the magnetic dipole moments of which are aligned with an external magnetic field.

In computer simulations, the resulting molecule is subjected to shear flows of varying strength, and the conformational properties, such as size and shape, as well as dynamic properties in the form of whole-body rotations, are studied as functions of the shear rate and the relative orientation of the shear flow direction with regard to the axis of the external magnetic field.

When these properties are compared to corresponding ones in the case of non-magnetic star polymers, one finds that some phenomena are largely unaffected by the introduction of magnetic moments, while others emerge, or behave qualitatively differently, due to the spontaneous self-assembly of columns of magnetic particles.

Further, this thesis contains new and improved results pertaining to the viscoelastic behavior of polymer melts, partly building on research carried out in the course of the author's *Diplomarbeit* (master's thesis).

In both topics, a hybrid simulation method of Multi-Particle Collision Dynamics (MPCD) and Molecular Dynamics (MD) is employed, using a simulation and data analysis package developed and published by the thesis author; a short description of said package is provided in this text.

Contents

Chapter 1

Introduction

1.1 Soft Matter

The overarching theme in this thesis is that of *soft matter*, sometimes referred to as *soft condensed matter*. While different authors give different definitions for these terms, the latter name reveals one characteristic property of soft matter, namely that it concerns materials that are not in a gaseous state.[1]

Another field of study can generally be excluded from the *soft matter* realm, which is solid state physics,[2] i.e. the physics of solid crystals with short- and long-range positional, and, if applicable, orientational order, in all spatial dimensions.[3,4] Likewise, *simple liquids* are often excluded as well,[5] although the definition of "simple" in this context is not generally agreed upon either.[6]

What remains, then, are systems that are characterized by some or all of the following features:

[1] R. A. L. Jones. *Soft Condensed Matter*. 1st ed. Oxford University Press, 2002, Section 1.1.
[2] Jones, *Soft Condensed Matter*, Section 1.1.
[3] Jones, *Soft Condensed Matter*, Section 1.2.
[4] I. W. Hamley. *Introduction to Soft Matter – Revised Edition. Synthetic and Biological Self-Assembling Materials*. John Wiley & Sons, 2007, Section 1.3.
[5] Jones, *Soft Condensed Matter*, Section 1.1.
[6] J.-P. Hansen and I. R. McDonald. *Theory of Simple Liquids*. 2nd ed. Academic Press, 1990, Section 1.2.

- Large (and often slow[7]) responses to small external perturbations,[8,9,10] which includes the fact that soft matter systems may be orders of magnitude easier to deform (and hence are, in this sense, *softer*) than typical solids.[11,12,13,14]

- Characteristic length scales (e.g. sizes of constituent particles) which are considerably larger than atomic ones,[15] but smaller than macroscopic ones; i.e. length scales roughly between a nanometer and a micrometer.[16,17,18,19]

- Consequently, behavior that is largely dictated not by chemical details, but rather by physical properties, e.g. topology and steric constraints.[20] As such, soft matter made of seemingly unrelated chemical compounds can exhibit similar physical behavior, a phenomenon often called *universality*.[21,22,23] This often allows one to disregard chemical details in models and computer simulations, which can greatly reduce the model complexity and computational effort required. Conversely, theories making use of universality commonly do not aim to predict particular quantities (e.g. size or stiffness) to a high degree of quantitative accuracy, but rather explain how they scale e.g. with the degree of polymerization.[24,25]

[7] P. Ziherl. *Soft Matter Physics*. 2014. URL: `http://www-f1.ijs.si/~ziherl/smt.pdf` (visited on 2019-01-28), Chapter 1.
[8] Jones, *Soft Condensed Matter*, Section 1.1.
[9] G. Gompper and M. Schick, eds. *Polymer Melts and Mixtures*. Vol. 1. Soft Matter. Wiley-VCH, 2006, Preface by B. Widom.
[10] M. Daoud and C. E. Williams, eds. *Soft Matter Physics*. Springer, 1999, Foreword by P. G. de Gennes.
[11] J. K. G. Dhont, G. Gompper, G. Nägele, D. Richter, and R. G. Winkler, eds. *Soft Matter. From Synthetic to Biological Materials*. Vol. 1. Schriften des Forschungszentrums Jülich, Reihe Schlüsseltechnologien / Key Technologies. Forschungszentrum Jülich, 2008, Section I.1.2.
[12] J. K. G. Dhont, G. Gompper, and D. Richter, eds. *Soft Matter: Complex Materials on Mesoscopic Scales*. Vol. 10. Matter and Materials. Forschungszentrum Jülich, 2002, Preface.
[13] Gompper and Schick, *Polymer Melts and Mixtures*, Preface by B. Widom.
[14] Ziherl, *Soft Matter Physics*, Chapter 1.
[15] Dhont, Gompper, Nägele, Richter, and Winkler, *Soft Matter*, Section I.1.1.
[16] Jones, *Soft Condensed Matter*, Section 1.1.
[17] Dhont, Gompper, and Richter, *Soft Matter: Complex Materials on Mesoscopic Scales*, Preface.
[18] C. N. Likos. "Effective interactions in soft condensed matter physics". *Physics Reports* **348** (2001), 267. Section 2.1.
[19] Hamley, *Introduction to Soft Matter – Revised Edition*, Section 1.3.
[20] Gompper and Schick, *Polymer Melts and Mixtures*, Preface by B. Widom.
[21] Jones, *Soft Condensed Matter*, Section 1.1.
[22] Ziherl, *Soft Matter Physics*, Chapter 1.
[23] Gompper and Schick, *Polymer Melts and Mixtures*, Chapter "An Introduction to Soft Matter".
[24] Ziherl, *Soft Matter Physics*, Chapter 1.
[25] Gompper and Schick, *Polymer Melts and Mixtures*, Chapter "An Introduction to Soft Matter".

- Characteristic energy scales, like the ones corresponding to bonding or deformation energies, that are comparable to the thermal energy $k_{\mathrm{B}}T$.[26,27,28,29] This in turn lends Brownian motion[30] and thermal fluctuations,[31] as well as entropic effects,[32] considerable importance.[33]

- The propensity towards self-assembly and self-organization at various, hierarchical scales: Molecules form, or take on particular conformations, in correspondence with the underlying balance of energetic and entropic contributions, and/or they aggregate into larger-scale structures, like micelles, membranes, and other mesophases.[34,35,36,37] Polydispersity, i.e. the circumstance that soft matter molecules' sizes often follow a probability distribution rather than having a fixed value, enhances the richness and complexity of structures that can be formed.[38]

- Viscosities much higher than those found in simple liquids, which may be dependent on the stresses exerted, such that the behavior is non-Newtonian (or viscoelastic).[39]

[26] Jones, *Soft Condensed Matter*, Section 1.1.
[27] Dhont, Gompper, and Richter, *Soft Matter: Complex Materials on Mesoscopic Scales*, Preface.
[28] Gompper and Schick, *Polymer Melts and Mixtures*, Preface by B. Widom.
[29] Hamley, *Introduction to Soft Matter – Revised Edition*, Section 1.2.
[30] Jones, *Soft Condensed Matter*, Section 1.1.
[31] Daoud and Williams, *Soft Matter Physics*, Preface.
[32] Gompper and Schick, *Polymer Melts and Mixtures*, Preface by B. Widom.
[33] Ziherl, *Soft Matter Physics*, Chapter 1.
[34] Jones, *Soft Condensed Matter*, Section 1.1.
[35] Dhont, Gompper, Nägele, Richter, and Winkler, *Soft Matter*, Section I.1.1.
[36] Dhont, Gompper, and Richter, *Soft Matter: Complex Materials on Mesoscopic Scales*, Preface.
[37] Ziherl, *Soft Matter Physics*, Chapter 1.
[38] Ziherl, *Soft Matter Physics*, Chapter 1.
[39] Ziherl, *Soft Matter Physics*, Chapter 1.

Examples of soft matter systems include gels,[40] polymers[41,42] in solutions[43,44] and melts,[45] colloids[46,47,48] (of sizes in the range of $1\,\mathrm{nm} - 1000\,\mathrm{nm}$)[49,50] and colloidal dispersions,[51] liquid crystals,[52,53,54,55] viscoelastic liquids[56,57] and foams,[58,59] industrial products such as glues,[60,61] inks,[62,63] paints,[64] soaps,[65,66] and detergents,[67] many foods,[68] such as milk[69] and honey,[70] and biological macromolecules,[71] membranes,[72] and entire cells.[73,74] In many—but not all—of these examples, mesoscopic components are embedded in a solvent (which is why those systems are commonly called *complex fluids*), so that it stands to reason that hydrodynamics often plays an important role.[75]

[40]Gompper and Schick, *Polymer Melts and Mixtures*, Preface by B. Widom.
[41]Dhont, Gompper, and Richter, *Soft Matter: Complex Materials on Mesoscopic Scales*, Preface.
[42]Gompper and Schick, *Polymer Melts and Mixtures*, Preface by B. Widom.
[43]Jones, *Soft Condensed Matter*, Section 1.2.
[44]Ziherl, *Soft Matter Physics*, Chapter 1.
[45]Jones, *Soft Condensed Matter*, Sections 1.1 and 1.2.
[46]Dhont, Gompper, and Richter, *Soft Matter: Complex Materials on Mesoscopic Scales*, Preface.
[47]Gompper and Schick, *Polymer Melts and Mixtures*, Preface by B. Widom.
[48]Ziherl, *Soft Matter Physics*, Chapter 1.
[49]Dhont, Gompper, Nägele, Richter, and Winkler, *Soft Matter*, Section I.1.1.
[50]Ziherl, *Soft Matter Physics*, Chapter 1.
[51]Jones, *Soft Condensed Matter*, Section 1.1.
[52]Jones, *Soft Condensed Matter*, Section 1.1.
[53]Dhont, Gompper, and Richter, *Soft Matter: Complex Materials on Mesoscopic Scales*, Preface.
[54]Gompper and Schick, *Polymer Melts and Mixtures*, Preface by B. Widom.
[55]Ziherl, *Soft Matter Physics*, Chapter 1.
[56]Jones, *Soft Condensed Matter*, Section 1.2.
[57]Ziherl, *Soft Matter Physics*, Chapter 1.
[58]Jones, *Soft Condensed Matter*, Section 1.2.
[59]Ziherl, *Soft Matter Physics*, Chapter 1.
[60]Jones, *Soft Condensed Matter*, Section 1.1.
[61]Dhont, Gompper, and Richter, *Soft Matter: Complex Materials on Mesoscopic Scales*, Preface.
[62]Dhont, Gompper, and Richter, *Soft Matter: Complex Materials on Mesoscopic Scales*, Preface.
[63]Likos, "Effective interactions in soft condensed matter physics", Section 2.1.
[64]Jones, *Soft Condensed Matter*, Section 1.1.
[65]Jones, *Soft Condensed Matter*, Section 1.1.
[66]Likos, "Effective interactions in soft condensed matter physics", Section 2.1.
[67]Dhont, Gompper, and Richter, *Soft Matter: Complex Materials on Mesoscopic Scales*, Preface.
[68]Jones, *Soft Condensed Matter*, Section 1.1.
[69]Dhont, Gompper, and Richter, *Soft Matter: Complex Materials on Mesoscopic Scales*, Preface.
[70]Ziherl, *Soft Matter Physics*, Chapter 1.
[71]Dhont, Gompper, and Richter, *Soft Matter: Complex Materials on Mesoscopic Scales*, Preface.
[72]Dhont, Gompper, and Richter, *Soft Matter: Complex Materials on Mesoscopic Scales*, Preface.
[73]Dhont, Gompper, Nägele, Richter, and Winkler, *Soft Matter*, Section I.1.1.
[74]Dhont, Gompper, and Richter, *Soft Matter: Complex Materials on Mesoscopic Scales*, Preface.
[75]Dhont, Gompper, Nägele, Richter, and Winkler, *Soft Matter*, Section I.1.1.

1.2 Contents and Organization

This thesis is organized as follows:

Chapter 2 introduces linear polymers and discusses how they are modeled in this thesis.

In subsequent chapters, the two soft matter systems considered in this thesis will be discussed:

First, in Chapter 3, magnetically functionalized star polymers (MFSPs) with magnetic moments in dilute (Newtonian) solution will be investigated.

Chapter 4 introduces the reader to the basics of fluid dynamics, to the extent needed for the discussion of the second system, a melt of linear polymers, presented in Chapter 5.

Both soft matter systems are treated with the same simulation technique, Multi-Particle Collision Dynamics (MPCD) with embedded Molecular Dynamics (MD). Chapter 6 describes the techniques in general, as well as details of the algorithms employed in this thesis, while Chapter 7 presents the particular simulation and analysis package, *OpenMPCD*,[76] that has been developed by the author for the research at hand.

Near the end of the thesis, appendices (e.g. on conventions regarding mathematical definitions and notations) offer information that the reader may find useful, but which might not be essential to the understanding of the main body of the text.

The thesis ends with a list of mathematical symbols used, including short descriptions thereof, and a bibliography.

1.3 Citing Conventions

It goes without saying that information taken from literature or other communications is cited in this work to the author's best knowledge and ability. As a general rule, such citations appear in close proximity to the place where the referenced information first appears in this text, i.e. following a term or phrase at the point of introduction, or preceding a formula taken from the literature. However, to avoid repeated citing of the same source within a sentence or paragraph, a citation may appear at the end of such sentence or paragraph, then applying to its entirety.

In those parts of this thesis that are intended to give the interested reader a short introduction to a well-known subject (e.g. hydrodynamics), the exposition often follows in the tracks of one or more textbooks. In these and similar cases, a corresponding citation footnote appears in the heading of the section concerned.

[76] D. Toneian. *OpenMPCD*. URL: `https://openmpcd.org`.

Verbatim quotes appear in quotation marks, “like this”, when they are relatively short, or, if they are longer, are indicated by a vertical line to the left of the quoted content,

> like this.

For technical reasons, footnotes are moved to the page(s) following the end of the citation in the latter case.

Resources cited for the first time in a particular chapter appear in a verbose format in footnotes, while following references to the same resources appear in a shorter format. Full bibliographical information for all sources can be found in the bibliography at the end of the thesis.

Parts of this thesis are related to the author's previous thesis (*Diplomarbeit*).[77] Instead of merely referring the reader to the latter for an introduction to those parts, portions of the *Diplomarbeit* are reproduced, in slightly adapted form, in an attempt to make the thesis more self-contained.

1.4 Acknowledgements

This thesis and the work described therein would not have been possible, were it not for the extremely proficient and friendly support by Prof. Gerhard Kahl (TU Wien), Prof. Christos N. Likos (University of Vienna), Prof. Roland G. Winkler, and Prof. Gerhard Gompper (both Forschungszentrum Jülich), for which I am most grateful.

Further, I thank the TU Wien, the University of Vienna, the FWF and its SFB ViCoM (F41), the Forschungszentrum Jülich, the University of Oxford, the Jülich Supercomputing Centre, the Vienna Scientific Cluster and the IHRS BioSoft Guest Student Program for financial support and/or infrastructure provided.

[77] D. Toneian. “Multi-Particle Collision Dynamics Simulation of Viscoelastic Fluids”. Diploma thesis. TU Wien, 2015.

Last but not least, I would like to thank very much (in alphabetical order) Thorsten Auth, Ronald Blaak, Iurii Chubak, Thomas Eisenstecken, Maud Formanek, Raphael Hornung, Martin Jehser, Angela Koffler, Dimitrios Kyranas, Maximilian Liebetreu, Marisol Ripoll, Sebastian Rode, Mario Theers, Anoop Varghese, Lisa Weiß, Elmar Westphal, Jens Winkelmann, Julia Yeomans, and Andreas Zöttl for helpful discussions, and furthermore Angela Koffler for help in creating Fig. 3.9.

Chapter 2

Polymers and their Models

This chapter starts by giving a brief description of the atomistic composition of chemical polymers, and some concomitant properties. Then, it motivates and describes some physical models of polymers, which abstract away a lot of the chemical details, while retaining the most important physical features.

On the one hand, these simplified models allow for easier and more general theoretical treatment of the polymers. On the other, in computer simulations they oftentimes adequately capture the relevant physics in a qualitative manner, while reducing computational cost dramatically, compared to the alternative of atom-by-atom computer simulations. Thus, the simplified models allow one to simulate systems that would otherwise be inaccessible due to their size and/or complexity.

2.1 Polymers in Chemistry

The word *polymer* derives from the Greek *polys* (*many*) and *meros* (*part*).[1,2,3,4] It describes large molecules (*macromolecules*) that are made of a large number of chemical units, called monomers, which are repeated multiple times in the polymer molecule, but in such a way that the number of chemically *distinct* units (monomers) is rather small.[5,6]

The simplest form, thus, is a polymer that is both

- *regular*,[7] i.e. there is only one type of monomer (also called *constitutional repeating unit*[8]), and
- *linear*, such that there are no branch points.[9]

If one denotes the monomer with A, then such a simple polymer can be represented by a linear chain like this:

A—A—A—. . .—A—A—A

The number of A units appearing is called the *degree of polymerization*, which typically ranges between 100 and 10^9.[10]

[1] P. C. Painter and M. M. Coleman. *Essentials of Polymer Science and Engineering*. DEStech Publications, 2009, Section 1.
[2] A. Isihara. *Condensed Matter Physics*. Dover Publications, 2007, Section 12.2.
[3] M. Rubinstein and R. H. Colby. *Polymer Physics*. 3rd ed. Oxford University Press, 2003, Section 1.2.
[4] Online Etymology Dictionary. *Polymer*. URL: `https://www.etymonline.com/word/polymer` (visited on 2019-01-16).
[5] Doi. *Introduction to Polymer Physics*. Oxford University Press, 1996, Section 1.
[6] *Compendium of Chemical Terminology*. Version 2.3.3. International Union of Pure and Applied Chemistry. 2014. URL: `https://goldbook.iupac.org/`, Definitions of "polymer" and "macromolecule (polymer molecule)".
[7] International Union of Pure and Applied Chemistry. *Compendium of Polymer Terminology and Nomenclature. IUPAC Recommendations 2008*. RSC Publishing, 2009, Section 1.1.4.
[8] International Union of Pure and Applied Chemistry, *Compendium of Polymer Terminology and Nomenclature*, Section 1.1.15.
[9] International Union of Pure and Applied Chemistry, *Compendium of Polymer Terminology and Nomenclature*, Section 1.1.32.
[10] Doi, *Introduction to Polymer Physics*, Section 1.

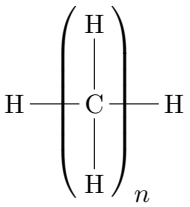

(a) Poly(methylene)

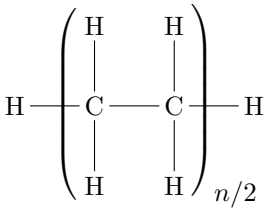

(b) Poly(ethylene)

Figure 2.1: Two equivalent representations of a polyethylene macromolecule with n C-atoms and $2n$ H-atoms (plus two more for the end monomers), with equivalent degrees of polymerization n and $n/2$, respectively; in (a), the monomer unit is CH_2, while in (b), it is C_2H_4. The latter representation is more traditional, as is the source-based name *polyethylene*, compared to the structure-based name *poly(methylene)*.[14]

To offer a specific example that is both instructive and simple in its chemical makeup, *poly(methylene)* has CH_2 as its monomer unit; the macromolecule is better known by the name *polyethylene*, where the monomer unit is defined to be C_2H_4.[11,12,13] Both conventions refer to the same chemical substance; see Fig. 2.1, where graphical representations of this polymer are shown.

[11] International Union of Pure and Applied Chemistry, *Compendium of Polymer Terminology and Nomenclature*, Section 14.2.2.1, Table 4.
[12] Doi, *Introduction to Polymer Physics*, Section 1.1.1.
[13] L. H. Sperling. *Introduction to Polymer Science*. 4th ed. John Wiley & Sons, 2006, Section 1.1.
[14] International Union of Pure and Applied Chemistry. *Compendium of Polymer Terminology and Nomenclature. IUPAC Recommendations 2008*. RSC Publishing, 2009, Section 14.2.2.1, Table 4.

While it is true that the polyethylene macromolecule is linear in the (topological) sense described above, i.e. it contains no points where three carbon atoms branch off a shared carbon atom, two consecutive bonds do not enclose an angle of 180°, i.e. the carbon atoms do not lie on a straight line. Indeed, the angle formed by three consecutive carbon atoms is found to be $\sim 110°$ and the angle between two hydrogen atoms and their shared carbon atom is about 108°,[15] so that sections of the polymer are more realistically represented the way shown in Fig. 2.2. This, along with the observation that the carbon-carbon bonds can be rotated, allows the macromolecule's carbon backbone to describe paths in space that are not straight; Thus, there is a certain flexibility in the macromolecule. One way to characterize this polymer flexibility is via the *persistence length*:[16] Letting s denote the position along the polymer backbone's contour, one can ask how strong the correlation between the backbone tangent vector (i.e. the direction of the next bond along the polymer backbone) at two arbitrary points, s_0 and $s_0+\Delta s$, is. If Δs is small, i.e. if one considers two points on the polymer backbone that are in close succession, then one may expect the two tangent vectors to point along similar directions. If, on the other hand, Δs is large, the tangent vectors at s_0 and $s_0 + \Delta s$ will be only weakly correlated. The persistence length is then loosely defined as the contour length Δs after which one can consider the directions of the contour tangent vectors at s_0 and $s_0 + \Delta s$ independent of one another.

The magnitude of the persistence length is, of course, dependent on the type of polymer considered (for polyethylene, it is 5.75 Å,[17] and thus only a few multiples of the carbon-carbon bond length of about 1.55 Å[18]). The main significance of this observation lies the fact that there *is* such a (finite) length where, if two bonds are separated at least by this distance from one another, the details of the bond conformations become irrelevant, and beyond which one can consider the orientation of the two bonds as essentially random.

[15] M. S. Miao, P. E. Van Camp, V. E. Van Doren, J. J. Ladik, and J. W. Mintmire. "Conformation and electronic structure of polyethylene: A density-functional approach". *Physical Review B* **54** (1996), 10430.
[16] Sperling, *Introduction to Polymer Science*, Section 5.2.1.
[17] Sperling, *Introduction to Polymer Science*, Section 5.2.1.
[18] Miao, Van Camp, Van Doren, Ladik, and Mintmire, "Conformation and electronic structure of polyethylene: A density-functional approach".

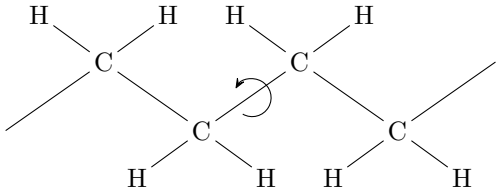

Figure 2.2: Two-dimensional representation of a part of polyethylene that takes the true bond-angles into account. The arrow indicates that there is a rotational degree of freedom about the carbon-carbon bonds, which allows for changes in the direction of the macromolecule's carbon backbone.

Despite the simplicity of this polymer description and the other ones discussed in the following, they can capture the qualitative behavior of large classes of polymers, with chemical details manifesting themselves only through the values of the parameters such as the persistence length. In this context, one often speaks of *universality* in the behavior of polymers (cf. Section 1.1).[19,20]

2.2 The Freely Rotating Chain Model[21,22]

One can take the existence of a finite persistence length as a basis for a simple model of a polymer, which is commonly called the model of the *freely rotating chain* (FRC).[23] This model aids in understanding the overall configurational behavior (i.e. what shape the polymer assumes), and reduces the polymer to its backbone – in the case of polyethylene, the chain of carbon atoms, entirely neglecting the hydrogen atoms.

What remains, then, is a fixed number of carbon atoms. Since typically, bond lengths (i.e. distances between successive monomers) and angles vary by only about 3% about their mean values in real polymers,[24] this model assumes that the carbon atoms are separated from their nearest neighbors by a fixed distance b_{FRC}, with a fixed angle α_{FRC} formed by the bonds between three consecutive carbon atoms.

[19] I. Teraoka. *Polymer Solutions. An Introduction to Physical Properties.* John Wiley & Sons, 2002, Section 1.1.1.
[20] M. Kröger. "Simple models for complex nonequilibrium fluids". *Physics Reports* **390** (2004), 453. Section 1.
[21] Teraoka, *Polymer Solutions*, Sections 1.1.2.1 and 1.2.3.2.
[22] M. Doi and S. F. Edwards. *The Theory of Polymer Dynamics.* Oxford University Press, 1994, Section 2.1.2.
[23] Teraoka, *Polymer Solutions*, Sections 1.1.2.1 and 1.2.3.2.
[24] R. B. Bird, C. F. Curtiss, R. C. Armstrong, and O. Hassager. *Kinetic Theory.* 2nd ed. Vol. 2. Dynamics of Polymeric Liquids. John Wiley & Sons, 1987, Section 11.2.

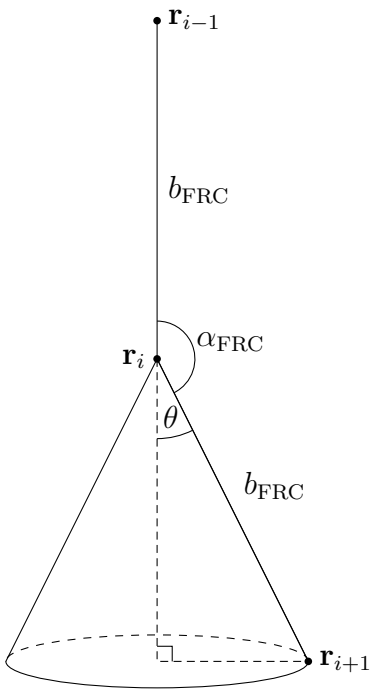

Figure 2.3: Graphical representation of a section of a polymer in the freely rotating chain (FRC) model. Given the positions $\mathbf{r}_i$ and $\mathbf{r}_{i-1}$ of the i-th monomer and its predecessor $i-1$, respectively, the successor monomer $i+1$ lies on a right (i.e. not oblique, or slanted) circular cone's directrix, with the cone's apex at $\mathbf{r}_i$, and a cone opening angle $\theta = 180° - \alpha_{\mathrm{FRC}}$. Each monomer is separated by a distance b_{FRC} from its nearest neighbors.

Let $\mathbf{r}_i$ be the position vector of carbon atom i in an arbitrary coordinate system, and let $\mathbf{r}_{i-1}$ and $\mathbf{r}_{i+1}$ be the positions of the previous and next carbon atoms along the polymer backbone, respectively. Given values for $\mathbf{r}_{i-1}$ and $\mathbf{r}_i$, the next carbon atom must then lie on the *directrix* (i.e. the rim) of a right (i.e. not oblique, or slanted) circular cone, with the cone's apex at $\mathbf{r}_i$ and a cone opening angle of $\theta = (180° - \alpha_{\mathrm{FRC}})$. For symmetry reasons, any point on the cone's directrix is assumed by $\mathbf{r}_{i+1}$ with equal probability. The situation is visualized in Fig. 2.3.

To analyze the relationship between the direction of one bond and the direction of subsequent bonds, one may first define $\Delta\mathbf{r}_i := \mathbf{r}_i - \mathbf{r}_{i-1}$, the bond vector from monomer (or atom) $i-1$ to i. One clearly has $\Delta\mathbf{r}_i \cdot \Delta\mathbf{r}_{i+1} = b_{\mathrm{FRC}}^2 \cos(\theta)$.

In order to obtain $\langle \Delta\mathbf{r}_{i+1} \rangle_{\Delta\mathbf{r}_i}$, the expectation value of $\Delta\mathbf{r}_{i+1}$ for a given $\Delta\mathbf{r}_i$, one can decompose $\Delta\mathbf{r}_{i+1}$ into a component parallel to $\Delta\mathbf{r}_i$ (the vertical dashed line in Fig. 2.3), which amounts to $\cos(\theta) \cdot \Delta\mathbf{r}_i$, independent of the particular position of $\mathbf{r}_{i+1}$ on the cone's directrix, and a component perpendicular to $\Delta\mathbf{r}_i$ (the horizontal dashed line in Fig. 2.3), which averages

to 0 as every position on the directrix is equally probable. Therefore,

$$\langle \Delta\mathbf{r}_{i+1} \rangle_{\Delta\mathbf{r}_i} = \cos(\theta) \cdot \Delta\mathbf{r}_i. \tag{2.1}$$

One should emphasize that $\langle \Delta\mathbf{r}_{i+1} \rangle_{\Delta\mathbf{r}_i}$ is independent of all $\Delta\mathbf{r}_{i-n}$ with $n > 0$.

The relation between $\Delta\mathbf{r}_{i-1}$ and $\Delta\mathbf{r}_{i+1}$ may then be explored by multiplying both sides of Eq. (2.1) by $\Delta\mathbf{r}_{i-1}$,

$$\Delta\mathbf{r}_{i-1} \cdot \langle \Delta\mathbf{r}_{i+1} \rangle_{\Delta\mathbf{r}_i} = \cos(\theta) \cdot (\Delta\mathbf{r}_{i-1} \cdot \Delta\mathbf{r}_i), \tag{2.2}$$

and taking the expectation value w.r.t. $\Delta\mathbf{r}_i$ for a fixed $\Delta\mathbf{r}_{i-1}$:

$$\begin{aligned}
\left\langle \Delta\mathbf{r}_{i-1} \cdot \langle \Delta\mathbf{r}_{i+1} \rangle_{\Delta\mathbf{r}_i} \right\rangle_{\Delta\mathbf{r}_{i-1}} &= \langle \cos(\theta) \cdot (\Delta\mathbf{r}_{i-1} \cdot \Delta\mathbf{r}_i) \rangle_{\Delta\mathbf{r}_{i-1}} && \text{(2.3a)} \\
&= \cos(\theta) \cdot \langle \Delta\mathbf{r}_{i-1} \cdot \Delta\mathbf{r}_i \rangle_{\Delta\mathbf{r}_{i-1}} && \text{(2.3b)} \\
&= \cos(\theta) \cdot \left(\Delta\mathbf{r}_{i-1} \cdot \langle \Delta\mathbf{r}_i \rangle_{\Delta\mathbf{r}_{i-1}} \right) && \text{(2.3c)} \\
&= \cos(\theta) \cdot (\Delta\mathbf{r}_{i-1} \cdot \cos(\theta) \cdot \Delta\mathbf{r}_{i-1}) && \text{(2.3d)} \\
&= (\cos(\theta))^2 \cdot (\Delta\mathbf{r}_{i-1} \cdot \Delta\mathbf{r}_{i-1}) && \text{(2.3e)} \\
&= (\cos(\theta))^2 \cdot b_{\mathrm{FRC}}^2, && \text{(2.3f)}
\end{aligned}$$

where use has been made of Eq. (2.1) and the fact that $|\Delta\mathbf{r}_{i-1}| = b_{\mathrm{FRC}}$ by definition of the model.

This process can be generalized[25] to yield the recursion equation (without loss of generality letting $m < n$)

$$\langle \Delta\mathbf{r}_m \cdot \Delta\mathbf{r}_n \rangle_{\Delta\mathbf{r}_m} = \cos(\theta) \langle \Delta\mathbf{r}_{m+1} \cdot \Delta\mathbf{r}_n \rangle_{\Delta\mathbf{r}_{m+1}} \tag{2.4}$$

with the initial condition

$$\langle \Delta\mathbf{r}_n \cdot \Delta\mathbf{r}_n \rangle_{\Delta\mathbf{r}_n} = |\Delta\mathbf{r}_n|^2 = b_{\mathrm{FRC}}^2, \tag{2.5}$$

the solution of which is[26]

$$\langle \Delta\mathbf{r}_m \cdot \Delta\mathbf{r}_n \rangle_{\Delta\mathbf{r}_m} = (\cos(\theta))^{|n-m|} b_{\mathrm{FRC}}^2. \tag{2.6}$$

[25] Doi and Edwards, *The Theory of Polymer Dynamics*, Section 2.1.2.
[26] Doi and Edwards, *The Theory of Polymer Dynamics*, Section 2.1.2.

This result is intuitive:[27] Clearly, $\langle \Delta\mathbf{r}_i \cdot \Delta\mathbf{r}_i \rangle = b_{\mathrm{FRC}}^2$, and by the argument presented in the discussion of the relationship of $\Delta\mathbf{r}_i$ and $\Delta\mathbf{r}_{i+1}$, $\langle \Delta\mathbf{r}_i \cdot \Delta\mathbf{r}_{i+1} \rangle = \cos(\theta)\, b_{\mathrm{FRC}}^2$. Thus, the freedom of a bond to rotate reduces the correlation by a factor of $\cos(\theta)$. Successive application of the same argument then results in repeated multiplications by $\cos(\theta)$, yielding the desired result.

The key significance of Eq. (2.6) is that the correlation in the direction of the (fixed-length) bond vectors decays exponentially with the distance along the backbone (unless of course $\cos(\theta) \in \{-1, 0, 1\}$, or equivalently, α_{FRC} is an integer multiple of 90°). This is what justifies the use of an even simpler model, to be discussed in the next section on the freely jointed chain model.

Another useful computation determines the expectation value (w.r.t. the random placement of successive monomers on their respective cone directrices) of the squared end-to-end distance, $\langle R^2 \rangle = \langle \mathbf{R} \cdot \mathbf{R} \rangle$, where $\mathbf{R} := \mathbf{r}_N - \mathbf{r}_0$ is the vector pointing from the first monomer's position $\mathbf{r}_0$ to the position of the last monomer, $\mathbf{r}_N$:

Since

$$\begin{aligned} \mathbf{R} &= \mathbf{r}_N - \mathbf{r}_0 && \text{(2.7a)} \\ &= \mathbf{r}_N - \mathbf{r}_{N-1} + \mathbf{r}_{N-1} - \mathbf{r}_{N-2} + \ldots + \mathbf{r}_1 - \mathbf{r}_0 && \text{(2.7b)} \\ &= \sum_{i=1}^{N} \Delta\mathbf{r}_i, && \text{(2.7c)} \end{aligned}$$

[27] Rubinstein and Colby, *Polymer Physics*, Section 2.3.1.

one has, with Eq. (2.6) (and requiring $|\cos(\theta)| \neq 1$)[28,29,30]

$$\left\langle R^2 \right\rangle = \left\langle \left(\sum_{i=1}^{N} \Delta \mathbf{r}_i \right) \cdot \left(\sum_{j=1}^{N} \Delta \mathbf{r}_j \right) \right\rangle \tag{2.8a}$$

$$= \sum_{i=1}^{N} \sum_{j=1}^{N} \langle \Delta \mathbf{r}_i \cdot \Delta \mathbf{r}_j \rangle \tag{2.8b}$$

$$= \sum_{i=1}^{N} \sum_{j=1}^{N} (\cos(\theta))^{|i-j|} b_{\mathrm{FRC}}^2 \tag{2.8c}$$

$$= b_{\mathrm{FRC}}^2 N \frac{1+\cos(\theta)}{1-\cos(\theta)} - 2 b_{\mathrm{FRC}}^2 \cos(\theta) \frac{1-(\cos(\theta))^N}{(1-\cos(\theta))^2}, \tag{2.8d}$$

so that in the limit of a large number N of bonds,

$$\lim_{N\to\infty} \left(\left\langle R^2 \right\rangle / N \right) = b_{\mathrm{FRC}}^2 \frac{1+\cos(\theta)}{1-\cos(\theta)}, \tag{2.9}$$

i.e. $\langle R^2 \rangle$ scales with N, rather than with N^2 as one might perhaps assume at first glance.

2.3 The Freely Jointed Chain Model

Instead of considering individual backbone atoms in a polymer, one can take a coarse-grained view and group several, say, carbon atoms (along with e.g. hydrogen atoms attached to them) into one *effective* monomer. The more backbone atoms such a monomer encompasses, the better the approximation $\langle \Delta \mathbf{r}_n \cdot \Delta \mathbf{r}_{n+1} \rangle \approx 0$ holds, with $\Delta \mathbf{r}_i = \mathbf{r}_i - \mathbf{r}_{i-1}$, now being the bond vector from the *effective* monomer $i-1$ to its successor i (cf. Eq. (2.6)).

So, in the *freely jointed chain* (FJC) model, or *random-flight* model,[31] one assumes that $\langle \Delta \mathbf{r}_n \cdot \Delta \mathbf{r}_{n+1} \rangle = 0$ exactly, in addition to the assumption of a fixed bond length b_{FJC}, now understood to mean the spatial separation between consecutive *effective* monomers.

Since each bond's direction is now independent of all other bond orientations – which implies that the polymer can fold back onto itself, i.e. that there is no excluded volume –, the model corresponds to a random walk in three dimensions with fixed step size b_{FJC}. Given the position

[28] Teraoka, *Polymer Solutions*, Equation 1.32.
[29] H. Yamakawa and Y. Takenao. *Helical Wormlike Chains in Polymer Solutions*. 2nd ed. Springer, 2016. Equation 2.10.
[30] J. Bois. *Rudiments of Polymer Physics*. 2002. URL: `http://pimprenelle.lps.ens.fr/biolps/sites/default/files/teaching/4/poly_elast.pdf` (visited on 2019-01-28), Section 2.3.
[31] Yamakawa and Takenao, *Helical Wormlike Chains in Polymer Solutions*, Section 2.1.2.

$\mathbf{r}_0$ of the first monomer, the position $\mathbf{r}_N$ of the last monomer follows the Gaussian distribution[32]

$$\mathrm{P}\left(\mathbf{r}_N;\mathbf{r}_0\right) = \left(2\pi N b_{\mathrm{FJC}}^2/3\right)^{-3/2} \exp\left(-\frac{3\left(\mathbf{r}_N-\mathbf{r}_0\right)^2}{2Nb_{\mathrm{FJC}}^2}\right). \tag{2.10}$$

This result even holds in a more general case, where the non-constant step length b is allowed to follow any one distribution, provided that the distribution function implies an expectation value of b_{FJC}^2 for the mean squared bond length.[33]

Eq. (2.10) implies that the FJC model can be understood as two point masses, at $\mathbf{r}_0$ and $\mathbf{r}_N$ respectively, joined by a harmonic (Hookean) spring, with potential

$$V_{\mathrm{FJC}} = K_{\mathrm{FJC}}\left(\mathbf{r}_N-\mathbf{r}_0\right)^2/2 \tag{2.11}$$

and spring constant $K_{\mathrm{FJC}} = 3/\left(Nb_{\mathrm{FJC}}^2\right)$ (in units of the thermal energy scale $k_{\mathrm{B}}T$ imposed by a thermodynamic surrounding).[34,35] This idea, along with straightforward generalization to more than two joined point masses, will be put to use in Chapter 5.

2.4 The Bead-Spring Model

This finding, in turn, motivates another level of coarse-graining, where a number of FJC monomers large enough to satisfy Eq. (2.10) are grouped together into *effective monomers of the bead-spring model*, with the effective monomers being joined to their nearest neighbors via springs. The advantage of this model lies in the absence of fixed constraints on the bond length, which may otherwise complicate theoretical treatment and Molecular Dynamics simulations.[36]

If the springs are, as in the previous section, taken to be harmonic, one obtains the *Rouse model*,[37] many properties of which can conveniently be treated analytically due to the Gaussian distribution underlying the model (cf. Section 5.1), but which suffers from the fact that, given sufficiently large forces, the polymer can be stretched to arbitrary lengths, a result that is clearly incompatible with real chemical systems.

[32] Teraoka, *Polymer Solutions*, Equation 1.20.
[33] Teraoka, *Polymer Solutions*, Section 1.2.2.3.
[34] Bird, Curtiss, Armstrong, and Hassager, *Kinetic Theory*, Example 11.3-3.
[35] H. Yamakawa. *Modern Theory of Polymer Solutions*. Electronic Edition. 2001. URL: `http://www.molsci.polym.kyoto-u.ac.jp/archives/redbook.pdf` (visited on 2019-01-18), Section 33.
[36] Bird, Curtiss, Armstrong, and Hassager, *Kinetic Theory*, 11.4.
[37] P. E. Rouse. "A Theory of the Linear Viscoelastic Properties of Dilute Solutions of Coiling Polymers". *The Journal of Chemical Physics* **21** (1953), 1272.

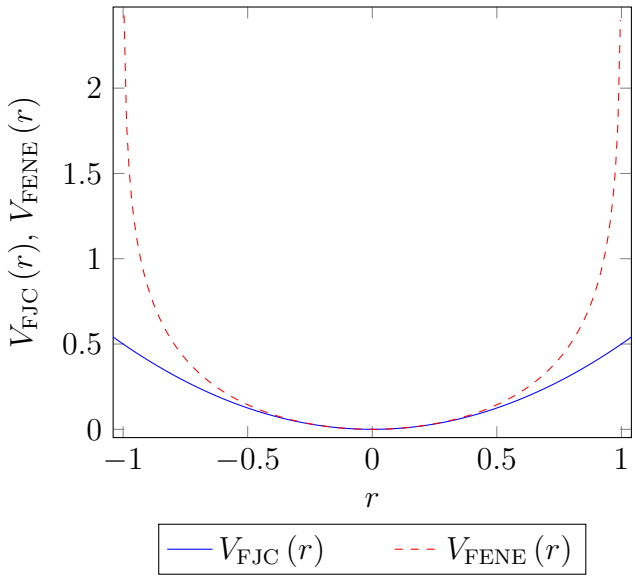

Figure 2.4: Comparison of the Hookean potential (cf. Eq. (2.11)) and the FENE potential Eq. (2.12) as a function of the instantaneous bond length r. Both spring constants and the parameter R_{FENE} have been set to 1 in this illustration.

One alternative for the bond potential is the *finitely extendible nonlinear elastic* (FENE) potential[38,39]

$$V_{\mathrm{FENE}}(r) = -\frac{1}{2} R_{\mathrm{FENE}}^2 K_{\mathrm{FENE}} \ln\left(1 - \left(\frac{r}{R_{\mathrm{FENE}}}\right)^2\right), \tag{2.12}$$

which prevents the instantaneous bond length r from exceeding a maximal value R_{FENE}. The FENE potential reduces to the harmonic potential with spring constant K_{FENE} in the limit $R_{\mathrm{FENE}} \to \infty$.[40] Fig. 2.4 illustrates the two potentials.

[38] H. R. Warner Jr. "Kinetic Theory and Rheology of Dilute Suspensions of Finitely Extendible Dumbbells". *Industrial & Engineering Chemistry Fundamentals* **11** (1972), 379.
[39] Bird, Curtiss, Armstrong, and Hassager, *Kinetic Theory*, Equation (G) in Table 11.5-1.
[40] Warner, "Kinetic Theory and Rheology of Dilute Suspensions of Finitely Extendible Dumbbells", Section I.B.

2.5 The Kremer-Grest Model

The bead-spring model discussed in the previous section is, like all models discussed so far, an *ideal chain* model,[41] which means that monomers are free to overlap. Although this peculiarity seems to be unphysical, the ideal chain models are, depending on the chain lengths and timescales considered,[42] often adequate descriptions of real systems, especially in concentrated solutions, melts, glasses, and dilute solutions in so-called theta solvents.[43]

In other circumstances, though, one may want to hinder monomers from approaching one another arbitrarily closely. Models that achieve this are called *real chain* or *excluded-volume chain* models,[44] and one such model is called the *Kremer-Grest* model:[45]

In this model, any two monomers, not necessarily nearest neighbors along the polymer chain, interact via the Weeks-Chandler-Andersen (WCA) potential,[46]

$$V_{\mathrm{WCA}}(r) = 4\epsilon_{\mathrm{WCA}}\left(\left(\frac{\sigma_{\mathrm{WCA}}}{r}\right)^{12} - \left(\frac{\sigma_{\mathrm{WCA}}}{r}\right)^{6} + \frac{1}{4}\right)\Theta\left(2^{1/6}\sigma_{\mathrm{WCA}} - r\right), \tag{2.13}$$

which is a Lennard-Jones potential shifted (term 1/4) and truncated (by the Heaviside step function $\Theta(x)$, which takes on the values 0, 1/2, or 1, for $x < 0$, $x = 0$, and $x > 0$, respectively) such that it is purely repulsive. r denotes the momentary separation of the centers of the two particles involved. Fig. 2.5 illustrates the WCA and Lennard-Jones potentials.

For bonds along the polymer chain, the Kremer-Grest model additionally makes use of the FENE potential, Eq. (2.12).

A generalization of this model will be employed in the study of star polymers in the next chapter.

[41] Teraoka, *Polymer Solutions*, Section 1.1.3.
[42] Gompper and Schick, *Polymer Melts and Mixtures*, Chapter 1.
[43] Teraoka, *Polymer Solutions*, Section 1.1.3.
[44] Teraoka, *Polymer Solutions*, Section 1.1.3.
[45] K. Kremer and G. S. Grest. "Molecular dynamics (MD) simulations for polymers". *Journal of Physics: Condensed Matter* **2** (1990), SA295.
[46] J. D. Weeks, D. Chandler, and H. C. Andersen. "Role of Repulsive Forces in Determining the Equilibrium Structure of Simple Liquids". *The Journal of Chemical Physics* **54** (1971), 5237.

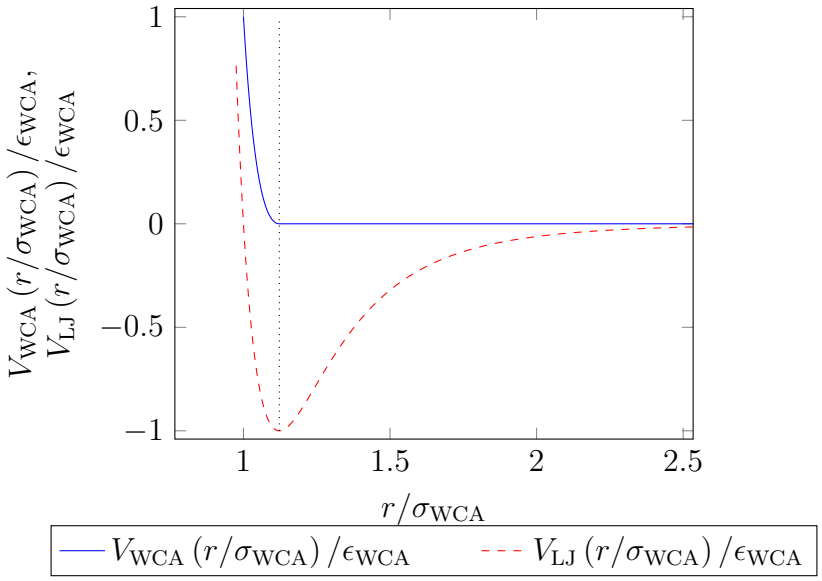

Figure 2.5: Comparison of the WCA potential (cf. Eq. (2.13)) and the Lennard-Jones potential $V_{\mathrm{LJ}}(r) = 4\epsilon_{\mathrm{WCA}}\left(\left(\frac{\sigma_{\mathrm{WCA}}}{r}\right)^{12} - \left(\frac{\sigma_{\mathrm{WCA}}}{r}\right)^{6}\right)$ as a function of the reduced instantaneous bond length r/σ_{WCA}. The dotted line marks the minimum of the potentials, at $r/\sigma_{\mathrm{WCA}} = 2^{1/6}$; the WCA potential is truncated to 0 for larger values of r.

Chapter 3

Magnetically Functionalized Star Polymers

Part of the work presented in this chapter has been published in the Journal of Physics: Condensed Matter by David Toneian, Christos N. Likos, and Gerhard Kahl, under the title "Controlled self-aggregation of polymer-based nanoparticles employing shear flow and magnetic fields", DOI 10.1088/1361-648X/ab0f6d – volume and page numbers have not yet been assigned.

The research presented is based, in particular, on Blaak and Likos[1], who study a similar model as investigated here, but only under equilibrium conditions.

Figure 3.1: Schematic illustration of a star polymer, consisting of a core particle and three attached linear polymer arms.

3.1 Star Polymers

In contrast to the linear polymers discussed in the previous chapter, this chapter deals with *star polymers*, a class of branched polymers that consists of a central core particle, attached to which there are a number of linear polymer chains, called *arms* in this context. Fig. 3.1 shows a sketch of such a star polymer with three arms. The core may consist of "an atom, a small molecule, or a macromolecular structure itself"[2]. The arms, in general, may differ from one another, and do not need to be regular polymers, but can instead possess features such as in-chain- or end-functionalization, asymmetries (with regard to topology, molecular weight, chemical composition, or functionalization), or multi-block (e.g. triblock copolymer) structures.[3]

One particular class of star polymers, called *telechelic star polymers* (abbreviated TSP), has identical polymeric arms that are diblock copolymers, i.e. arms of the structure

A—A—A—...—B—B—B

with the monomers A near to the central core being solvophilic, and the monomers B near the free ends of the arms being solvophobic; see Fig. 3.2 for a sketch.[4,5,6] Since the solvophobic monomers strive to minimize the contact area with the surrounding solvent fluid, the telechelic star polymer may form, depending on the system parameters (see below), clusters of solvophobic monomers, called *patches*. Emergence and stability of such patches, and what the probability distributions e.g. for the number and for the sizes of the patches are, depends on a number of parameters, such as the number of arms f per TSP, the fraction $\alpha = N_\mathrm{B}/(N_\mathrm{A} + N_\mathrm{B})$ of the number of solvophobic monomers over the total number of (non-core) monomers, and the quality and temperature of the solvent. Fig. 3.3, for example, shows the mean patch count as a function of f and α.

---

[1] R. Blaak and C. N. Likos. "Self-assembly of magnetically functionalized star-polymer nano-colloids". *The European Physical Journal E* **41** (2018), 3.

[2] N. Hadjichristidis, M. Pitsikalis, H. Iatrou, P. Driva, G. Sakellariou, and M. Chatzichristidi. "Polymers with Star-Related Structures: Synthesis, Properties, and Applications". Ed. by K. Matyjaszewski and M. Möller. Vol. 6. Polymer Science: A Comprehensive Reference. Elsevier, 2012. Chap. 6.03, 29. Section 6.03.1.1.

[3] Hadjichristidis, Pitsikalis, Iatrou, Driva, Sakellariou, and Chatzichristidi, "Polymers with Star-Related Structures: Synthesis, Properties, and Applications", Section 6.03.1.1.

[4] B. Capone, I. Coluzza, F. LoVerso, C. N. Likos, and R. Blaak. "Telechelic Star Polymers as Self-Assembling Units from the Molecular to the Macroscopic Scale". *Physical Review Letters* **109** (2012), 238301.

[5] B. Capone, I. Coluzza, R. Blaak, F. Lo Verso, and C. N. Likos. "Hierarchical self-assembly of telechelic star polymers: from soft patchy particles to gels and diamond crystals". *New Journal of Physics* **15** (2013), 095002. Section 1.

[6] F. Lo Verso and C. N. Likos. "End-functionalized polymers: Versatile building blocks for soft materials". *Polymer* **49** (2008), 1425. Section 4.

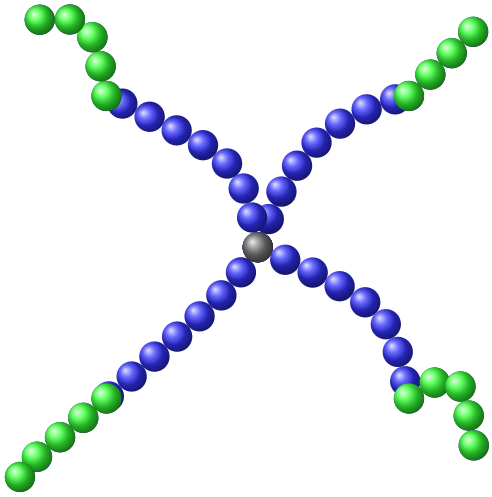

Figure 3.2: Schematic illustration of a telechelic star polymer (TSP). The (gray) core monomer has four polymer chains attached to it, each of which consists of a solvophilic part close to the core (blue monomers), and a solvophobic part near the free ends of the arms (green monomers).

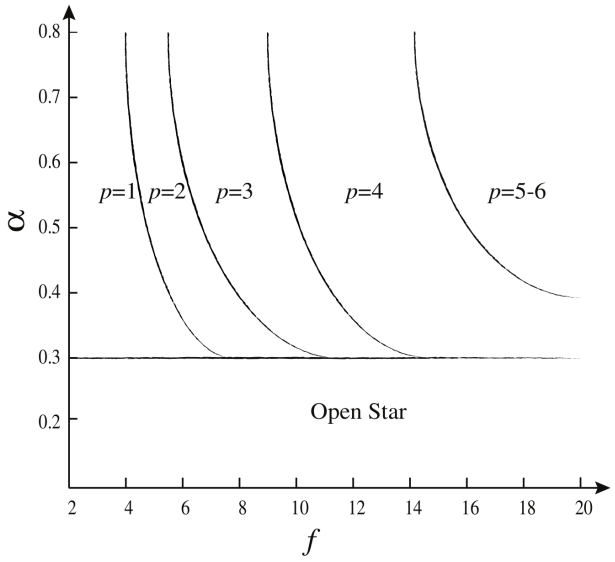

Figure 3.3: The mean number of patches, p, in a telechelic star polymer (TSP), as a function of the number of arms f and of the asymmetry ratio α. Image reproduced unaltered from Capone et al.[7] in compliance with the CC BY 3.0[8] license.

In addition to the self-assembly of the TSPs, Capone et al.[9] demonstrated in their computer simulations that dense solutions of these TSPs may aggregate into large-scale structures, where simple cubic or diamond lattices are mechanically stable, depending on the number of patches p per TSP.

Since both f and α are set during (hypothetical) chemical synthesis, and the solvent or its temperature may be hard to change in a controlled (and, if required, fast) manner in experiments – e.g. in order to investigate possible transitions from one lattice to another – Blaak and Likos[10] suggested another system of star polymers as an alternative to the TSPs above. There, intra-star clustering is not achieved by solvophobicity, but rather by decorating the (now homogeneous) polymer arms' free ends with a particle carrying a super-paramagnetic dipole moment. It is this type of *magnetically functionalized star polymers* that is studied in this chapter.

3.2 MFSP Model[11]

Rather than simulating the molecule atom by atom, the magnetically functionalized star polymer (MFSP) is modeled as a collection of effective monomers, like in the Kremer-Grest model introduced in Section 2.5, but with generalized potentials discussed below. The MSFPs are represented by monomers (also referred to as *particles*) of three types: core particles (denoted below by the subscript C), arm particles (A), and magnetic particles (M). A star polymer has exactly one core particle, attached to which are f linear polymers arms, each containing n_A arm particles. Additionally, at the free end of each arm, a super-paramagnetic particle is attached, so that a star polymer consists of a total of $N = 1 + f\,(n_\mathrm{A} + 1)$ monomers. Fig. 3.4 shows a snapshot of such a macromolecule.

[7] B. Capone, I. Coluzza, R. Blaak, F. Lo Verso, and C. N. Likos. "Hierarchical self-assembly of telechelic star polymers: from soft patchy particles to gels and diamond crystals". *New Journal of Physics* **15** (2013), 095002. Figure 2.

[8] *Creative Commons Attribution 3.0 Unported (CC BY 3.0).* URL: `https://creativecommons.org/licenses/by/3.0/legalcode`.

[9] Capone, Coluzza, LoVerso, Likos, and Blaak, "Telechelic Star Polymers as Self-Assembling Units from the Molecular to the Macroscopic Scale".

[10] Blaak and Likos, "Self-assembly of magnetically functionalized star-polymer nano-colloids".

[11] Blaak and Likos, "Self-assembly of magnetically functionalized star-polymer nano-colloids".

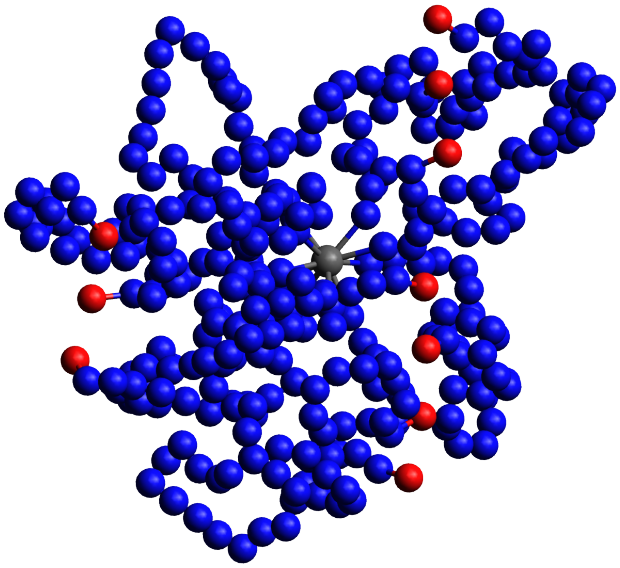

Figure 3.4: Simulation snapshot of a star polymer in a strong magnetic field (along the vertical direction). The core particle is shown in gray, the arm particles are colored in blue, and the magnetic particles are colored red. Note the monomer-type–dependent inter-particle distances and the formation of columns of magnetic particles parallel to the magnetic field.

Each monomer is assumed to be spherically symmetric, and to consist of two concentric parts: an inner, hard-core part with diameter D_α (where α represents one of the particle types C, A, and M), and an outer, "soft" part with a thickness of σ_α; the total diameter of the particles is thus $D_\alpha + \sigma_\alpha$. The particle masses are taken to be identical for all monomer types.

As far as the author knows, MFSPs have not yet been synthesized or otherwise observed in nature, but the model and its parameters (cf. Section 3.2.2 below) have been chosen such that it is believed that chemical synthesis of such MFSPs is feasible.[12]

3.2.1 Interaction Potentials

Any pair of two monomers (of types α and β, respectively) interact via a modified Weeks-Chandler-Andersen (WCA) potential, Eq. (2.13), which is still purely repulsive, but now takes into account both the impenetrable hard cores with diameters D_α and D_β of the involved

[12]Blaak and Likos, "Self-assembly of magnetically functionalized star-polymer nano-colloids", Section 1.

particles, as well as their soft-core diameters σ_α and σ_β:

$$V_{\mathrm{WCA}}(r) := \begin{cases} 4\epsilon_{\alpha\beta}\left[\left(\frac{\sigma_{\alpha\beta}}{r-D_{\alpha\beta}}\right)^{12} - \left(\frac{\sigma_{\alpha\beta}}{r-D_{\alpha\beta}}\right)^{6} + \frac{1}{4}\right] & \text{if } (r-D_{\alpha\beta}) \leq 2^{1/6}\sigma_{\alpha\beta}, \\ 0 & \text{else.} \end{cases} \tag{3.1}$$

Here, r is the distance between the centers of the two interacting monomers, $D_{\alpha\beta} := (D_\alpha + D_\beta)/2$ and $\sigma_{\alpha\beta} := (\sigma_\alpha + \sigma_\beta)/2$ are the mean hard- and soft-core diameters, respectively (Lorentz mixing rule[13,14]), and $\epsilon_{\alpha\beta} := \sqrt{\epsilon_\alpha \epsilon_\beta}$ defines the interaction strength in accordance with the Berthelot mixing rule.[15,16]

In addition to $V_{\mathrm{WCA}}(r)$, (i) pairs of particles that are considered to be directly chemically connected, i.e. neighboring monomers within the same arm, (ii) the magnetic monomers and their respective neighbor arm monomers, and (iii) the core monomer and its directly connected arm monomers, interact via a generalized FENE potential

$$V_{\mathrm{FENE}}(r) := -\frac{1}{2}K_{\alpha\beta}R_{\alpha\beta}^2 \ln\left[1 - \left(\frac{r-l_{\alpha\beta}}{R_{\alpha\beta}}\right)^2\right], \tag{3.2}$$

where $l_{\alpha\beta}$ is the equilibrium bond length between two particles of types α and β, $R_{\alpha\beta}$ is the maximum deviation from that equilibrium length, and $K_{\alpha\beta}$ scales the interaction strength.

Finally, the magnetic particles interact with one another via the dipole-dipole-interaction[17,18]

$$V_{\mathrm{M}}(\mathbf{r}) := -\frac{\mu_0}{4\pi r^3}\left(3\left(\mathbf{m}_1 \cdot \hat{\mathbf{r}}\right)\left(\mathbf{m}_2 \cdot \hat{\mathbf{r}}\right) - \mathbf{m}_1 \cdot \mathbf{m}_2\right), \tag{3.3}$$

with μ_0 being the vacuum permeability constant, $\mathbf{m}_1$ and $\mathbf{m}_2$ being the magnetic dipole moments of the two particles involved, $\mathbf{r}$ being the connecting vector with $r = |\mathbf{r}|$, and $\hat{\mathbf{r}} = \mathbf{r}/r$ being the associated unit vector. To simplify the model, it is assumed that the super-paramagnetic end monomers have their dipole moment always perfectly aligned along the spatially homogeneous external magnetic field $\mathbf{B}$ with magnitude $B = |\mathbf{B}|$ and unit vector $\hat{\mathbf{B}} = \mathbf{B}/B$. Furthermore,

[13] H. A. Lorentz. "Ueber die Anwendung des Satzes vom Virial in der kinetischen Theorie der Gase". *Annalen der Physik* **248** (1881), 127.

[14] M. P. Allen and D. J. Tildesley. *Computer Simulation of Liquids.* Reprint by The Ipswich Book Co Ltd in 1991. Clarendon Press, 1987.

[15] D. Berthelot. "Sur le mélange des gaz". *Comptes rendus hebdomadaires des séances de l'Académie des Sciences* **126** (1898), 1703.

[16] Allen and Tildesley, *Computer Simulation of Liquids.*

[17] J. D. Jackson. *Classical Electrodynamics.* 3rd ed. John Wiley & Sons, 1999, Eq. (5.56) in conjunction with Eq. (5.72).

[18] E. P. Furlani. *Permanent Magnet and Electromechanical Devices. Materials, Analysis, and Applications.* 1st ed. Academic Press Series in Electromagnetism. Academic Press, 2001, Eq. (3.128).

the magnetic dipole moments are assumed to be equal in magnitude, such that, for any magnetic particle i, $\mathbf{m}_i = m\hat{\mathbf{B}}$ with constant m. This assumption allows one to simplify Eq. (3.3), leading to

$$V_{\mathrm{M}}(\mathbf{r}) = -\lambda \frac{k_{\mathrm{B}} T a_0^3}{r^3} \left[3 \left(\hat{\mathbf{B}} \cdot \hat{\mathbf{r}} \right)^2 - 1 \right], \tag{3.4}$$

where the dimensionless parameter $\lambda := \mu_0 m^2 / (4\pi k_{\mathrm{B}} T a_0^3)$ will be called *magnetic interaction strength* in what follows, and $k_{\mathrm{B}}T$ and a_0 are the energy and length scales, respectively (see below).

3.2.2 Interaction Parameters

The three interactions $V_{\mathrm{WCA}}(\mathbf{r})$, $V_{\mathrm{FENE}}(\mathbf{r})$, and $V_{\mathrm{M}}(\mathbf{r})$ introduced above are specified by a large number of model parameters. Varying them all independently would be prohibitively complex; hence, the WCA energy scales ϵ_α are set to unity in units of $k_{\mathrm{B}}T$ (k_{B} being Boltzmann's constant, and T the temperature) for all particle types α; likewise, the soft-core diameters σ_α are set to unity in terms of the MPCD length unit a_0 (see Chapter 6).

The arm monomers are assumed to have no hard core, i.e. $D_{\mathrm{A}} = 0$, as in the traditional Kremer-Grest model[19] (cf. Section 2.5). The magnetic monomers are modeled as having a hard core of diameter $D_{\mathrm{M}} = a_0$ (corresponding to the impenetrable super-paramagnetic material) and $\sigma_{\mathrm{M}} = a_0$; in contrast, the core particle is assumed to have $D_{\mathrm{M}} = 2a_0$, so that the core's spherical surface is large enough to accommodate a sufficiently large number f of attached arms. Note that, in order to keep the model as simple as possible, the arms may move freely around the core, rather than each being grafted to a particular location on the core monomer's surface, as would probably be the case were the MFSP to be realized in an experiment. Similarly, there is no surface anchoring at the magnetic particles either: the point connecting a magnetic monomer to the rest of its polymer arm can freely move on the magnetic monomer's surface.

In Eq. (3.2), the FENE equilibrium length $l_{\alpha\beta}$ is set to $D_{\alpha\beta}$, and the maximum bond length deviation is assumed to be $R_{\alpha\beta} = 1.5\sigma_{\alpha\beta}$ for all α and β. The FENE interaction strength is set to $K_{\alpha\beta} = 30\epsilon_{\alpha\beta}\sigma_{\alpha\beta}^{-2}$.

Finally, the parameter λ is varied in order to study the influence of the magnetic interaction strength on the system's behavior.

[19] Kremer and Grest, "Molecular dynamics (MD) simulations for polymers".

The model is compatible with the one used by Blaak and Likos[20], except that in their contribution, pure Molecular Dynamics (MD) without an explicit solvent is used, such that no hydrodynamic interaction is present. Furthermore, their FENE interaction strength is half of the one used in this thesis. Blaak and Likos[21] discuss the MFSP system for various numbers of arms f and numbers n_A of non-magnetic monomers per arm, and report qualitatively similar results (e.g. regarding size and shape descriptors, cf. Section 3.5.2) in most cases. Therefore, in the interest of computational efficiency, the novel data presented here are based on stars with $f = 10$ and $n_\mathrm{A} = 30$.

Regarding the magnetic particles, the parameter choices above are commensurate with a real-world hard-core diameter of about 10 nm, consisting e.g. of super-paramagnetic ferumoxide[22] with a 10 nm soft-core coating diameter, such that $\lambda \approx 100$ is realistically achievable.[23]

3.3 Forces on Magnetic Monomers

Having specified the interaction potentials above, one can perform a few simple calculations in order to develop a better understanding of the (expected) behavior of a MFSP. In this section it will be shown that (i) the magnetic dipole-dipole interaction favors an arrangement of magnetic monomers along the external magnetic field, (ii) that positioning magnetic moments side-by-side in a direction orthogonal to the external field leads to repulsion, and (iii) how one regime crosses into the other, depending on the angle between the connection vector $\hat{\mathbf{r}}$ and the external field direction $\hat{\mathbf{B}}$.

Therefore, at first glance it stands to reason that energetically, MFSPs would strive to arrange all magnetic monomers along one straight line parallel to $\hat{\mathbf{B}}$, thereby forming a single *column* or *cluster* of magnetic monomers. This would indeed be the case, if one were to neglect energetic costs of stretching individual arms long enough to allow their ends to reach the magnetic column. Depending on the number of arms f and the number n_A of non-magnetic monomers per arm, little to no stretching may be required, but for large f and small n_A, such a linear arrangement may be energetically expensive or, due to the finite extensibility of the FENE bonds, outright impossible.

[20] Blaak and Likos, "Self-assembly of magnetically functionalized star-polymer nano-colloids".
[21] Blaak and Likos, "Self-assembly of magnetically functionalized star-polymer nano-colloids".
[22] C. W. Jung and P. Jacobs. "Physical and chemical properties of superparamagnetic iron oxide MR contrast agents: Ferumoxides, ferumoxtran, ferumoxsil". *Magnetic Resonance Imaging* **13** (1995), 661.
[23] Blaak and Likos, "Self-assembly of magnetically functionalized star-polymer nano-colloids", Section 2.

Aside from this complication, steric obstruction (particularly near the star polymer core) may hinder the formation of a one-cluster star. Finally, random motion induced by thermal and hydrodynamic fluctuations acts to avoid the entropically disadvantageous constrained configurations, where a large number of magnetic monomers are allowed to explore only a narrow section of phase-space due to their being restricted to a single magnetic cluster.

3.3.1 Forces due to Magnetic Dipole-Dipole-Interaction

Given two magnetic dipole moments $\mathbf{m}_1$ and $\mathbf{m}_2$, and the vector $\mathbf{r}$ pointing from the moment $\mathbf{m}_1$ to $\mathbf{m}_2$, the force $\mathbf{F}_\mathrm{M}$ exerted on the moment $\mathbf{m}_2$ due to the general magnetic interaction potential V_M, Eq. (3.3), can be shown to be given by[24,25]

$$\mathbf{F}_\mathrm{M}(\mathbf{r}) = \frac{3\mu_0}{4\pi r^5}\left[(\mathbf{m}_1\cdot\mathbf{m}_2)\,\mathbf{r} + (\mathbf{m}_1\cdot\mathbf{r})\,\mathbf{m}_2 + (\mathbf{m}_2\cdot\mathbf{r})\,\mathbf{m}_1 - 5r^{-2}\,(\mathbf{m}_1\cdot\mathbf{r})\,(\mathbf{m}_2\cdot\mathbf{r})\,\mathbf{r}\right].$$

With the simplifying assumptions set forth in Section 3.2.1, this reduces to

$$\begin{aligned}\mathbf{F}_\mathrm{M}(\mathbf{r}) &= \frac{3\lambda}{r^5}k_\mathrm{B}Ta_0^3\left[\mathbf{r} + 2\left(\hat{\mathbf{B}}\cdot\mathbf{r}\right)\hat{\mathbf{B}} - 5r^{-2}\left(\hat{\mathbf{B}}\cdot\mathbf{r}\right)\left(\hat{\mathbf{B}}\cdot\mathbf{r}\right)\mathbf{r}\right]\\ &= \frac{3\lambda}{r^4}k_\mathrm{B}Ta_0^3\left[\left(1 - 5\left(\hat{\mathbf{B}}\cdot\hat{\mathbf{r}}\right)^2\right)\hat{\mathbf{r}} + 2\left(\hat{\mathbf{B}}\cdot\hat{\mathbf{r}}\right)\hat{\mathbf{B}}\right].\end{aligned}$$

Let $\hat{\mathbf{B}}$, the direction of the external magnetic field, serve as one of the unit vectors of a new Cartesian coordinate system, and let $\hat{\mathbf{A}}$ and $\hat{\mathbf{C}}$ denote the other two, orthogonal but otherwise arbitrarily chosen unit vectors. Writing $\hat{\mathbf{r}} = \rho_A\hat{\mathbf{A}} + \rho_B\hat{\mathbf{B}} + \rho_C\hat{\mathbf{C}}$ in terms of these unit vectors, one has $\hat{\mathbf{B}}\cdot\hat{\mathbf{r}} = \rho_B$ and

$$\mathbf{F}_\mathrm{M}(\mathbf{r}) = \frac{3\lambda}{r^4}k_\mathrm{B}Ta_0^3\left(\left(1 - 5\rho_B^2\right)\hat{\mathbf{r}} + 2\rho_B\hat{\mathbf{B}}\right), \tag{3.5}$$

leading to a force of magnitude

$$F_\mathrm{M}(r) = \frac{3\lambda}{r^4}k_\mathrm{B}Ta_0^3\sqrt{1 - 2\rho_B^2 + 5\rho_B^4}.$$

[24] Furlani, *Permanent Magnet and Electromechanical Devices*, Equation (3.130).

[25] K. W. Yung, P. B. Landecker, and D. D. Villani. "An Analytic Solution for the Force Between Two Magnetic Dipoles". *Magnetic and Electrical Separation* **9** (1998), 39. Equation (37) (NB: in the second equality, all hats of m_a, m_b should be vector arrows), and Equation (42).

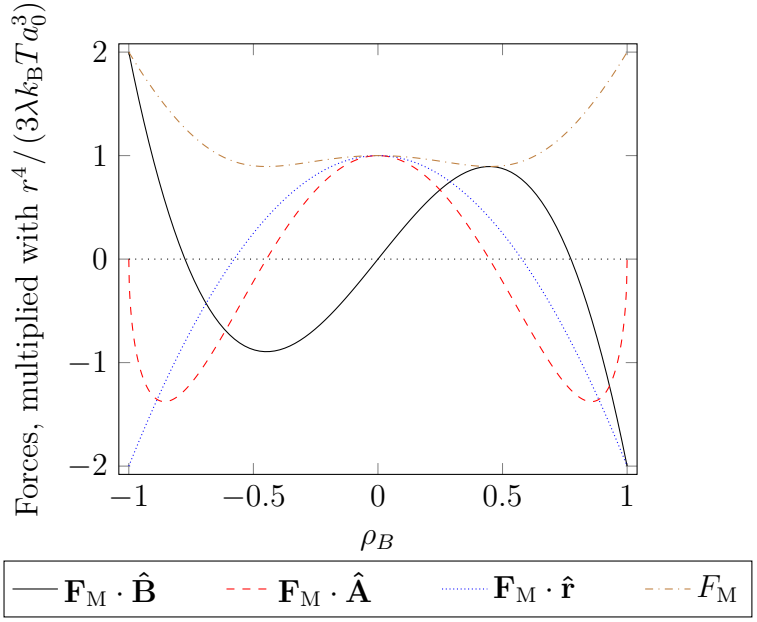

Figure 3.5: Projections of the magnetic force $\mathbf{F}_\mathrm{M}$ onto different directions (as labeled) as well as the total force magnitude F_M, as a function of ρ_B and for constant r. The horizontal loosely dotted line is a guide for the eye, showing where forces are zero. See text of Section 3.3.1 for details.

Of this force, the amount acting on the moment $\mathbf{m}_2$ along the direction of $\hat{\mathbf{B}}$ is

$$\mathbf{F}_\mathrm{M} \cdot \hat{\mathbf{B}} = \frac{3\lambda}{r^4} k_\mathrm{B} T a_0^3 \rho_B \left(3 - 5\rho_B^2\right).$$

The remaining component, i.e. the force acting perpendicular to $\hat{\mathbf{B}}$, can more easily be computed by assuming, without loss of generality, $\rho_C = 0$, so that $\hat{\mathbf{A}}$ can be considered *the* direction orthogonal to $\hat{\mathbf{B}}$. Then, with $\rho_A^2 + \rho_B^2 = 1$ (since $\rho_C = 0$),

$$\mathbf{F}_\mathrm{M} \cdot \hat{\mathbf{A}} = \frac{3\lambda}{r^4} k_\mathrm{B} T a_0^3 \left(1 - 5\rho_B^2\right) \sqrt{1 - \rho_B^2}. \tag{3.6}$$

Projecting the force vector onto $\hat{\mathbf{r}}$, one finds

$$\mathbf{F}_\mathrm{M} \cdot \hat{\mathbf{r}} = \frac{3\lambda}{r^4} k_\mathrm{B} T a_0^3 \left(1 - 3\rho_B^2\right).$$

The projected forces computed above, as well as the force magnitude F_M, are plotted in Fig. 3.5, for constant r and as a function of ρ_B. Introducing the angle θ between $\hat{\mathbf{B}}$ and $\hat{\mathbf{r}}$, one can instead express the forces (with constant r) as functions of θ via $\hat{\mathbf{B}} \cdot \hat{\mathbf{r}} = \left|\hat{\mathbf{B}}\right| |\hat{\mathbf{r}}| \cos(\theta) = \cos(\theta) = \rho_B$, as is done in Fig. 3.6.

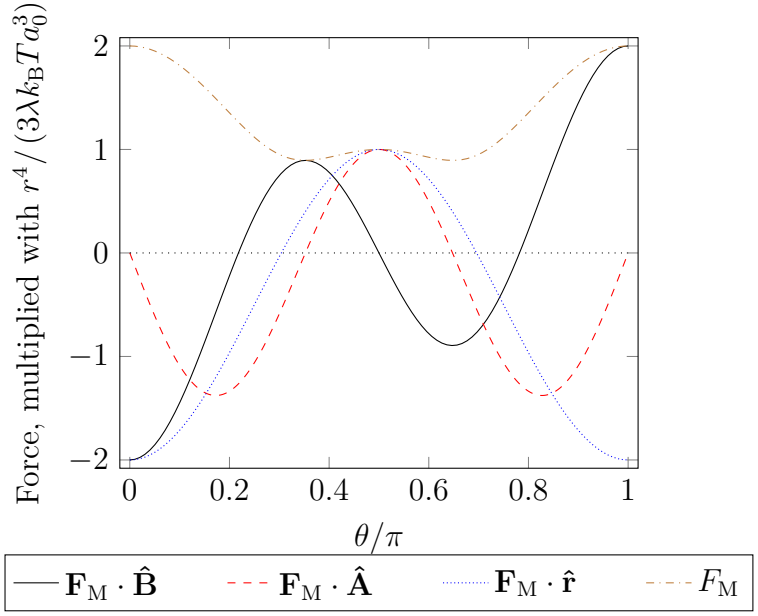

Figure 3.6: Projections of the magnetic force $\mathbf{F}_M$, as in Fig. 3.5, except that they are expressed as functions of $\theta/\pi = \arccos(\rho_B)/\pi$ rather than ρ_B.

3.3.2 Forces due to the WCA Excluded Volume Interaction

The potential V_{WCA} (cf. Eq. (3.1)), which models the excluded volume effect, gives rise to a force

$$\mathbf{F}_{\text{WCA}}(\mathbf{r}) := \begin{cases} 24\epsilon_{\alpha\beta} \frac{\hat{\mathbf{r}}}{r-D_{\alpha\beta}} \left[2\left(\frac{\sigma_{\alpha\beta}}{r-D_{\alpha\beta}}\right)^{12} - \left(\frac{\sigma_{\alpha\beta}}{r-D_{\alpha\beta}}\right)^{6} \right] & \text{if } (r - D_{\alpha\beta}) \leq 2^{1/6}\sigma_{\alpha\beta}, \\ 0 & \text{else,} \end{cases} \tag{3.7}$$

acting on the monomer i, if $\mathbf{r} = \mathbf{r}_i - \mathbf{r}_{i-1}$ points from monomer $i-1$ to monomer i.

3.3.3 Force Balance with $\hat{\mathbf{r}} \parallel \hat{\mathbf{B}}$

In a configuration where $\hat{\mathbf{r}} \parallel \hat{\mathbf{B}}$ (i.e. $\rho_B = 1$), force balance is achieved when $-\mathbf{F}_M \cdot \hat{\mathbf{r}} = \mathbf{F}_{\text{WCA}} \cdot \hat{\mathbf{r}}$, i.e. when either $r = \infty$, or when $r \leq \left(2^{1/6}\sigma_{\alpha\beta} + D_{\alpha\beta}\right)$ and

$$\frac{6\lambda}{r^4} k_B T a_0^3 = \frac{24\epsilon_{\alpha\beta}}{r - D_{\alpha\beta}} \left[2\left(\frac{\sigma_{\alpha\beta}}{r - D_{\alpha\beta}}\right)^{12} - \left(\frac{\sigma_{\alpha\beta}}{r - D_{\alpha\beta}}\right)^{6} \right].$$

With the choice of the interaction parameters outlined in Section 3.2.2, this relation can be written as

$$\frac{\lambda}{4} = a_0^{-3} \frac{r^4}{r - a_0} \left[2 \left(\frac{a_0}{r - a_0} \right)^{12} - \left(\frac{a_0}{r - a_0} \right)^{6} \right].$$

the numerical solution of which gives $r \approx 1.97\, a_0$ for $\lambda = 100$, and $r \approx 1.93\, a_0$ for $\lambda = 200$. This demonstrates that an increase in the magnetic interaction strength leads only to a modest reduction of the equilibrium distance between magnetic particles, due to the steep slope of the WCA potential at short distances.

Of course, a full treatment of the balance of forces between two magnetic monomers would require a (statistical) analysis of contributions due to FENE bonds, thermal fluctuations, and hydrodynamic interactions. However, comparison with simulation data shows that the two-force approximation employed above closely reproduces the observed equilibrium distance.

3.4 Equilibrium Behavior[26]

In order to provide useful a context for the new research results presented in subsequent sections, this section summarizes key findings by Blaak and Likos,[27] who study a single MFSP using Molecular Dynamics (cf. Chapter 6) at constant temperature, but without hydrodynamic interactions.

Fig. 3.7 shows, in the top panel, the mean number N_C of magnetic clusters that are present at a given moment in a MFSP, depending on the functionality (number of arms) f, and the magnetic interaction strength λ. Both here and in the novel results described in subsequent sections, a magnetic cluster is defined to be a group of magnetic monomers where each monomer is separated from another member of the cluster by not more than $2.5\, a_0$, measured from center to center. This length corresponds to about 125% of the WCA-FENE-equilibrium distance calculated in Section 3.3.3.

[26] Blaak and Likos, "Self-assembly of magnetically functionalized star-polymer nano-colloids".
[27] Blaak and Likos, "Self-assembly of magnetically functionalized star-polymer nano-colloids".
[28] R. Blaak and C. N. Likos. "Self-assembly of magnetically functionalized star-polymer nano-colloids". *The European Physical Journal E* **41** (2018), 3. Figure 2.
[29] *Creative Commons Attribution 4.0 International (CC BY 4.0).* URL: `https://creativecommons.org/licenses/by/4.0/legalcode`.

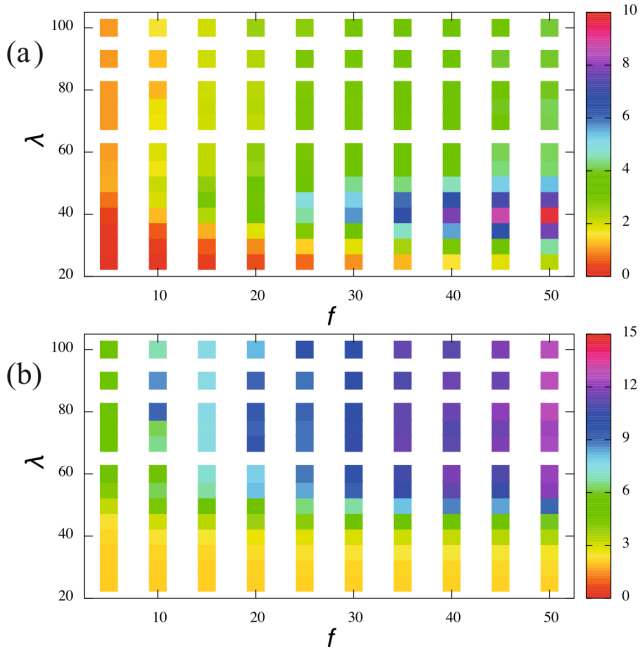

Figure 3.7: Average number N_C of magnetic clusters (a), and mean number of magnetic monomers per magnetic cluster (b), as functions of the number of arms f in the MFSP and the magnetic interaction strength λ. Each arm has $n_A = 50$ non-magnetic arm particles. Image reproduced unaltered from Blaak and Likos[28] in compliance with the CC BY 4.0[29] license.

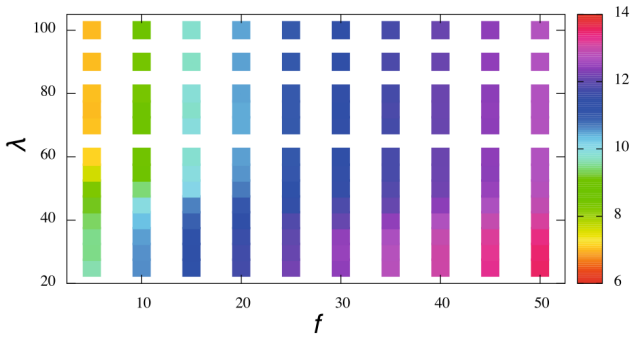

Figure 3.8: Radius of gyration R_g as a function of the number of arms f in the MFSP and the magnetic interaction strength λ. Each arm has $n_A = 50$ non-magnetic arm particles. Image reproduced unaltered from Blaak and Likos[31] in compliance with the CC BY 4.0[32] license.

Blaak and Likos[30] define a cluster to consist of at least two magnetic particles. Their data, visualized in Fig. 3.7, document fundamental trends: For the lowest magnetic interaction strengths considered, i.e. $\lambda = 25$, only few magnetic clusters occur, and those clusters that do form mostly consist of only two magnetic monomers. These clusters merely correspond to monomers spontaneously and randomly meeting; they are hardly stable enough to persist until a third magnetic monomer joins the aggregate.

The situation changes as λ approaches 40. Then, especially for high f, the number of clusters rises with growing f, as does the average size of a cluster. This is compatible with the interpretation that with sufficiently large λ, magnetic clusters become stable enough to merge with other clusters or single magnetic monomers, but are still prone to breaking due to thermal fluctuations.

As one increases λ further, the number of clusters decreases again. This decrease goes hand in hand with an increase of the average cluster size; now, the magnetic interaction bestows the clusters with enough stability for them to persist for long times, such that they have ample opportunity to aggregate into groups of ten or more magnetic monomers.

[30] Blaak and Likos, "Self-assembly of magnetically functionalized star-polymer nano-colloids".
[31] R. Blaak and C. N. Likos. "Self-assembly of magnetically functionalized star-polymer nano-colloids". *The European Physical Journal E* **41** (2018), 3. Figure 2.
[32] *Creative Commons Attribution 4.0 International (CC BY 4.0).* URL: `https://creativecommons.org/licenses/by/4.0/legalcode`.

Fig. 3.8 shows the radius of gyration R_g of the star polymer, which serves as a measure of the MFSP's overall size, thoroughly defined in Section 3.5.2. In this figure, two general trends can be observed: As one increases the number of arms f, and thus the total number of monomers, the MFSP grows in size. By increasing the magnetic interaction strength λ, however, one can force the MFSP into more compact configurations, because restraining the free ends of the arms in their respective magnetic clusters reduces the mean distance of monomers from the star's core.

3.5 Behavior under Shear

In this thesis, MFSPs are studied in the presence of hydrodynamic interactions (see Chapter 6 for simulation details); further, the system is driven out of equilibrium by applying a linear shear flow to the solvent (cf. Section 6.1.3). That is, the solvent's flow field $\mathbf{u}$ (in the absence of MFSPs, which may hinder the free flow of the solvent[33]) on average obeys $\mathbf{u}(x, y, z) = (y - y_0)\dot{\gamma}\hat{\mathbf{e}}_x$. Here, the axes of the Cartesian coordinate system are chosen such that the *shear flow direction* is along the x axis, the *shear gradient direction* is along the y axis, and the *shear vorticity direction* is along the z axis. $y = y_0$ is the plane where there is no net shear flow, and y_0 may be set to 0 by a suitable choice of coordinate system. The *shear rate* $\dot{\gamma} := \mathrm{d}u_x/\,\mathrm{d}y$ is a measure for the strength of the flow field.

Having thus distinguished two axes, the flow and gradient direction – and the vorticity axis by implication –, one is now free to choose a direction for the external magnetic field $\hat{\mathbf{B}}$. It is apparent from Eq. (3.4) that a simple change of sign $\hat{\mathbf{B}} \mapsto -\hat{\mathbf{B}}$ leaves the system invariant, but a lot of freedom remains in the choice of the relative orientation of $\hat{\mathbf{B}}$ with regard to the shear flow geometry. In this work, three principal scenarios are investigated, corresponding to having $\hat{\mathbf{B}}$ point along the x, y, and z axis, respectively.

[33] M. Ripoll, R. G. Winkler, and G. Gompper. "Hydrodynamic screening of star polymers in shear flow". *The European Physical Journal E* **23** (2007), 349.

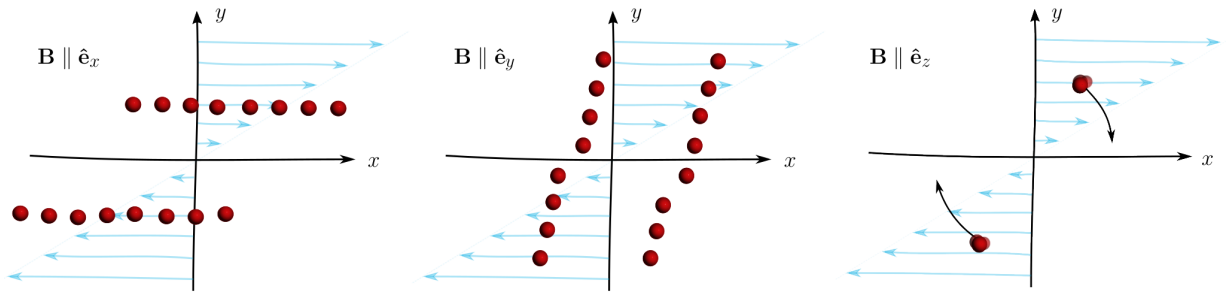

Figure 3.9: Sketches of the three geometries considered in this thesis. In all cases, the shear flow direction is chosen along the x axis, and the shear gradient direction along the y axis; the blue arrows indicate the linear shear flow profile that would develop in absence of a solute such as the star polymer, with longer arrows corresponding to faster solvent flows. In the left, middle, and right panel, respectively, the external magnetic field $\hat{\mathbf{B}}$ is chosen along the x, y, and z axes, and the magnetic monomers (red spheres) are aligned accordingly. Arm monomers and the core monomer are not shown, and the curved arrows in the right panel suggest a net rotation of the MFSP. The author would like to thank Angela Koffler for help in creating this figure.

Fig. 3.9 shows sketches for the three separate cases. The illustrations are constructed by first visualizing the shear flow profile of the solvent (blue arrows), then choosing a direction for $\hat{\mathbf{B}}$, and then simplistically assuming that the magnetic monomers (red spheres) are arranged along that direction. Finally, one may imagine, in a naive Gedankenexperiment, what effect the shear flow would have on the magnetic columns. It seems plausible that in the case where $\hat{\mathbf{B}} \parallel \hat{\mathbf{e}}_x$ (left panel of Fig. 3.9), the top magnetic column might be moved to the right and the bottom column to the left, to the extent the polymer arms allow. In the case $\hat{\mathbf{B}} \parallel \hat{\mathbf{e}}_y$ (middle panel), moving the magnetic monomers in the positive y half-plane to the right and the bottom ones to the left would tend to break the magnetic columns, and thus reduce stability of the clusters. Finally, for $\hat{\mathbf{B}} \parallel \hat{\mathbf{e}}_z$ (right panel), one might imagine that the clusters, all of their respective members being at roughly the same x and y coordinates, would experience similar local flows, and would thus not be broken apart as easily; more interestingly, though, the fact that the columns can not move away indefinitely from the MFSP's core (not shown in the figure) may suggest that the columns, and thus the MFSP as a whole, may undergo a rotational movement about the z axis.

In the following subsections, it will be argued that these pictures indeed reflect the behavior of MFSPs under shear flow. Also, the case will be made that the physical quantities extracted from the simulations can be loosely put into one of four categories:

1. The mean number of magnetic clusters, N_{C}, which forms its own category due to the important role it plays in many of the other properties;

2. Size and shape descriptors, which are largely controlled by the number of clusters that are formed at a particular set of values for $\dot{\gamma}$, $\hat{\mathbf{B}}$, and λ;

3. Quantities that are qualitatively unaffected by the presence of magnetic interactions, i.e. behave for MFSPs similarly as for non-magnetic star polymers; and

4. Properties that have a N_{C}-dependence, but *additionally* strongly depend on the shear rate $\dot{\gamma}$.

All simulations correspond to stars with $f = 10$ arms per star, and $n_{\mathrm{A}} = 30$ non-magnetic particles per arm. The masses of the individual monomers were set uniformly to $m = 5\, m_{\mathrm{MPCD}}$, where m_{MPCD} is the MPCD mass unit (cf. Chapter 6). Simulations for different magnetic field directions $\hat{\mathbf{B}}$, magnetic interaction strengths λ, and shear rates $\dot{\gamma}$ have been carried out independently from one another, except that they draw their initial MFSP configurations from a pool of 16 possible, independent snapshots that have been created under equilibrium conditions. Data collection was started only after a steady state had been reached in the out-of-equilibrium flow (see Chapter 6 for details.)

It should be mentioned that the case $\hat{\mathbf{B}} = \hat{\mathbf{e}}_x$ with $\lambda = 200$ has not been investigated for the following reason: The studies had started with the three cases for $\lambda = 100$, after which the thesis author concluded that $\hat{\mathbf{B}} = \hat{\mathbf{e}}_z$ was (subjectively) the most interesting case, and that $\hat{\mathbf{B}} = \hat{\mathbf{e}}_x$ was relatively similar to $\hat{\mathbf{B}} = \hat{\mathbf{e}}_y$. Rather than running computer experiments for the latter two cases and $\lambda = 200$, it was decided to disregard the $\hat{\mathbf{B}} = \hat{\mathbf{e}}_x$ orientation in favor of additional simulations, and thus improved statistics in the analyzed quantities, for the other five scenarios.

3.5.1 Number N_C of Magnetic Clusters

Turning to the behavior of the magnetic clusters first, Fig. 3.10 shows the mean number N_C of magnetic clusters as a function of the shear rate $\dot{\gamma}$, for various combinations of the direction of the external magnetic field, $\mathbf{B}$, and the magnetic interaction strength λ. Note that, in contrast to Fig. 3.7, magnetic clusters are now understood to include the case of single magnetic monomers.

For low shear rates, the number of clusters is approximately two, as is the case in the equilibrium study of Blaak and Likos[34], with different choices of the direction $\hat{\mathbf{B}}$ or strength λ of the external magnetic field having only negligible effect. At a critical shear rate $\dot{\gamma}^*(\hat{\mathbf{B}}, \lambda)$, which, depending on $\hat{\mathbf{B}}$ and λ, varies between about $\dot{\gamma}^*(\hat{\mathbf{e}}_y, 100) = 4 \cdot 10^{-3}/t_{\mathrm{MPCD}}$ and $\dot{\gamma}^*(\hat{\mathbf{e}}_z, 200) = 5 \cdot 10^{-2}/t_{\mathrm{MPCD}}$ for the presented data (t_{MPCD} being the time unit in MPCD simulations), the mean number of magnetic clusters starts to increase with increasing shear rates $\dot{\gamma}$.

First, it can be noted that the qualitative hypotheses put forth in Section 3.5 regarding the stability of clusters for various $\hat{\mathbf{B}}$ are confirmed: For a given λ, $\hat{\mathbf{B}} \parallel \hat{\mathbf{e}}_y$ yields the most unstable clusters, while for $\hat{\mathbf{B}} \parallel \hat{\mathbf{e}}_z$, the shear flow is least capable of breaking magnetic clusters. As expected, an increase in λ promotes cluster stability.

Second, the increase in the number N_C of clusters with increasing $\dot{\gamma}$ is of logarithmic nature, $N_C \propto \ln(\dot{\gamma})$, corresponding to straight lines in the semi-logarithmic representation of Fig. 3.10. This indicates that the shear forces for a given shear rate cause clusters above a certain ($\dot{\gamma}$-dependent) size to break, while leaving smaller clusters intact; An alternative, but now falsified, hypothesis would have been that there is a critical shear rate below which clusters are stable, but above which all clusters are broken up into their monomeric constituents.

Third, one may note that the slopes of the curves in Fig. 3.10 are approximately equal. One can thus introduce a scaling time, $\tau^*(\hat{\mathbf{B}}, \lambda)$, that is empirically defined, depending on $\hat{\mathbf{B}}$ and λ, such that the data in Fig. 3.10 collapse onto a single master curve, with the transition from constant $N_C \approx 2$ to $N_C \propto \ln(\dot{\gamma})$ appearing at approximately $\tau^*(\hat{\mathbf{B}}, \lambda) \cdot \dot{\gamma} \approx 1$, as is done in Fig. 3.11. Performing a least-square fit of the data in the region $\tau^*(\hat{\mathbf{B}}, \lambda) \cdot \dot{\gamma} > 1$, where the master curve in the semi-logarithmic Fig. 3.11 appears to describe a straight line, against the linear equation $N_C = k \ln(\dot{\gamma}) + d$, one finds $k \approx 2.04 \pm 0.04$ and $d \approx 2.26 \pm 0.07$ for $\hat{\mathbf{B}} = \hat{\mathbf{e}}_y$, $\lambda = 100$ (the curve with the largest range in the scaled shear rates). The heuristic values for $\tau^*(\hat{\mathbf{B}}, \lambda)$ are listed in Table 3.1.

[34] Blaak and Likos, "Self-assembly of magnetically functionalized star-polymer nano-colloids".

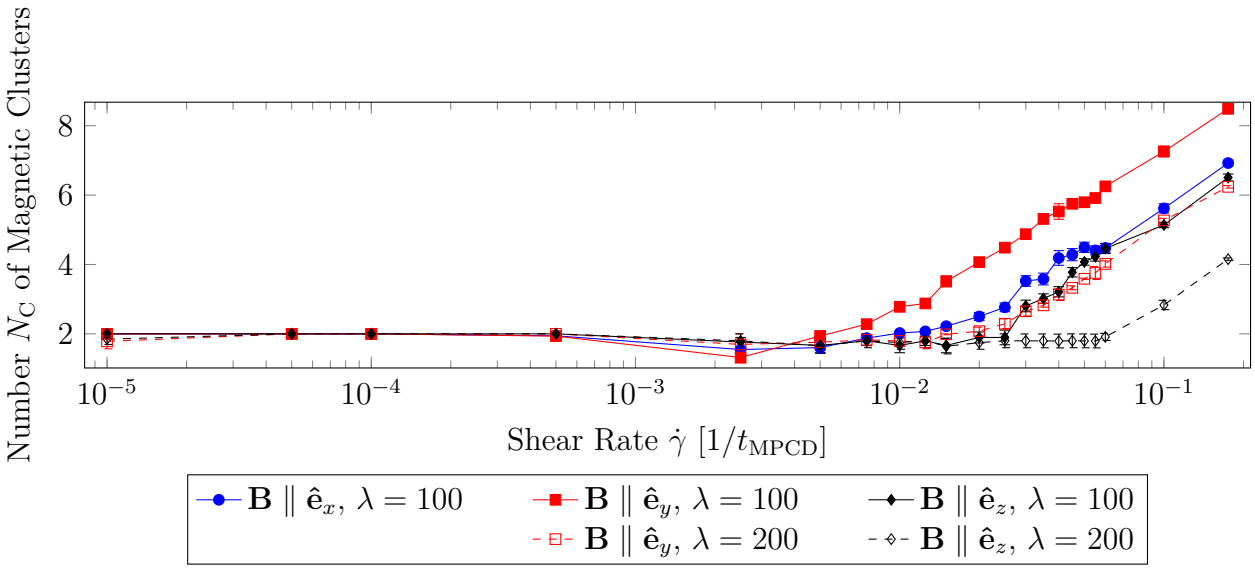

Figure 3.10: Mean number N_C of magnetic clusters as a function of the shear rate $\dot{\gamma}$ (reported in units of $1/t_{\mathrm{MPCD}}$, where t_{MPCD} is the unit of time in the MPCD simulation). Here and in the following plots, full symbols and solid lines correspond to $\lambda = 100$, while open symbols and dashed lines correspond to $\lambda = 200$. Circles (blue), squares (red), and diamonds (black) correspond to an external magnetic field $\mathbf{B}$ parallel to the x, y, and z axes, respectively.

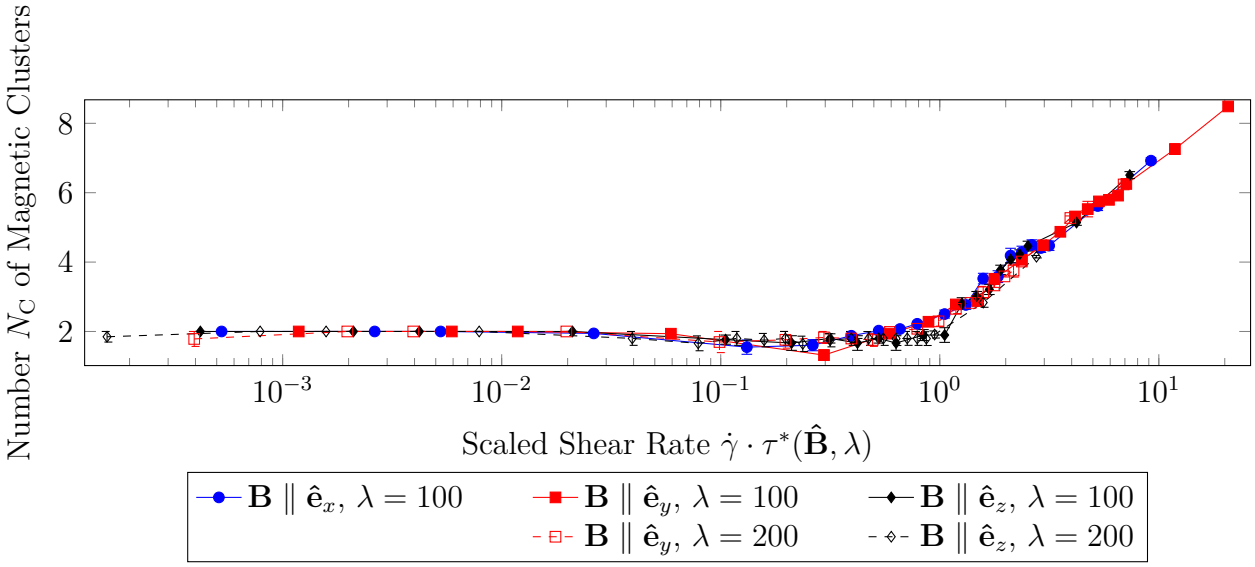

Figure 3.11: Mean number N_C of magnetic clusters as a function of the shear rate $\dot{\gamma}$ scaled by an empirical factor $\tau^*(\hat{\mathbf{B}}, \lambda)$ chosen such that the curves of Fig. 3.10 collapse.

$\hat{\mathbf{B}}$	λ	$\tau^*(\hat{\mathbf{B}}, \lambda)$
$\hat{\mathbf{e}}_x$	100	52.63
$\hat{\mathbf{e}}_y$	100	118.42
$\hat{\mathbf{e}}_z$	100	42.11
$\hat{\mathbf{e}}_y$	200	39.47
$\hat{\mathbf{e}}_z$	200	15.79

Table 3.1: Heuristically determined scaling times $\tau^*(\hat{\mathbf{B}}, \lambda)$ that collapse the measured mean cluster counts N_C onto a single master curve (cf. Fig. 3.11) — see text for details.

The product $\tau^*(\hat{\mathbf{B}}, \lambda) \cdot \dot{\gamma}$ is a measure for the (scaled) shear rate that has the advantage of being dimensionless. It may be reminiscent of the *Weissenberg number* Wi, which is defined as the product of the shear rate $\dot{\gamma}$ and a characteristic time τ. This concept exists for linear polymers,[35,36] ring polymers,[37] and star polymers,[38,39,40,41,42] among others.[43]

[35] C.-C. Huang, G. Sutmann, G. Gompper, and R. G. Winkler. "Tumbling of polymers in semidilute solution under shear flow". *Europhysics Letters* **93** (2011), 54004.

[36] K.-W. Hsiao, C. M. Schroeder, and C. E. Sing. "Ring Polymer Dynamics Are Governed by a Coupling between Architecture and Hydrodynamic Interactions". *Macromolecules* **49** (2016), 1961.

[37] Hsiao, Schroeder, and Sing, "Ring Polymer Dynamics Are Governed by a Coupling between Architecture and Hydrodynamic Interactions".

[38] G. S. Grest, K. Kremer, S. T. Milner, and T. A. Witten. "Relaxation of Self-Entangled Many-Arm Star Polymers". *Macromolecules* **22** (1989), 1904.

[39] D. Jaramillo-Cano, M. Formanek, C. N. Likos, and M. Camargo. "Star Block-Copolymers in Shear Flow". *The Journal of Physical Chemistry B* **122** (2018), 4149.

[40] M. Ripoll, R. G. Winkler, and G. Gompper. "Star Polymers in Shear Flow". *Physical Review Letters* **96** (2006), 188302.

[41] Ripoll, Winkler, and Gompper, "Hydrodynamic screening of star polymers in shear flow".

[42] J. Sablić, R. Delgado-Buscalioni, and M. Praprotnik. "Application of the Eckart frame to soft matter: rotation of star polymers under shear flow". *Soft Matter* **13** (2017), 6988. arXiv: `1707.09170 [cond-mat.soft]`.

[43] F. Taslimi, G. Gompper, and R. G. Winkler. "Scaffold Structures by Telechelic Rodlike Polymers: Nonequilibrium Structural and Rheological Properties under Shear Flow". *Macromolecules* **47** (2014), 6946.

While τ is often defined to be the *longest relaxation time* of the polymer in question, or a closely related polymer (such as an isolated arm of a star polymer),[44,45] the concrete definition of this τ varies in the literature. Depending on the authors, the reference times employed in defining the Weissenberg number for non-magnetic star polymers range from Zimm relaxation times of the (isolated) polymer arms,[46,47] rotational diffusion times of the stars,[48] to arm disentanglement times,[49] with other candidate relaxation times described in the literature.[50]

Since it is unclear which, if any, of the many relaxation times would be appropriate to define a Weissenberg number in the case of the magnetically functionalized stars studied here, the author of this thesis refrains from denoting the empirically scaled shear rates $\tau^*(\hat{\mathbf{B}}, \lambda) \cdot \dot{\gamma}$ as a (or *the*) Weissenberg number. In particular, the introduction of the magnetic interaction at the free ends of the arms causes a qualitative change in the behavior of the arms (i.e. regarding end-to-end vector autocorrelation of the arms, as is sometimes studied for linear polymers,[51] or regarding the arm disentanglement times[52]). Furthermore, particularly for strong magnetic interactions λ, the characteristic times for magnetic clusters to form and break up can be prohibitively long for computer simulations, making these time scales poor candidates for a reference time if one wants to establish comparability of MFSPs (regarding e.g. the quantities discussed in the following subsection) with non-magnetic stars.

[44] Hsiao, Schroeder, and Sing, "Ring Polymer Dynamics Are Governed by a Coupling between Architecture and Hydrodynamic Interactions".
[45] Jaramillo-Cano, Formanek, Likos, and Camargo, "Star Block-Copolymers in Shear Flow".
[46] Ripoll, Winkler, and Gompper, "Star Polymers in Shear Flow".
[47] Jaramillo-Cano, Formanek, Likos, and Camargo, "Star Block-Copolymers in Shear Flow".
[48] Sablić, Delgado-Buscalioni, and Praprotnik, "Application of the Eckart frame to soft matter: rotation of star polymers under shear flow".
[49] Sablić, Delgado-Buscalioni, and Praprotnik, "Application of the Eckart frame to soft matter: rotation of star polymers under shear flow".
[50] Grest, Kremer, Milner, and Witten, "Relaxation of Self-Entangled Many-Arm Star Polymers".
[51] Huang, Sutmann, Gompper, and Winkler, "Tumbling of polymers in semidilute solution under shear flow".
[52] Sablić, Delgado-Buscalioni, and Praprotnik, "Application of the Eckart frame to soft matter: rotation of star polymers under shear flow".

3.5.2 N_C-Controlled Quantities: Size and Shape Descriptors

To quantitatively analyze the size and shape of the magnetically functionalized star polymers under shear, one can measure the radius of gyration R_g (Fig. 3.12), acylindricity c (Fig. 3.13), asphericity b (Fig. 3.21), and relative shape anisotropy κ^2 (Fig. 3.22), elaborated on below. These four quantities can be computed from the eigenvalues $\Lambda_1^2 \leq \Lambda_2^2 \leq \Lambda_3^2$ of the so-called gyration tensor $S_{\mu\nu}$ (with $\mu, \nu \in \{x, y, z\}$) as follows:[53]

$$S_{\mu\nu} := \frac{1}{N} \sum_{i=1}^{N} r_\mu^{(i,\mathrm{S})} r_\nu^{(i,\mathrm{S})}, \tag{3.8}$$

$$c := \Lambda_2^2 - \Lambda_1^2, \tag{3.9}$$

$$b := \Lambda_3^2 - \frac{1}{2}\left(\Lambda_1^2 + \Lambda_2^2\right), \tag{3.10}$$

$$R_g := \sqrt{\Lambda_1^2 + \Lambda_2^2 + \Lambda_3^2}, \tag{3.11}$$

$$\kappa^2 := \left(b^2 + \frac{3}{4}c^2\right) / R_g^4. \tag{3.12}$$

Here, $N = 1 + f\,(n_\mathrm{A} + 1)$ is the total number of particles per star polymer, and $r_\mu^{(i,\mathrm{S})}$ is the μ-component of the Cartesian position vector of particle number i, with the coordinate system chosen such that $\sum_{i=1}^{N} r_\mu^{(i,\mathrm{S})} = 0$ for all μ, which coincides with the center of mass frame since all monomers have the same mass.

[53] D. N. Theodorou and U. W. Suter. "Shape of Unperturbed Linear Polymers: Polypropylene". *Macromolecules* **18** (1985), 1206.

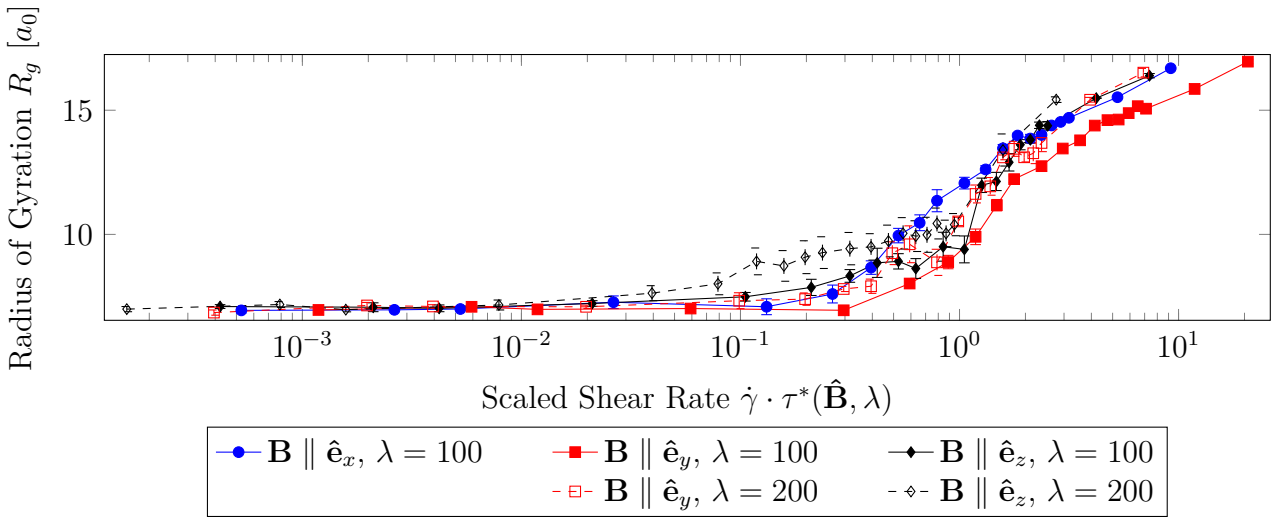

Figure 3.12: Radius of gyration R_g, in multiples of the unit length a_0, as a function of the scaled shear rate $\dot{\gamma} \cdot \tau^*(\hat{\mathbf{B}}, \lambda)$. (See text for details.)

That the eigenvalues $\Lambda_1^2 \leq \Lambda_2^2 \leq \Lambda_3^2$ are real and non-negative can bee seen by the fact that $S_{\mu\nu}$ is evidently real and symmetric and hence Hermitian[54] and normal,[55] which proves that the eigenvalues are real[56] and that the eigenvectors form an orthogonal basis,[57] so that the gyration tensor becomes diagonal in that basis.[58] In this Cartesian coordinate system, the definition Eq. (3.8) of the gyration tensor applies equally (since the center-of-mass-frame property $\sum_{i=1}^{N} r_\mu^{(i,\mathrm{S})} = 0$ is conserved by the coordinate transformation $\mathbf{r}^{(i,\mathrm{S})} \mapsto U\mathbf{r}^{(i,\mathrm{S})}$, with U being the unitary transformation matrix facilitating the change of coordinate system[59]); then, in this coordinate system, the off-diagonal elements of the transformed $S_{\mu\nu}$ are zero, and the diagonal elements are given by sums of squares of real values, and hence are non-negative. Since these diagonal elements are the eigenvalues of the transformed gyration tensor, which are invariant under unitary coordinate transformations, necessarily the original gyration tensor's eigenvalues are non-negative too.

Radius of Gyration R_g

The radius of gyration R_g is an often-used[60] and versatile[61] measure of the size of an arbitrary object that can be accessed in experiments, e.g. via small-angle scattering.[62] From the definition Eq. (3.11), one can see that its square is equal to the trace of the gyration tensor $S_{\mu\nu}$, cf. Eq. (3.8). Therefore,

$$R_g = \sqrt{\frac{1}{N}\sum_{i=1}^{N} \left|\mathbf{r}^{(i,\mathrm{S})}\right|^2} \tag{3.13}$$

is an equivalent definition, from which it becomes evident that the radius of gyration is the root-mean-square of the distance of the MFSP's monomers from the center of mass.

For low shear rates $\dot{\gamma}$, the radius of gyration $R_g \approx 7a_0$ is close to the equilibrium value of Blaak and Likos[63] (cf. Fig. 3.8), despite the slight differences in the model and simulation methodology discussed in Section 3.2.2. With increasing shear rate, the radius of gyration experiences a mostly steady increase, except when passing the critical shear rate $\dot{\gamma}^*$, i.e. $\dot{\gamma} \cdot \tau^*(\hat{\mathbf{B}}, \lambda) \approx 1$, where magnetic clusters start breaking up and a sudden increase in R_g can be observed, particularly pronounced for $\hat{\mathbf{B}} = \hat{\mathbf{e}}_z$. This feature will emerge in many of the other quantities studied below.

[54] R. A. Beezer. *A First Course in Linear Algebra*. 3.50. Congruent Press, 2015. Definition HM, Pages 188f.
[55] Beezer, *A First Course in Linear Algebra*, Definition NRML, Page 575.
[56] Beezer, *A First Course in Linear Algebra*, Theorem HMRE, Page 400.
[57] Beezer, *A First Course in Linear Algebra*, Theorem OBNM, Page 578 (for a weaker version, see Theorem HMOE, Page 401).
[58] Beezer, *A First Course in Linear Algebra*, Theorem OD, Page 575.
[59] Beezer, *A First Course in Linear Algebra*, Text under Theorem OBNM, Page 579.
[60] M. Fixman. "Radius of Gyration of Polymer Chains". *The Journal of Chemical Physics* **36** (1962), 306.
[61] Rubinstein and Colby, *Polymer Physics*, Section 2.4.
[62] Rubinstein and Colby, *Polymer Physics*, Section 2.8.3.
[63] Blaak and Likos, "Self-assembly of magnetically functionalized star-polymer nano-colloids".

Shape Descriptors

At the outset, it should be noted that, despite what might be suggested by their names, the asphericity b and acylindricity c (and to a lesser extent, the relative shape anisotropy κ^2) do not exactly measure deviations from spherical or cylindrical configurations. Although these quantities take on values of 0 in the case of spherically or cylindrically symmetric arrangements of particles, respectively, the inverse conclusion is not strictly true, as shapes of certain other symmetries (e.g. tetrahedral symmetry) satisfy $b = c = \kappa^2 = 0$ as well.[64] Nevertheless, b, c and κ^2 are useful as they allow for quantitative comparisons of the shapes of star polymers.

The acylindricity c, Eq. (3.9), measures the difference in the smaller two eigenvalues of the gyration tensor. Were the MFSP spherically or cylindrically symmetric, one would find $c = 0$. Looking at the data visualized in Fig. 3.13, one finds that for $\hat{\mathbf{B}} = \hat{\mathbf{e}}_z$, there is a marked deviation from the otherwise relatively uniform $c \lesssim 5a_0$. Inspection of the behavior of the two smaller eigenvalues of S, Λ_1^2 (Fig. 3.14) and Λ_2^2 (Fig. 3.15), reveals that the former decreases with growing $\dot{\gamma}$ in qualitatively the same way for all $\hat{\mathbf{B}}$ investigated, but Λ_2^2 remains approximately constant for $\hat{\mathbf{B}} = \hat{\mathbf{e}}_z$, until it abruptly decreases at the critical shear rate.

To arrive at an interpretation, it is helpful to first understand which eigenvalue corresponds to which spatial axis in the system. Fig. 3.17 plots the orientation angle χ_G, defined as the angle between the shear flow direction (i.e. the x axis) and the major axis of the star polymer, i.e. the eigenvector corresponding to Λ_3^2, the largest eigenvalue of the gyration tensor. For low shear rates, the orientation angle has a relatively large mean value and considerable standard deviation (as indicated by the error bars), which suggests that there is no strong preference for alignment of the major axis with the shear flow direction; indeed, the star polymer as a whole is rather spherically symmetric, as the asphericity (Fig. 3.21) and relative shape anisotropy data (Fig. 3.22) reveal, despite the preference of the magnetic monomers to align along the external magnetic field (cf. the representative snapshot Fig. 3.4 in equilibrium). At higher shear rates, however, a strong orientation towards the shear flow direction sets in, which is due to the fact that the shear flow elongates the star along the x direction, and compresses it along the other directions, which in turn is evidenced by the increase in the largest eigenvector (Fig. 3.16), asphericity (Fig. 3.21), and relative shape anisotropy (Fig. 3.22), with according reductions in the smaller gyration tensor eigenvalues.

[64] Theodorou and Suter, "Shape of Unperturbed Linear Polymers: Polypropylene".

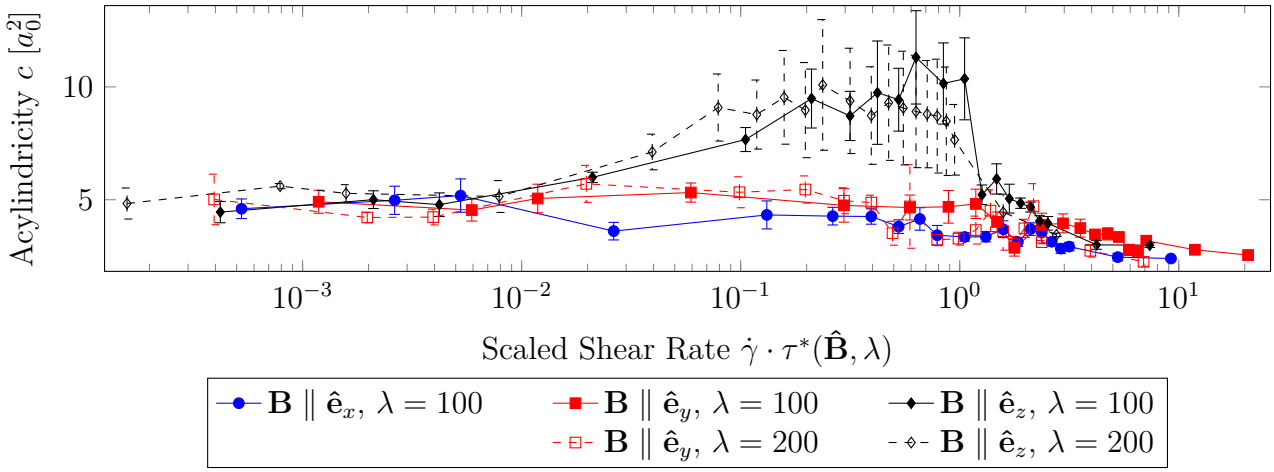

Figure 3.13: Acylindricity c as a function of the scaled shear rate $\dot{\gamma} \cdot \tau^*(\hat{\mathbf{B}}, \lambda)$. (See text for details.)

Turning back to the shoulder in the acylindricity graph (Fig. 3.13) and the abrupt decline in the middle eigenvalue Λ_2^2 (Fig. 3.15) for $\hat{\mathbf{B}} = \hat{\mathbf{e}}_z$, one can now identify three different regimes: for low $\dot{\gamma}$, the MFSP is roughly spherically symmetric overall, despite the linear arrangement of the magnetic monomers. For scaled shear rates in the region $10^{-1} \lesssim \dot{\gamma} \cdot \tau^*(\hat{\mathbf{B}}, \lambda) \lesssim 1$, the shear flow elongates and orients the star polymer along the flow direction, but is unable to break the magnetic columns, which causes the linear extent of the MSFP to be larger along the z direction (i.e. the axis of the magnetic field) than along the gradient direction y, and hence effects an increase in the acylindricity. Only after the critical shear rate is reached ($\dot{\gamma} \cdot \tau^*(\hat{\mathbf{B}}, \lambda) \approx 1$) do the magnetic columns break up, and the preference for z over y is lost, leading to similar values for the smallest and middle eigenvalue of the gyration tensor. This interpretation is also supported by analysis of the xx, yy, and zz components of the gyration tensor in the laboratory coordinate system (Figs. 3.18 to 3.20).

The results for the asphericity (Fig. 3.21) and relative shape anisotropy (Fig. 3.22) corroborate this picture of a comparatively spherical MFSP for low shear rates, and strongly elongated MFSPs for high shear rates, with a particularly abrupt transition near $\dot{\gamma} \cdot \tau^*(\hat{\mathbf{B}}, \lambda) \approx 1$ especially for $\hat{\mathbf{B}} = \hat{\mathbf{e}}_z$.

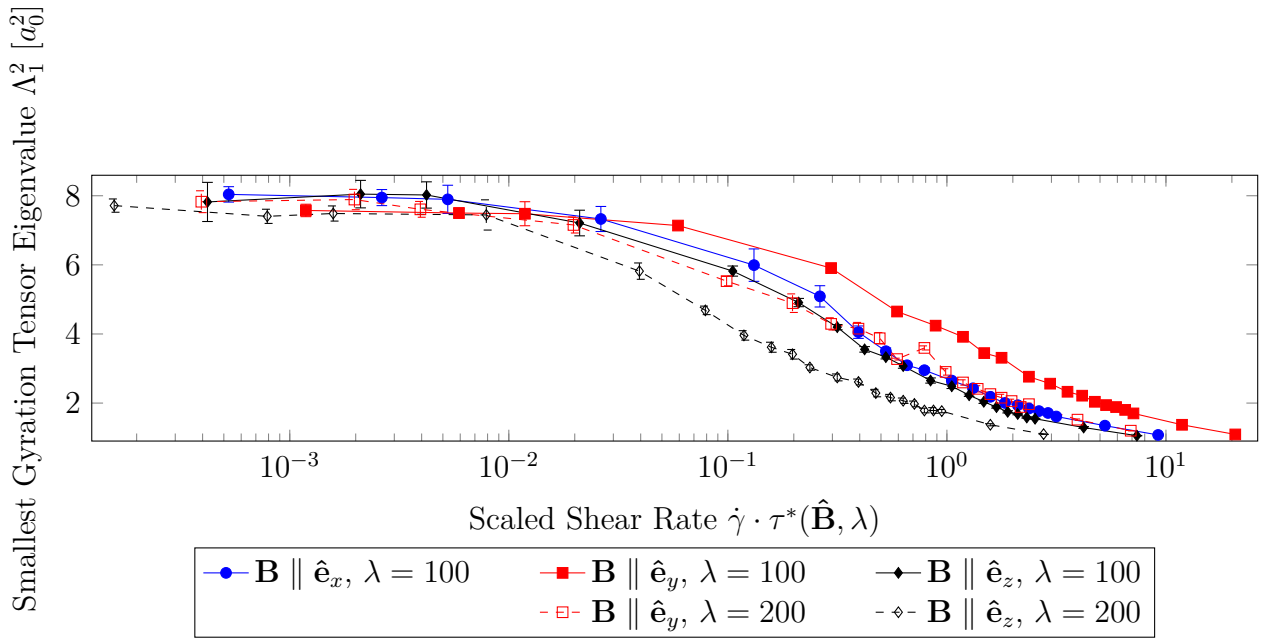

Figure 3.14: The smallest eigenvalue Λ_1^2 of the gyration tensor, measured in squared unit lengths a_0^2, as a function of the scaled shear rate $\dot{\gamma} \cdot \tau^*(\hat{\mathbf{B}}, \lambda)$. (See text for details.)

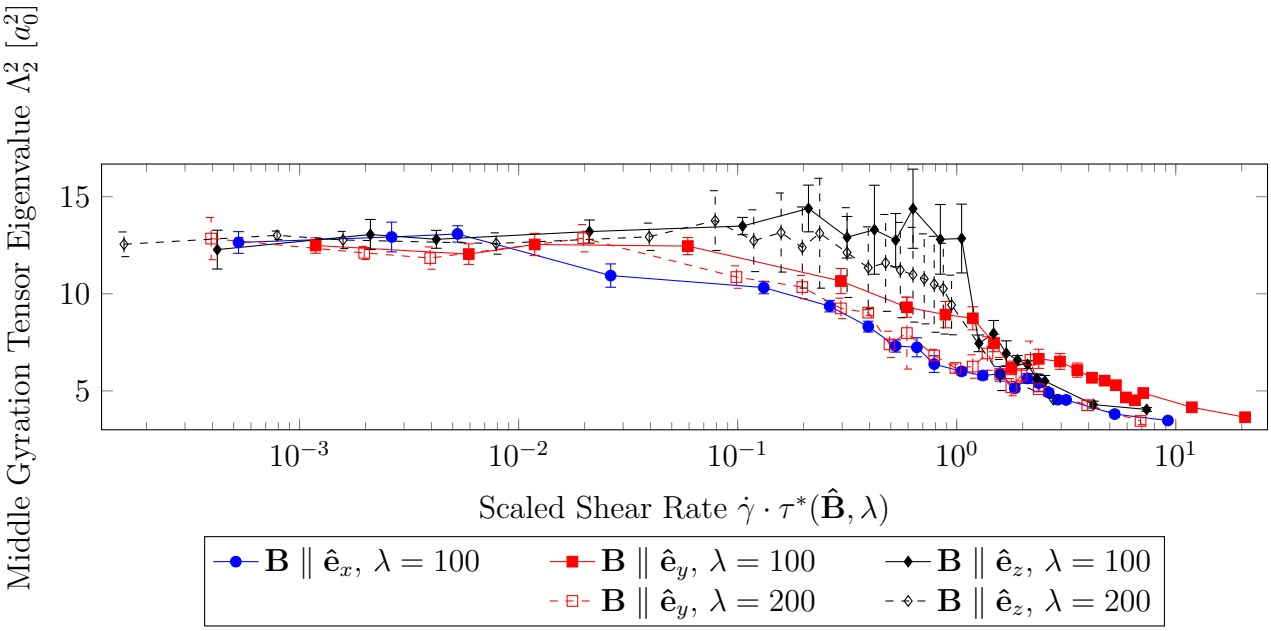

Figure 3.15: The middle eigenvalue Λ_2^2 of the gyration tensor, measured in squared unit lengths a_0^2, as a function of the scaled shear rate $\dot{\gamma} \cdot \tau^*(\hat{\mathbf{B}}, \lambda)$. (See text for details.)

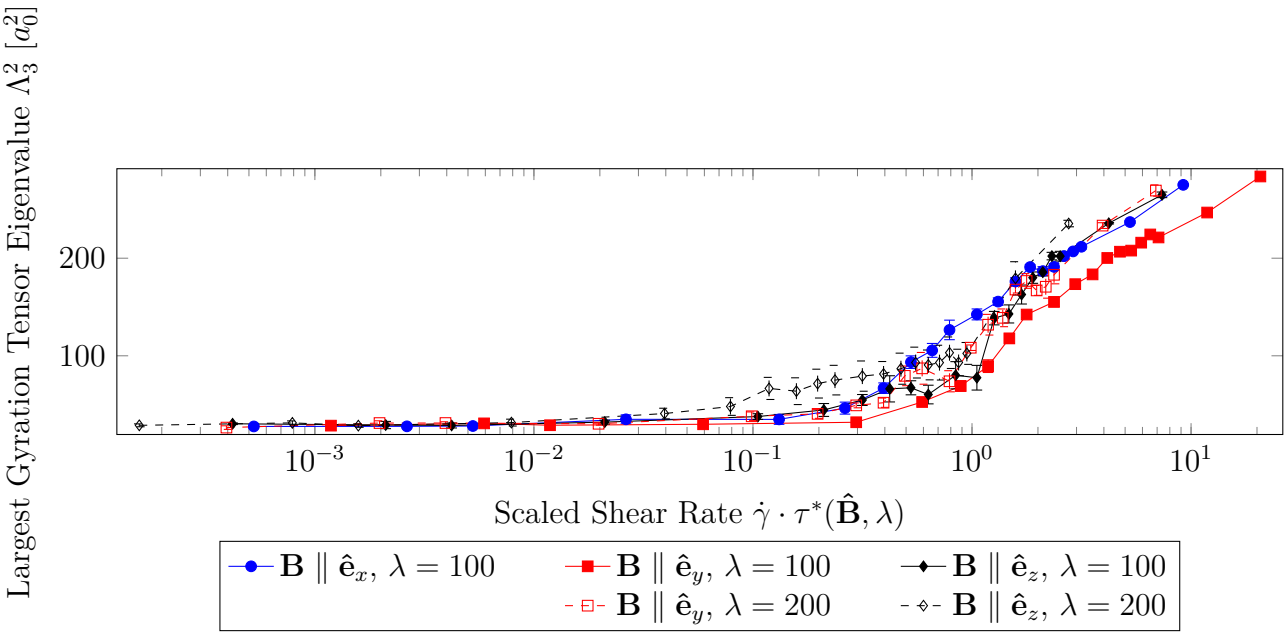

Figure 3.16: The largest eigenvalue Λ_3^2 of the gyration tensor, measured in squared unit lengths a_0^2, as a function of the scaled shear rate $\dot{\gamma} \cdot \tau^*(\hat{\mathbf{B}}, \lambda)$. (See text for details.)

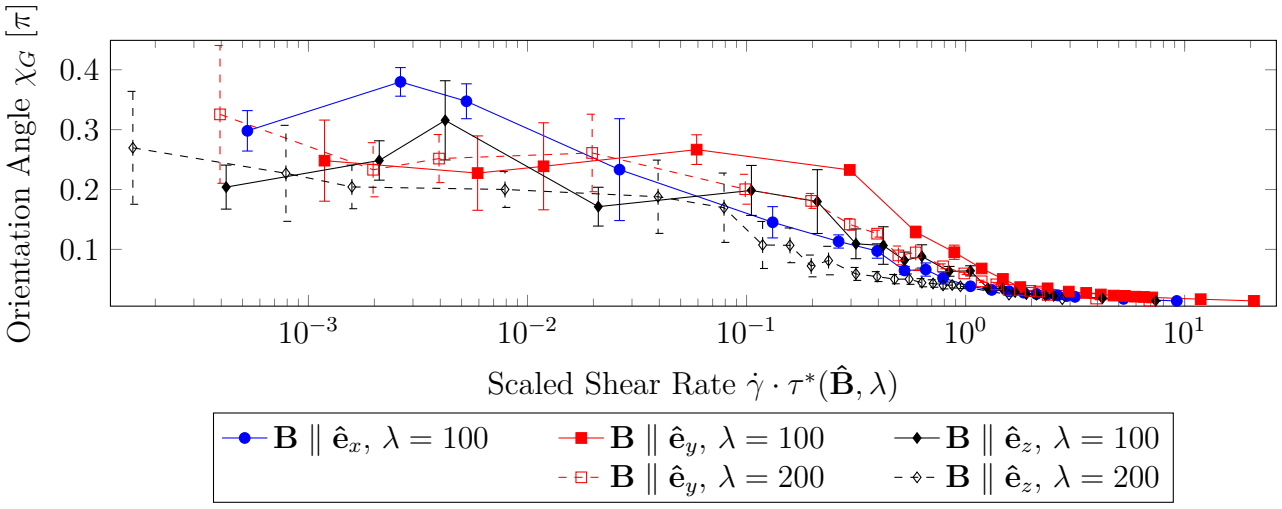

Figure 3.17: Orientation angle χ_G, measured in radians and shown in multiples of π, as a function of the scaled shear rate $\dot{\gamma} \cdot \tau^*(\hat{\mathbf{B}}, \lambda)$. The orientation angle is defined to be the angle between the direction of shear flow (the x axis in this work), and the gyration tensor's eigenvector corresponding to the largest eigenvalue, i.e. the direction along which the star polymer is most extended. (See text for details.)

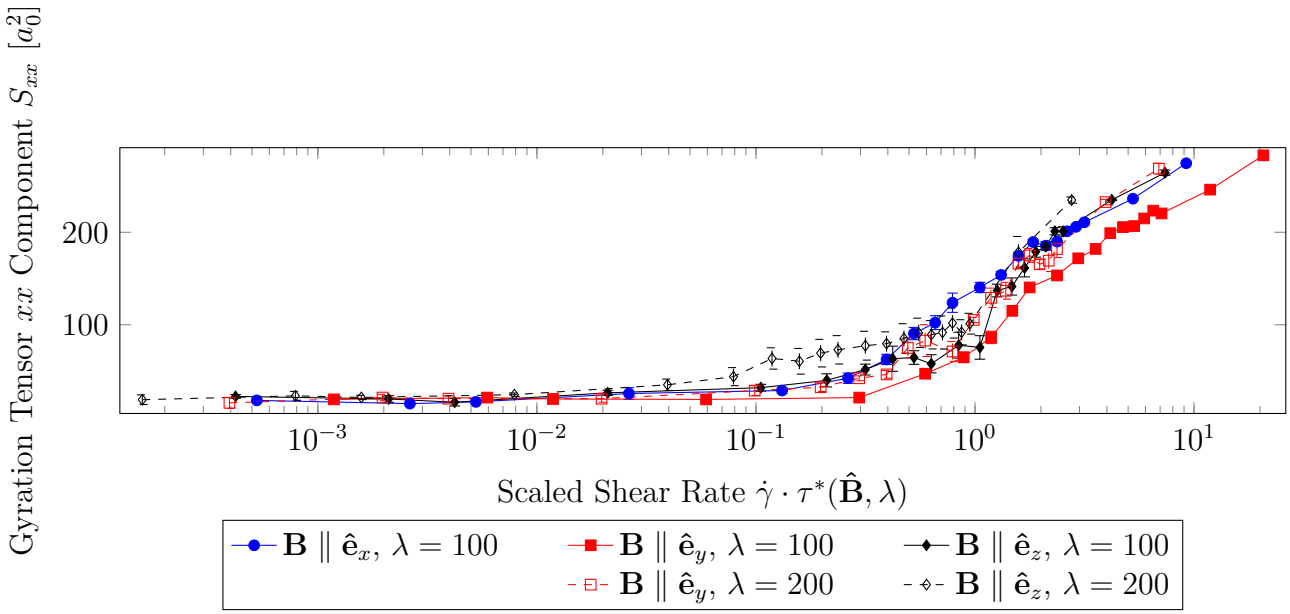

Figure 3.18: The xx component of the gyration tensor in the laboratory frame (see text), measured in squared unit lengths a_0^2, as a function of the scaled shear rate $\dot{\gamma} \cdot \tau^*(\hat{\mathbf{B}}, \lambda)$.

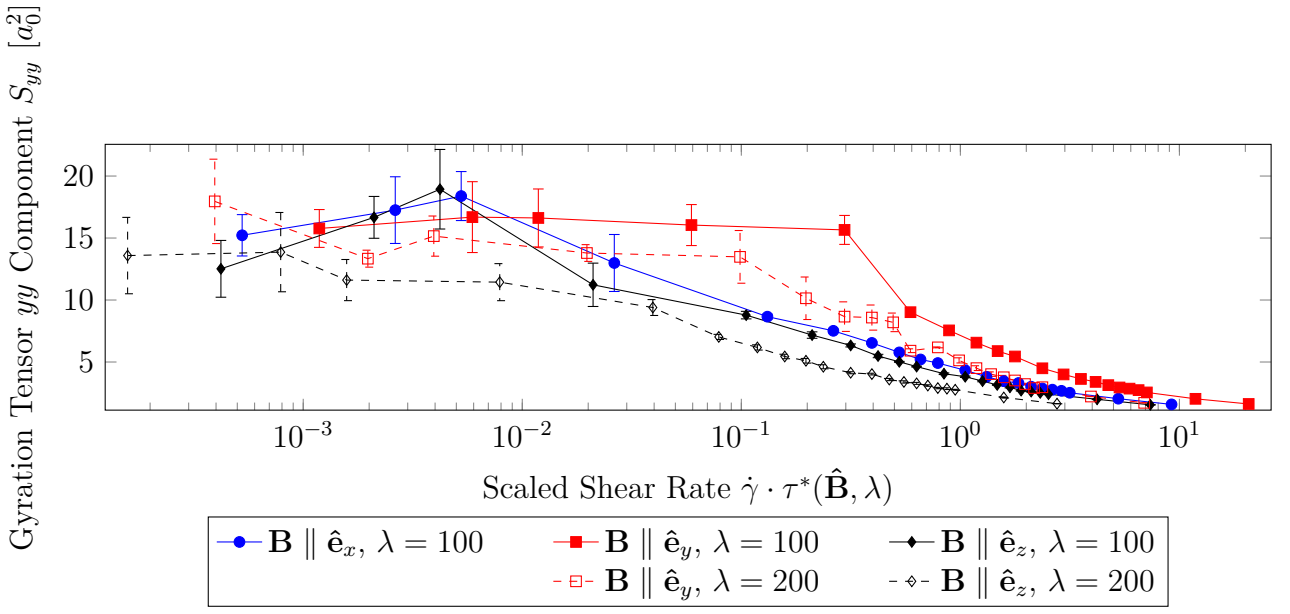

Figure 3.19: The yy component of the gyration tensor in the laboratory frame (see text), measured in squared unit lengths a_0^2, as a function of the scaled shear rate $\dot{\gamma} \cdot \tau^*(\hat{\mathbf{B}}, \lambda)$.

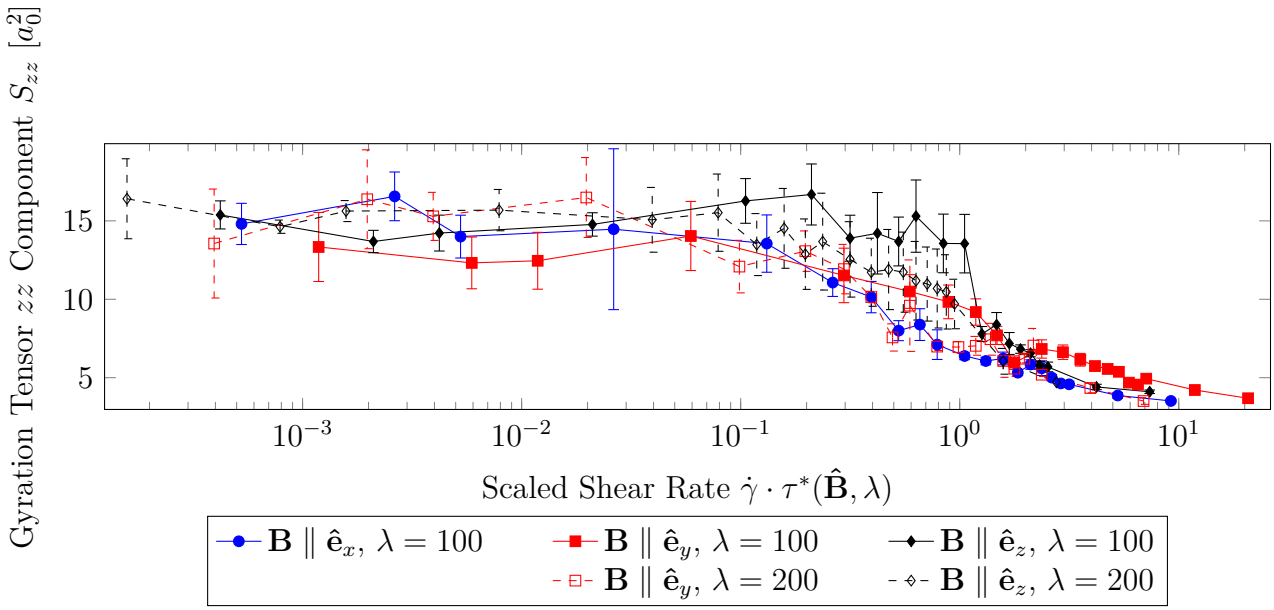

Figure 3.20: The zz component of the gyration tensor in the laboratory frame (see text), measured in squared unit lengths a_0^2, as a function of the scaled shear rate $\dot{\gamma} \cdot \tau^*(\hat{\mathbf{B}}, \lambda)$.

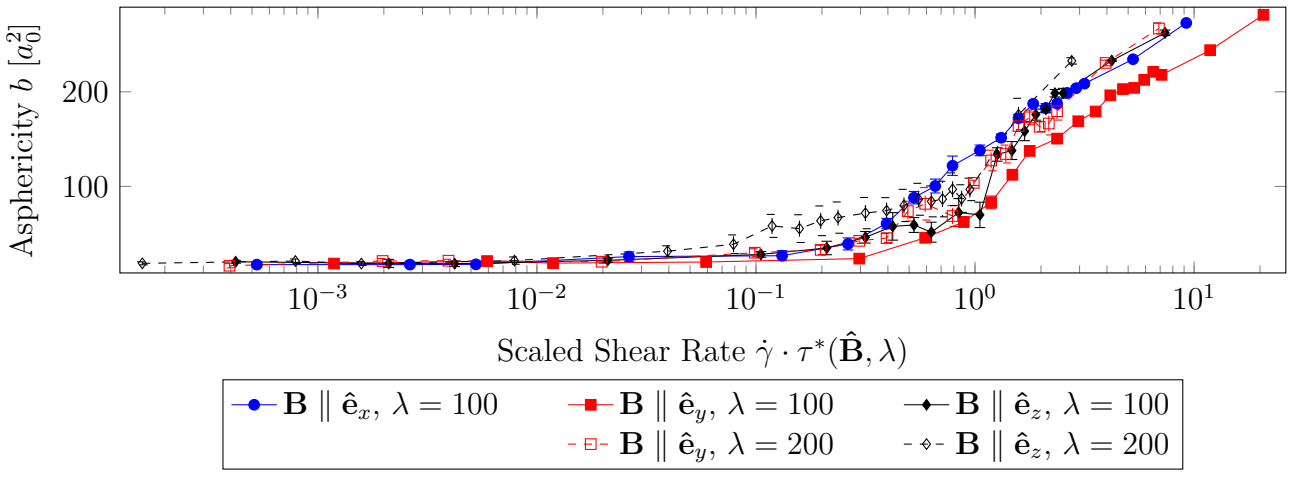

Figure 3.21: Asphericity b as a function of the scaled shear rate $\dot{\gamma} \cdot \tau^*(\hat{\mathbf{B}}, \lambda)$. (See text for details.)

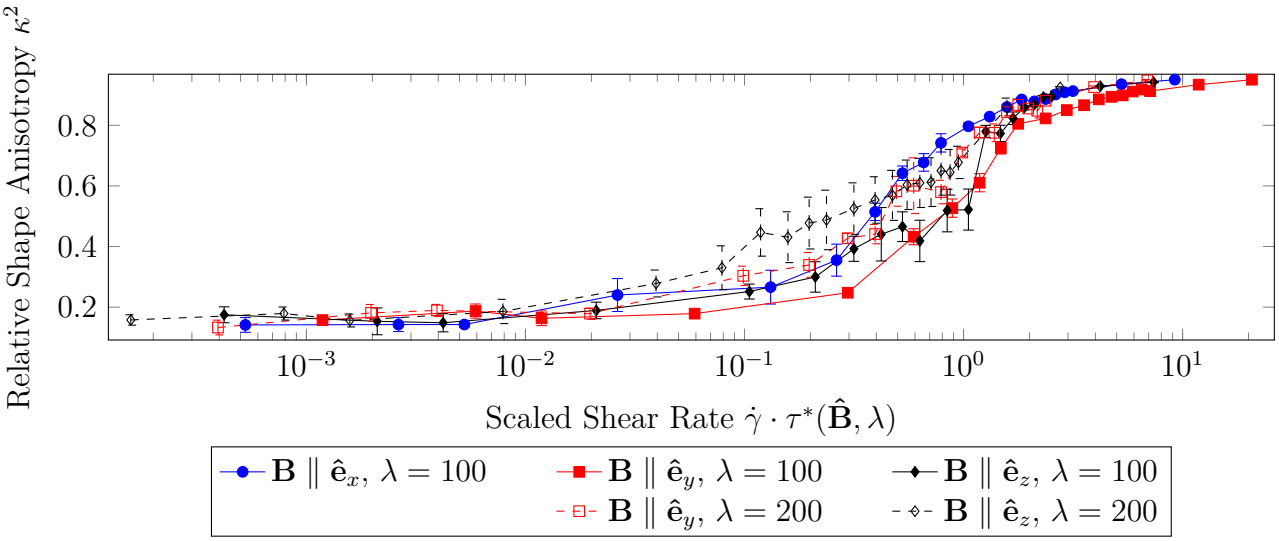

Figure 3.22: Relative shape anisotropy κ^2 as a function of the scaled shear rate $\dot{\gamma} \cdot \tau^*(\hat{\mathbf{B}}, \lambda)$. (See text for details.)

3.5.3 Universal Properties: Orientational Resistance

As Ripoll et al.[65] describe, one can find a relationship

$$\tan(2\chi_G) = \frac{2S_{xy}}{S_{xx} - S_{yy}} \tag{3.14}$$

between the orientation angle χ_G, discussed in the previous subsection, and particular components of the laboratory-frame gyration tensor $S_{\mu\nu}$. Ripoll et al.[66] report that a quantity called *orientational resistance*, defined as

$$m_G = \mathrm{Wi} \tan(2\chi_G), \tag{3.15}$$

is approximately constant (i.e. independent of the shear rate) for low Weissenberg numbers Wi in non-magnetic star polymers, as is the case for linear polymers and rod-like colloids, and beyond a certain Wi grows as

$$m_G \propto \mathrm{Wi}^{\mu} \tag{3.16}$$

with an exponent $\mu = 0.65 \pm 0.05$ (as opposed to $\mu = 0.54 \pm 0.03$ for self-avoiding linear polymers).

[65] Ripoll, Winkler, and Gompper, "Star Polymers in Shear Flow".
[66] Ripoll, Winkler, and Gompper, "Star Polymers in Shear Flow".

$\hat{\mathbf{B}}$	λ	$\dot{\gamma}_{\text{optimal}}$	C	μ	σ_C	σ_μ
$\hat{\mathbf{e}}_x$	100	0.00	$4.47 \cdot 10^{-2}$	$6.10 \cdot 10^{-1}$	$7.85 \cdot 10^{-4}$	$6.91 \cdot 10^{-3}$
$\hat{\mathbf{e}}_y$	100	0.00	$4.59 \cdot 10^{-2}$	$6.36 \cdot 10^{-1}$	$5.99 \cdot 10^{-4}$	$5.07 \cdot 10^{-3}$
$\hat{\mathbf{e}}_z$	100	0.00	$4.14 \cdot 10^{-2}$	$5.57 \cdot 10^{-1}$	$1.18 \cdot 10^{-3}$	$1.20 \cdot 10^{-2}$
$\hat{\mathbf{e}}_y$	200	$1 \cdot 10^{-5}$	$3.40 \cdot 10^{-2}$	$4.21 \cdot 10^{-1}$	$1.15 \cdot 10^{-3}$	$1.14 \cdot 10^{-2}$
$\hat{\mathbf{e}}_z$	200	0.00	$3.84 \cdot 10^{-2}$	$4.06 \cdot 10^{-1}$	$2.05 \cdot 10^{-3}$	$2.53 \cdot 10^{-2}$

Table 3.2: Fits of $m_G = C\dot{\gamma}^\mu$ with fit parameters C and μ (in units of τ, as defined in the text) and respective uncertainties σ_C and σ_μ, only taking data points into account if $\dot{\gamma} \geq \dot{\gamma}_{\text{optimal}}$, where $\dot{\gamma}_{\text{optimal}}$ is chosen such that it minimizes σ_μ. See Fig. 3.23.

Since this thesis refrains from declaring a particular Weissenberg number (cf. Section 3.5.1), a *reduced orientational resistance* m_G/τ is defined and studied, with τ being the factor in the relation $\text{Wi} = \tau\dot{\gamma}$. The qualitative behavior can nevertheless be directly compared with the results of Ripoll et al.:[67] as Fig. 3.23 demonstrates, the behavior of magnetically functionalized star polymers is similar in its functional form to that of non-magnetic stars and other polymeric systems. In particular, the data are compatible with a constant (reduced) orientational resistance for low shear rates (or Weissenberg numbers), and are well approximated by $m_G = C\dot{\gamma}^\mu$ for higher $\dot{\gamma}$. Performing a least-squares fit on the data (including uncertainties in the measurements of m_G) produces the fit parameters C and μ reported in Table 3.2; in particular, the exponents are found to lie in the range 0.4 to approximately 0.6.

The exponents μ found here are compatible with the one reported in Ripoll et al.[68] for the cases where magnetic clusters are particularly easy to break up and the MFSPs thus most resemble a non-magnetic star. Moreover, it is noteworthy that also for more robust magnetic clusters, the scaling behavior $m_G \propto \dot{\gamma}^\mu$ seems to hold. In this sense, the introduction of magnetic interactions via the end monomers' dipole moments does not remove star polymers from the class of systems characterized by the power-law dependence of the orientational resistance on the shear strength. (Note that the reference time τ has not been adjusted for changes in $\hat{\mathbf{B}}$ or λ.)

[67] Ripoll, Winkler, and Gompper, "Star Polymers in Shear Flow".
[68] Ripoll, Winkler, and Gompper, "Star Polymers in Shear Flow".

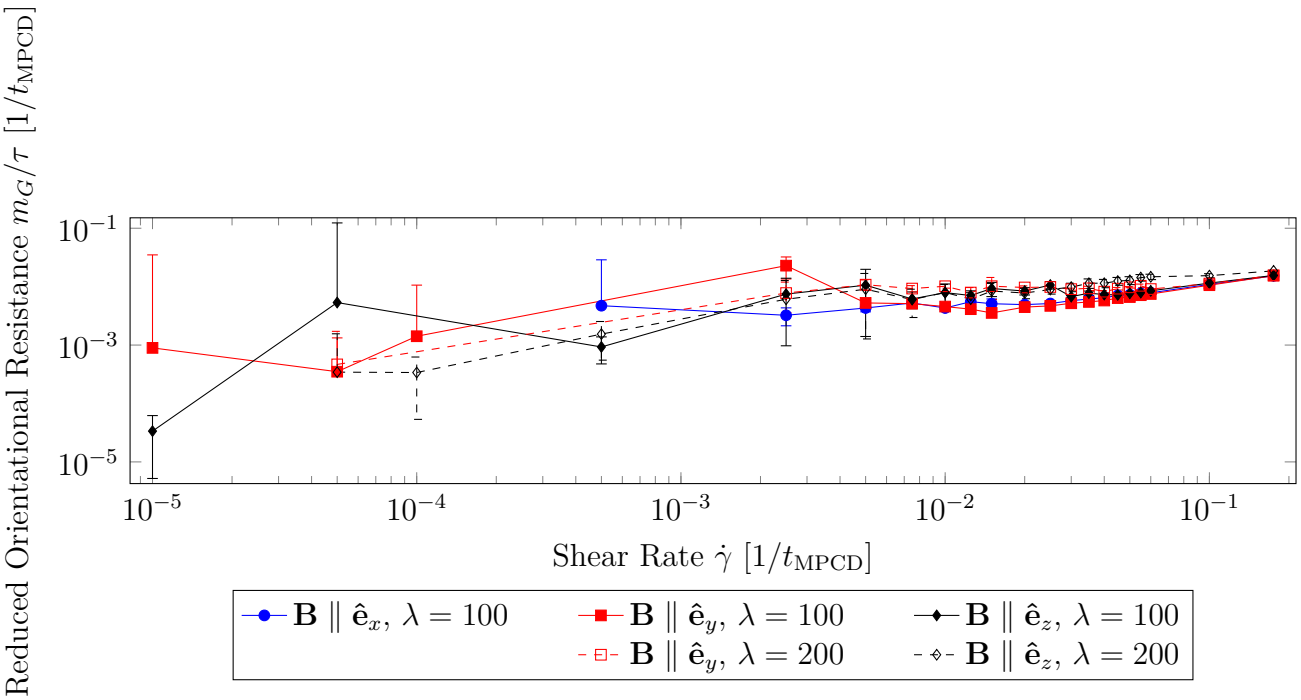

Figure 3.23: Reduced orientational resistance, m_G/τ, as a function of the proper shear rate $\dot{\gamma}$, both in units of t_{MPCD}^{-1}. The data are compatible with a plateau for low $\dot{\gamma}$ (note the large standard deviations, as indicated by the error bars) and an exponential scaling law $m_G/\tau = C\dot{\gamma}^{\mu}$ for high $\dot{\gamma}$; see Table 3.2 and the main text for details.

3.5.4 $\hat{\mathbf{B}}$-Sensitivity Beyond $N_{\mathbf{C}}$: Whole-Body Rotations

In order to analyze the rotational dynamics of the star polymer in the center-of-mass frame, one can investigate the angular velocity vector

$$\boldsymbol{\omega} = I^{-1} \cdot \mathbf{L}, \tag{3.17}$$

where

$$\mathbf{L} = \sum_{i=1}^{N} \mathbf{r}_i \times \mathbf{p}_i \tag{3.18}$$

is the total angular momentum vector of all of the MFSP's monomers, and the moment of inertia tensor I is symmetric and has diagonal components

$$I_{xx} = \sum_{i=1}^{N} m_i \left(y_i^2 + z_i^2\right) , \tag{3.19a}$$

$$I_{yy} = \sum_{i=1}^{N} m_i \left(x_i^2 + z_i^2\right) , \tag{3.19b}$$

$$I_{zz} = \sum_{i=1}^{N} m_i \left(x_i^2 + y_i^2\right) , \tag{3.19c}$$

and off-diagonal components

$$I_{xy} = I_{yx} = -\sum_{i=1}^{N} m_i x_i y_i \, , \tag{3.20a}$$

$$I_{xz} = I_{zx} = -\sum_{i=1}^{N} m_i x_i z_i \, , \tag{3.20b}$$

$$I_{yz} = I_{zy} = -\sum_{i=1}^{N} m_i y_i z_i \, . \tag{3.20c}$$

In the above, m_i, $\mathbf{p}_i$ and $\mathbf{r}_i = (x_i, y_i, z_i)^{\mathrm{T}}$ are the mass (uniform for all monomers in the studied MFSP model), momentum vector, and position vector of the i-th monomer, respectively.

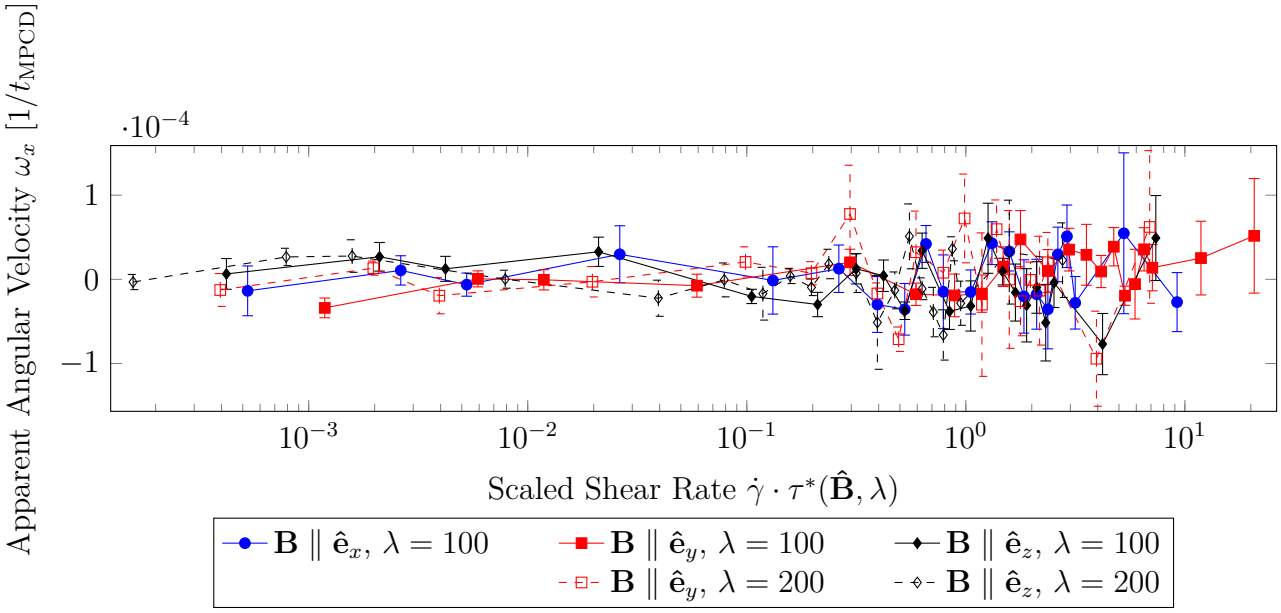

Figure 3.24: x-component ω_x of the apparent angular velocity $\boldsymbol{\omega}$, as defined in Eq. (3.17), in units of t_{MPCD}^{-1}. (See text for details.)

Although this method produces qualitatively usable data on the rotational dynamics of the star, particularly if I is calculated anew for every conformation of the MFSP, it suffers from an inability to distinguish true whole-body rotation from inconsequential translation or vibration of individual monomers – a deficiency that does not rear its head in the analysis of rigid bodies.[69] While the data for what will now be called *apparent* angular velocity (see Eq. (3.17)) are shown for reference in Figs. 3.24 to 3.26, the discussion will be formulated in terms of the *Eckart frame* formalism,[70,71] which minimizes spurious contributions, caused by vibrational motion, to the proper angular velocity.

Following Louck and Galbraith[72] (and always working in a center-of-mass frame), we start by arbitrarily choosing a particular configuration of the MFSP as the reference configuration. Let $\boldsymbol{\mathcal{R}}^{(i)}$ be the position vector of the i-th monomer in the reference configuration, with components $\mathcal{R}_x^{(i)}$, $\mathcal{R}_y^{(i)}$, and $\mathcal{R}_z^{(i)}$. Then, for each given instantaneous configuration, individually define the

[69] Sablić, Delgado-Buscalioni, and Praprotnik, "Application of the Eckart frame to soft matter: rotation of star polymers under shear flow".
[70] C. Eckart. "Some Studies Concerning Rotating Axes and Polyatomic Molecules". *Physical Review* **47** (1935), 552.
[71] J. D. Louck and H. W. Galbraith. "Eckart vectors, Eckart frames, and polyatomic molecules". *Reviews of Modern Physics* **48** (1976), 69.
[72] Louck and Galbraith, "Eckart vectors, Eckart frames, and polyatomic molecules", Section III.A.

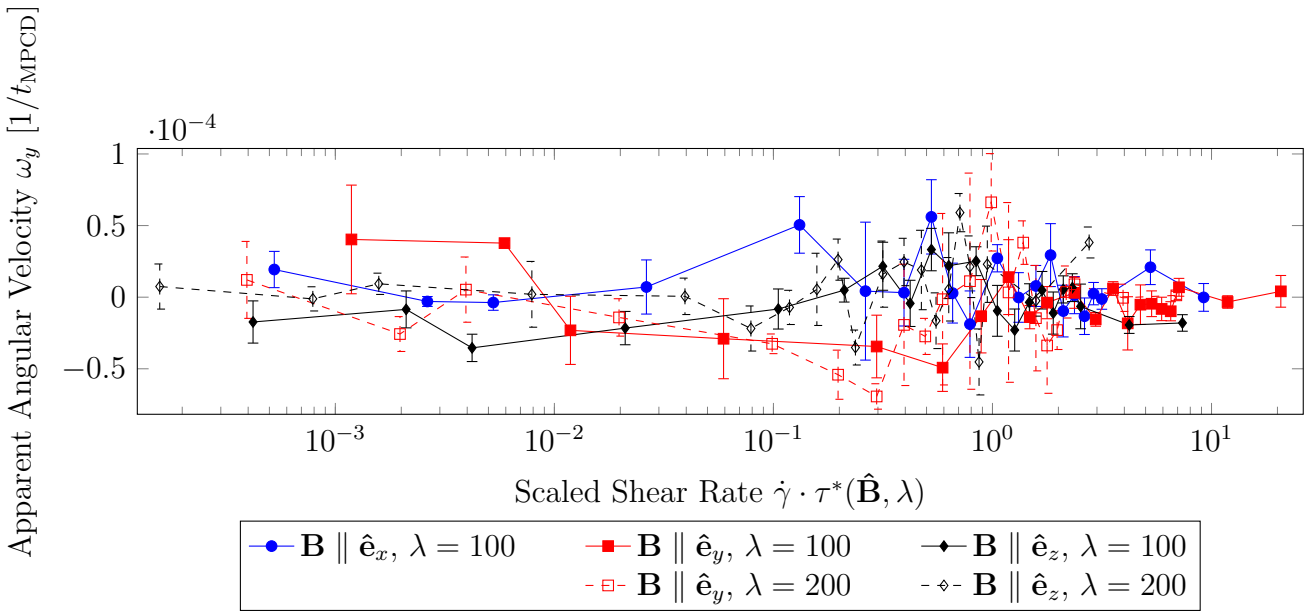

Figure 3.25: y-component ω_y of the apparent angular velocity $\boldsymbol{\omega}$, as defined in Eq. (3.17), in units of t_{MPCD}^{-1}. (See text for details.)

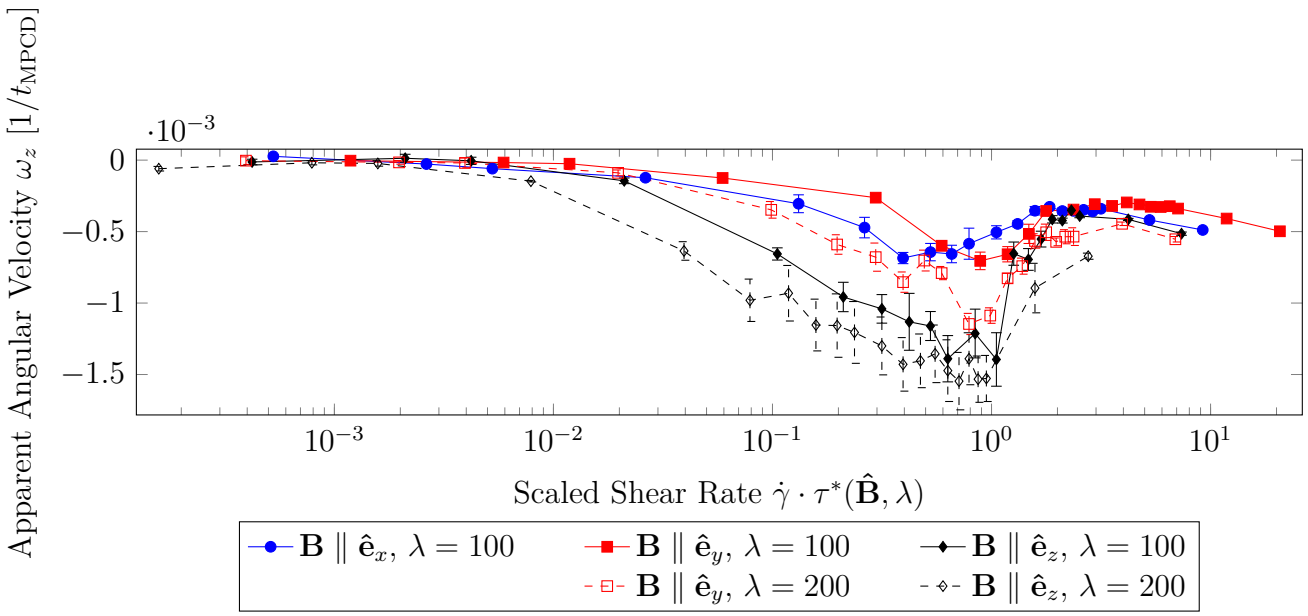

Figure 3.26: z-component ω_z of the apparent angular velocity $\boldsymbol{\omega}$, as defined in Eq. (3.17), in units of t_{MPCD}^{-1}. (See text for details.)

three *Eckart vectors* $\boldsymbol{\mathcal{F}}^{(1)}$, $\boldsymbol{\mathcal{F}}^{(2)}$ and $\boldsymbol{\mathcal{F}}^{(3)}$ via

$$\boldsymbol{\mathcal{F}}^{(\alpha)} := \sum_{i=1}^{N} m_i \mathcal{R}_{\alpha}^{(i)} \mathbf{r}_i, \tag{3.21}$$

with $\mathbf{r}_i$ being the instantaneous position of the i-th monomer. Further, let the three-dimensional symmetric *Gram matrix* $\mathcal{G}$ be defined via its components,

$$\mathcal{G}_{ij} = \boldsymbol{\mathcal{F}}^{(i)} \cdot \boldsymbol{\mathcal{F}}^{(j)}, \tag{3.22}$$

and let $\mathcal{G}^{-1/2}$ be a matrix satisfying $\mathcal{G}^{-1/2} \cdot \mathcal{G}^{-1/2} = \mathcal{G}^{-1}$, with $\mathcal{G}^{-1}$ being the inverse of $\mathcal{G}$. Then, the three *Eckart frame vectors*

$$\boldsymbol{\mathcal{E}}^{(i)} := \boldsymbol{\mathcal{F}}^{(i)} \cdot \mathcal{G}^{-1/2} \tag{3.23}$$

form a right-handed set of orthonormal basis vectors, different for each instantaneous configuration of the MFSP.

With

$$\tilde{\mathcal{R}}^{(i)} := \sum_{j=1}^{3} \mathcal{R}_{j}^{(i)} \boldsymbol{\mathcal{E}}^{(j)}, \tag{3.24}$$

one can further define the *Eckart moment of inertia tensor* $\mathcal{I}$ via

$$\mathcal{I} := \sum_{i=1}^{N} \left(m_i \left(\mathbf{r}_i \cdot \tilde{\mathcal{R}}^{(i)} \right) \mathbb{1} - \mathbf{r}_i \otimes \tilde{\mathcal{R}}^{(i)} \right), \tag{3.25}$$

where $\mathbb{1}$ is the identity (or unit) matrix, and $\otimes$ is the outer product (or tensor product). Finally, the *Eckart angular velocity* vector $\boldsymbol{\Omega}$ is given by

$$\boldsymbol{\Omega} := \mathcal{I}^{-1} \sum_{i=1}^{N} \tilde{\mathcal{R}}^{(i)} \times \mathbf{p}_i. \tag{3.26}$$

Although the choice of the initial configuration in constructing the Eckart frame is arbitrary, Sablić et al.[73] show that the resulting Eckart-frame angular velocities are essentially independent of the particular reference configuration.

[73] Sablić, Delgado-Buscalioni, and Praprotnik, "Application of the Eckart frame to soft matter: rotation of star polymers under shear flow".

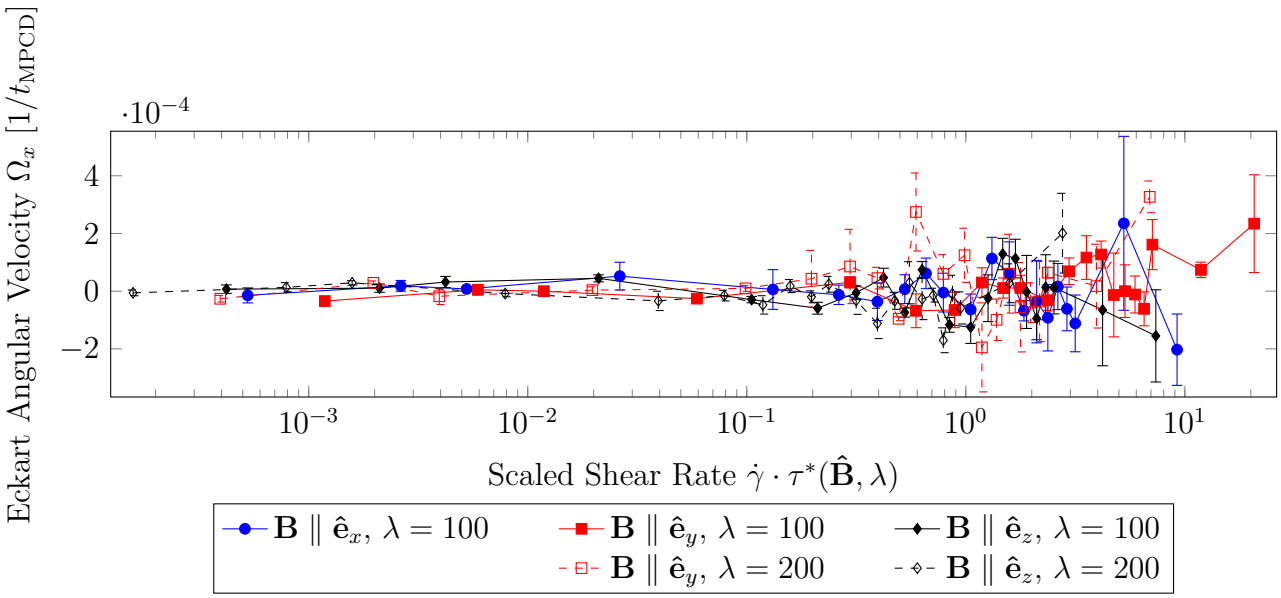

Figure 3.27: x-component Ω_x of the Eckart angular velocity $\mathbf{\Omega}$, as defined in Eq. (3.26), in units of t_{MPCD}^{-1}. (See text for details.)

Figs. 3.27 to 3.29 show the components of the Eckart angular velocity vector. While the data for the rotation around the x and y axes (i.e. the flow and gradient directions) are largely consistent with the absence of a net rotational movement, the data for rotation around the z (vorticity) axis conclusively show a net rotation, with the angular velocity increasing in magnitude with increasing shear rate $\dot{\gamma}$, except for a transient kink near the critical shear rate, where magnetic clusters start breaking up.

The apparent (i.e. non-Eckart) angular velocities, Figs. 3.24 to 3.26, paint a qualitatively mostly similar picture, except that, compared to the Eckart angular velocities, the apparent angular velocity about the z axis is relatively slow to pick up speed again beyond the critical shear rate.

This behavior differentiates the angular velocity from the other quantities studied above for MFSPs, in that there is a clear dependence on the cluster count N_{C}, as evidenced by the change in behavior near the critical shear rate $\tau^*(\hat{\mathbf{B}}, \lambda) \cdot \dot{\gamma} \approx 1$, but *on top* of that implicit $\dot{\gamma}$-dependence, there is another strong effect of $\dot{\gamma}$, in that higher shear rates increase the rotation frequency.

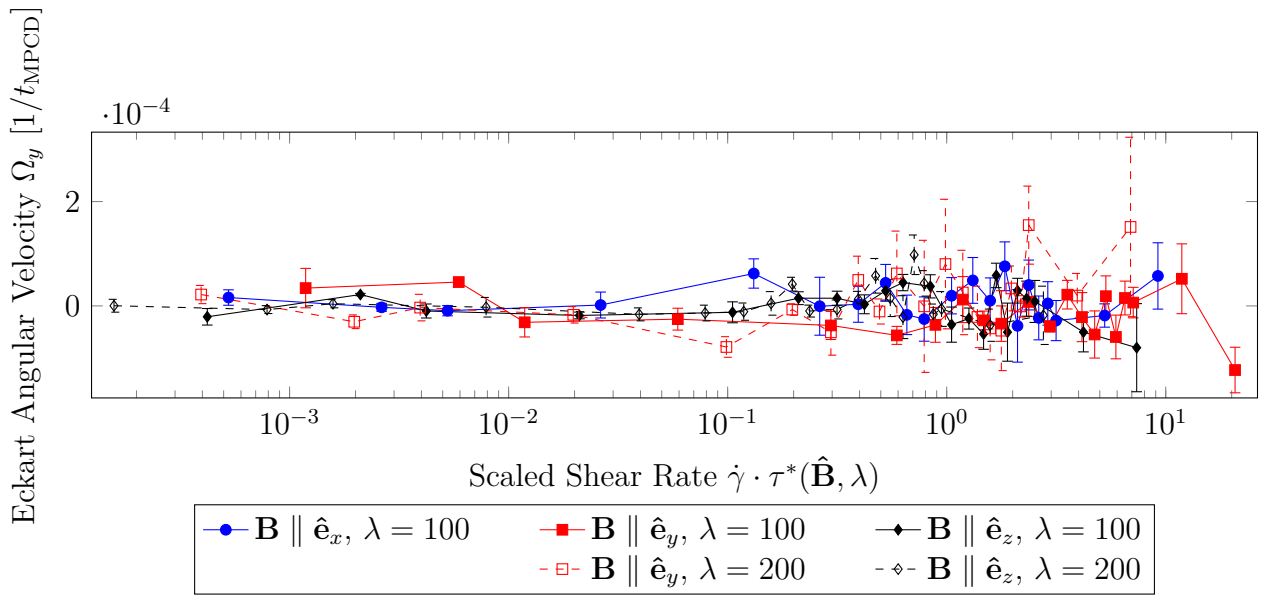

Figure 3.28: y-component Ω_y of the Eckart angular velocity $\mathbf{\Omega}$, as defined in Eq. (3.26), in units of t^{-1}_{MPCD}. (See text for details.)

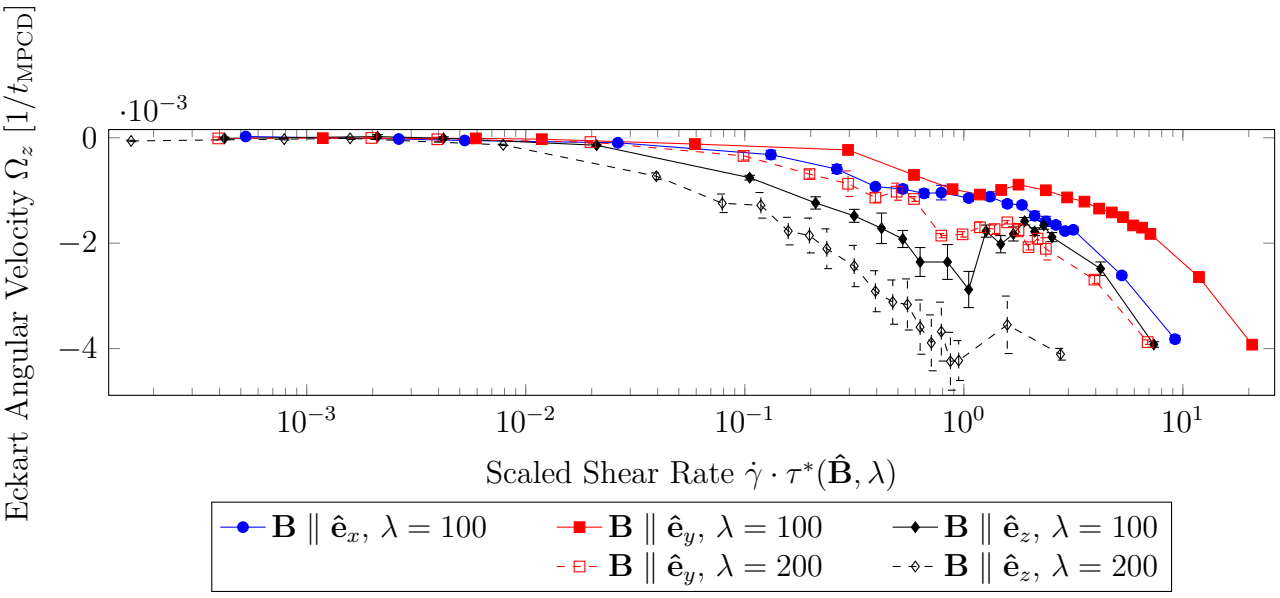

Figure 3.29: z-component Ω_z of the Eckart angular velocity $\mathbf{\Omega}$, as defined in Eq. (3.26), in units of t^{-1}_{MPCD}. (See text for details.)

3.6 Conclusions and Outlook

By decorating the free ends of star polymer arms with super-paramagnetic particles, one creates a soft, patchy colloid that exhibits interesting dependencies on an external magnetic field $\mathbf{B}$, regarding both its direction $\hat{\mathbf{B}}$ and its magnitude B, since $\lambda \propto B^2$. While some properties (orientational resistance) remain qualitatively unaffected by the new interaction, the number and orientation of linear magnetic clusters that self-assemble depends on $\mathbf{B}$. This number of magnetic clusters N_C, further dependent on the shear rate $\dot{\gamma}$ the star is subjected to, dictates the qualitative behavior of the size and shape of the star polymer for various values of $\dot{\gamma}$. Lastly, shear flow induces a net rotation of the star, with the angular velocity depending on N_C, $\hat{\mathbf{B}}$, and $\dot{\gamma}$ in intricate ways.

Further studies of this model, but with different parameters (e.g. for the number of arms, or non-homogeneous masses of monomers) would complement the picture of single stars in dilute solution. Of course, experimental realization and study of MFSPs would be highly interesting, and necessary to judge the quality of the model.

Entirely new insights might be gleaned from introducing viscoelasticity to the solvent – a topic to be discussed in the following chapters. In non-dilute solutions, inter-star organization might spontaneously emerge, with interesting dependencies on concentration and the parameters mentioned above. Dynamic (computer) experiments, where the external magnetic field is changed during observation, might be particularly rewarding, also in view of possible transitions from one kind of collective aggregate to another.

Chapter 4

Fluid Dynamics

4.1 Fundamental Principles

This section, which heavily borrows from Landau and Lifshitz,[1] is intended to give a quick review of the foundations of fluid dynamics most relevant to this thesis. Subsequent chapters will extend the material presented here. [Where indices are repeated within one expression, the Einstein summation convention is implied, cf. Appendix A.]

4.1.1 The Continuity Equation[2]

Let $\varrho(\mathbf{r}, t)$ be the density of the fluid at the position $\mathbf{r}$ and time t, and let there be an arbitrary, but fixed, non-degenerate 3-dimensional volume V, the 2-dimensional boundary of which is denoted by ∂V. The infinitesimal boundary surface element is referred to by the vector $\mathrm{d}\,\mathbf{f}(\mathbf{r})$, the magnitude of which is equal to the surface element's area, while the vector's direction is perpendicular to the surface, pointing outwards of the volume V. Finally, let $\mathbf{v}(\mathbf{r}, t)$ be the fluid's velocity field.

The fluid mass m_V inside the volume V is given by

$$m_V = \int_V \varrho(\mathbf{r}, t)\ \mathrm{d}^3 r\,. \tag{4.1}$$

The amount of mass per time flowing out of V through a particular surface element $\mathrm{d}\,\mathbf{f}$ is given by the component of the mass flux density $\varrho\mathbf{v}$ along $\mathrm{d}\,\mathbf{f}$,

$$\varrho\left(\mathbf{r},t\right)v_i\left(\mathbf{r},t\right)\,\mathrm{d}\,f_i\,, \tag{4.2}$$

so that the total amount of mass per time leaving V is

$$\oint\limits_{\partial V}\varrho\left(\mathbf{r},t\right)v_i\left(\mathbf{r},t\right)\,\mathrm{d}\,f_i\,. \tag{4.3}$$

The postulate of conservation of mass is formulated by equating this quantity to the negative time derivative of m_V, i.e. the mass flowing out of V per unit time. This leads to the integral form of the continuity equation, which states that mass can neither be created nor destroyed:

$$-\int\limits_V\partial_t\varrho\,\mathrm{d}^3\,r=\oint\limits_{\partial V}\varrho v_i\,\mathrm{d}\,f_i\,. \tag{4.4}$$

One can use Gauss's theorem to rewrite the right-hand side of the equation above as

$$\oint\limits_{\partial V}\varrho v_i\,\mathrm{d}\,f_i=\int\limits_V\partial_i\left(\varrho v_i\right)\,\mathrm{d}^3\,r \tag{4.5}$$

to obtain

$$\int\limits_V\left(\partial_i\left(\varrho v_i\right)+\partial_t\varrho\right)\,\mathrm{d}^3\,r=0\,. \tag{4.6}$$

Since this equation holds for arbitrary volumes V, the integrand has to be 0; thus, one arrives at the differential form of the continuity equation:

$$\partial_i\left(\varrho v_i\right)+\partial_t\varrho=0\,. \tag{4.7}$$

4.1.2 The Substantial Derivative[3]

When talking about time derivatives of vector fields that depend on the position and on time, such as the velocity field $\mathbf{v}\left(\mathbf{r},t\right)$, one sometimes refers to the *partial derivative*,

$$\partial_t\mathbf{v}\left(\mathbf{r},t\right)\,, \tag{4.8}$$

which describes the rate of change of $\mathbf{v}(\mathbf{r}, t)$ at a fixed point in space $\mathbf{r}$. Alternatively, one may refer to the *substantial derivative*

$$\mathrm{D}_t \mathbf{v}(\mathbf{r}, t) \ . \tag{4.9}$$

To define its meaning, one can imagine having a volume of fluid that is small compared to the volume the entire fluid occupies, but large compared to the fluid molecules. This mesoscopic fluid volume, sometimes called *fluid element*, can be thought to be marked in a way that distinguishes it from all the other parts of the fluid, e.g. by being dyed with a specific color. As time passes, the fluid element may not only change its shape – an effect that shall not be of concern here, provided one can still ascribe a position to the fluid element in a meaningful way – but may also have its position (i.e. its center of mass) moved in space.

It is the substantial derivative that describes how the velocity of the fluid element changes with time, and it has two contributions: On the one hand, the fluid element at position $\mathbf{r}$ witnesses how the velocity of the fluid at the fixed point $\mathbf{r}$ changes. On the other hand, since the fluid element is being transported from $\mathbf{r}(t)$ at time t to another position $\mathbf{r}(t + \mathrm{d}\, t)$ at time $t + \mathrm{d}\, t$, it also witnesses the fluid's velocity $\mathbf{v}(\mathbf{r}(t + \mathrm{d}\, t))$ at that new position.

Formally, the substantial derivative can be understood as the total time derivative of the fluid element's velocity as a function of time, $\mathbf{v}(\mathbf{r}(t), t)$, which can be found using the chain rule:

$$\begin{aligned} \mathrm{D}_t v_i &= \partial_t v_i + (\partial_j v_i)(\partial_t r_j) \\ &= \partial_t v_i + v_j \partial_j v_i \, . \end{aligned} \tag{4.10}$$

Since this relation holds for any $\mathbf{r}$- and t-dependent vector field for which the right-hand side of the above relation is defined, one can declare

$$\mathrm{D}_t := \partial_t + v_j \partial_j \, . \tag{4.11}$$

4.1.3 Euler's Equation for Ideal Fluids[4]

Given a fixed volume V with boundary ∂V and differential surface element $\mathrm{d}\,\mathbf{f}$, the force on the fluid volume due to (isotropic) pressure $p(\mathbf{r}, t)$ of the surrounding

medium is given by

$$-\oint_{\partial V} p\left(\mathbf{r},t\right)\,\mathrm{d}\,f_i\,, \tag{4.12}$$

which can be re-written, using Gauss's theorem, as

$$-\oint_{\partial V} p\left(\mathbf{r},t\right)\,\mathrm{d}\,f_i = -\int_V \partial_i p\left(\mathbf{r},t\right)\,\mathrm{d}^3\,r\,. \tag{4.13}$$

If V is taken to be infinitesimally small, the force density acting on V due to pressure is thus

$$-\partial_i p\left(\mathbf{r},t\right)\,. \tag{4.14}$$

With other external force densities f_i^{ext} acting on this volume element, the total force density then equals, according to Newton's second law, mass density times acceleration:

$$\varrho \mathrm{D}_t v_i = f_i^{\mathrm{ext}} - \partial_i p\,. \tag{4.15}$$

Insertion of the definition of the substantial derivative (4.11) and division by ϱ then leads to Euler's equation for *ideal fluids*, i.e. fluids in which energy dissipation is negligible:

$$\partial_t v_i + v_j \partial_j v_i = \varrho^{-1}\left(f_i^{\mathrm{ext}} - \partial_i p\right)\,. \tag{4.16}$$

4.1.4 Momentum Flux[5]

In order to study the evolution of the fluid's momentum density ϱv_i, one can use the continuity equation (4.7) to calculate

$$\begin{aligned}\partial_t\left(\varrho v_i\right) &= \varrho\partial_t v_i + v_i\partial_t\varrho \\ &= \varrho\partial_t v_i - v_i\partial_j\left(\varrho v_j\right)\,.\end{aligned} \tag{4.17}$$

Euler's equation (4.16) then allows the following reformulation:

$$\begin{aligned}\partial_t\left(\varrho v_i\right) &= f_i^{\mathrm{ext}} - \partial_i p - \varrho v_j\partial_j v_i - v_i\partial_j\left(\varrho v_j\right) \\ &= f_i^{\mathrm{ext}} - \partial_i p - \partial_j\left(\varrho v_i v_j\right) \\ &= f_i^{\mathrm{ext}} - \delta_{ij}\partial_j p - \partial_j\left(\varrho v_i v_j\right)\,.\end{aligned} \tag{4.18}$$

Defining the *momentum flux density tensor*

$$\Pi_{ij} := p\delta_{ij} + \varrho v_i v_j \,, \tag{4.19}$$

one arrives at

$$\partial_t \left(\varrho v_i\right) = f_i^{\text{ext}} - \partial_j \Pi_{ij} \,. \tag{4.20}$$

The physical meaning of Π_{ij} can be understood by integrating equation (4.20) for $f_i^{\text{ext}} = 0$ over an arbitrary, fixed volume V:

$$\begin{aligned} \partial_t \int\limits_V \varrho v_i \ \mathrm{d}^3 r &= - \int\limits_V \partial_j \Pi_{ij} \ \mathrm{d}^3 r \\ &= - \oint\limits_{\partial V} \Pi_{ij} \ \mathrm{d}\, f_j \,. \end{aligned} \tag{4.21}$$

Here, the left-hand side describes the rate of change of the i-component of the momentum in V (not accounting for external forces), while the right-hand side is a surface integral over Π_{ij}. Thus, Π_{ij} is the i-component of the momentum flowing out of the volume through a unit surface perpendicular to the j-axis during unit time. Then, with n_j being a unit vector, the i-component of the momentum flowing through a unit surface perpendicular to n_j per unit time is given by $\Pi_{ij} n_j$.

4.1.5 The Navier-Stokes Equation[6,7]

The previous sections described an ideal fluid, where no internal friction occurs. In order to introduce viscosity, one has to subtract a term σ'_{ij}, called *viscous stress tensor*, from the momentum flux density tensor (4.19):

$$\Pi_{ij} := p\delta_{ij} + \varrho v_i v_j - \sigma'_{ij} \,. \tag{4.22}$$

Defining the *stress tensor*[8]

$$\sigma_{ij} := -p\delta_{ij} + \sigma'_{ij} \,, \tag{4.23}$$

one can also write

$$\Pi_{ij} = \varrho v_i v_j - \sigma_{ij} \,. \tag{4.24}$$

To derive an expression for σ'_{ij}, one has to note there is no friction between neighboring fluid elements that move with the same velocity in the same direction;

thus, in the case of locally constant velocities, one must have $\sigma'_{ij} = 0$. Therefore, σ'_{ij} can neither have a constant contribution, nor can it depend on $\mathbf{v}$ directly. We adopt the conventional ansatz, which assumes that σ'_{ij} depends linearly on the first spatial derivatives of $\mathbf{v}$, so that[9]

$$\sigma'_{ij} = A_{ijkl}\partial_k v_l \,, \tag{4.25}$$

where the A_{ijkl} do not depend on $\mathbf{v}$ or any of its derivatives.

If the entire fluid undergoes rotational movement around an axis $\hat{\boldsymbol{\omega}}$ as if the fluid was a rigid body, i.e. if $\mathbf{v}(\mathbf{r}, t) = \boldsymbol{\omega} \times \mathbf{r}(t)$ with constant $\boldsymbol{\omega}$, then there cannot be friction, since in the co-rotating frame of reference, the fluid is at rest. So, in this case, one also has to have $\sigma'_{ij} = 0$; consequently, [with the Levi-Civita tensor ε_{ijk} as defined in Appendix D.2,]

$$\begin{aligned} \sigma'_{ij} &= A_{ijkl}\partial_k \varepsilon_{lmn}\omega_m r_n \\ &= A_{ijkl}\varepsilon_{lmn}\omega_m \partial_k r_n \\ &= A_{ijkl}\varepsilon_{lmn}\omega_m \delta_{kn} \\ &= A_{ijkl}\varepsilon_{mkl}\omega_m \stackrel{!}{=} 0 \,. \end{aligned} \tag{4.26}$$

Decomposing

$$A_{ijkl} = \frac{1}{2}\left(A_{ijkl} + A_{ijlk}\right) + \frac{1}{2}\left(A_{ijkl} - A_{ijlk}\right) \tag{4.27}$$

into a part

$$A_{ij(kl)} = \frac{1}{2}\left(A_{ijkl} + A_{ijlk}\right) \tag{4.28}$$

symmetric in the indices k and l, and a part

$$A_{ij[kl]} = \frac{1}{2}\left(A_{ijkl} - A_{ijlk}\right) \tag{4.29}$$

anti-symmetric in k and l, and noticing that the contraction of the anti-symmetric Levi-Civita tensor ε_{ijk} with a symmetric tensor S_{jk} gives 0 (cf. Appendices D.2 and D.3), one arrives at

$$A_{ij[kl]}\varepsilon_{mkl}\omega_m = 0 \tag{4.30}$$

for arbitrary $\boldsymbol{\omega}$. However, this means (see (D.6)) that

$$A_{ij[kl]} = 0 \,, \tag{4.31}$$

so that A_{ijkl} is symmetric in the indices k and l.

If one imposes isotropy on A_{ijkl}, i.e. if A_{ijkl} is to be indifferent to rotations of the Cartesian coordinate system, its most general form can be written as[10]

$$A_{ijkl} = s_1\delta_{ij}\delta_{kl} + s_2\left(\delta_{ik}\delta_{jl} + \delta_{il}\delta_{jk}\right) + s_3\left(\delta_{ik}\delta_{jl} - \delta_{il}\delta_{jk}\right) \tag{4.32}$$

with scalars s_1, s_2, and s_3, which are arbitrary *a priori*.

The requirement of symmetry in the indices k and l found in (4.31), however, requires that $s_3 = 0$. With this, the ansatz (4.25) becomes

$$\begin{aligned}\sigma'_{ij} &= s_1\delta_{ij}\delta_{kl}\partial_k v_l + s_2\left(\delta_{ik}\delta_{jl} + \delta_{il}\delta_{jk}\right)\partial_k v_l \\ &= s_1\delta_{ij}\partial_k v_k + s_2\left(\partial_i v_j + \partial_j v_i\right) \\ &= \left(s_1 + \frac{2}{3}s_2\right)\delta_{ij}\partial_k v_k + s_2\left(\partial_i v_j + \partial_j v_i - \frac{2}{3}\delta_{ij}\partial_k v_k\right) .\end{aligned} \tag{4.33}$$

Introducing the *dynamic viscosity*[11] $\eta := s_2$ and the *second viscosity* $\zeta_\mathrm{S} := s_1 + \frac{2}{3}s_2$, [also called *bulk viscosity*[12] or *dilatational viscosity*,[13]] the viscous stress tensor σ'_{ij} can then be re-written in the form

$$\sigma'_{ij} = \zeta_\mathrm{S}\delta_{ij}\partial_k v_k + \eta\left(\partial_i v_j + \partial_j v_i - \frac{2}{3}\delta_{ij}\partial_k v_k\right) . \tag{4.34}$$

This representation shows that the coefficient of η becomes zero if i and j are contracted, so that the trace of the viscous stress tensor becomes

$$\sigma'_{ii} = 3\zeta_\mathrm{S}\partial_i v_i . \tag{4.35}$$

The expression

$$\dot\gamma_{ij} := \partial_i v_j + \partial_j v_i \tag{4.36}$$

is called the *rate-of-strain tensor* or *rate-of-deformation tensor*,[14] which can be used to rewrite (4.34) as

$$\sigma'_{ij} = \left(\zeta_\mathrm{S} - \frac{2}{3}\eta\right)\delta_{ij}\partial_k v_k + \eta\dot\gamma_{ij} . \tag{4.37}$$

This new contribution σ'_{ij} to Π_{ij}, introduced in order to take viscosity into account, leads to an additional term in Euler's equation (4.16), which now reads

$$\varrho\left(\partial_t v_i + v_j\partial_j v_i\right) = f_i^\mathrm{ext} - \partial_i p + \partial_j\sigma'_{ij} . \tag{4.38}$$

In the case where $f_i^{\text{ext}} = 0$, $\partial_i \eta = 0$, and $\partial_i \zeta_{\text{S}} = 0$, [i.e. in the case of a force-free homogeneous fluid,] this relation can be simplified to

$$\begin{aligned} \varrho \left(\partial_t v_i + v_j \partial_j v_i \right) &= -\partial_i p + \zeta_{\text{S}} \partial_i \partial_k v_k + \eta \left(\partial_j \partial_i v_j + \partial_j \partial_j v_i - \frac{2}{3} \partial_i \partial_k v_k \right) \\ &= -\partial_i p + \eta \partial_j \partial_j v_i + \left(\zeta_{\text{S}} + \frac{\eta}{3} \right) \partial_i \partial_j v_j \end{aligned} \tag{4.39}$$

which is known as the *Navier-Stokes equation*. For a general external force density f_i^{ext}, this relation becomes

$$\varrho \left(\partial_t v_i + v_j \partial_j v_i \right) = f_i^{\text{ext}} - \partial_i p + \eta \partial_j \partial_j v_i + \left(\zeta_{\text{S}} + \frac{\eta}{3} \right) \partial_i \partial_j v_j \,. \tag{4.40}$$

4.1.6 Incompressibility[15]

If a fluid element's density is constant throughout time, i.e. if

$$\mathrm{D}_t \varrho = 0 \,, \tag{4.41}$$

the flow is called *incompressible*; if this condition is met for all [possible flows] for a given liquid, that liquid itself is called incompressible. Rewriting the continuity equation (4.7) as

$$\begin{aligned} 0 &= v_i \partial_i \varrho + \varrho \partial_i v_i + \partial_t \varrho \\ &= \varrho \partial_i v_i + \mathrm{D}_t \varrho \,, \end{aligned} \tag{4.42}$$

it is evident that the incompressibility condition (4.41) can be equivalently formulated as

$$\partial_i v_i = 0 \,. \tag{4.43}$$

For incompressible flows, the viscous stress tensor [Eq. (4.34)] becomes

$$\begin{aligned} \sigma'_{ij} &= \eta \left(\partial_i v_j + \partial_j v_i \right) \\ &= \eta \dot{\gamma}_{ij} \end{aligned} \tag{4.44}$$

and therefore the stress tensor [Eq. (4.23)] reads

$$\begin{aligned} \sigma_{ij} &= -p \delta_{ij} + \eta \left(\partial_i v_j + \partial_j v_i \right) \\ &= -p \delta_{ij} + \eta \dot{\gamma}_{ij} \,. \end{aligned} \tag{4.45}$$

The external-force Navier-Stokes equation [Eq. (4.40)] reduces to

$$\varrho\,(\partial_t v_i + v_j \partial_j v_i) = f_i^{\text{ext}} - \partial_i p + \eta \partial_j \partial_j v_i\,, \tag{4.46}$$

or equivalently,

$$\partial_t v_i + v_j \partial_j v_i = \varrho^{-1} f_i^{\text{ext}} - \varrho^{-1} \partial_i p + \nu \partial_j \partial_j v_i\,, \tag{4.47}$$

where the *kinematic viscosity* $\nu := \eta/\varrho$ has been introduced.

4.2 Adaptions of the Navier-Stokes Equation

4.2.1 The Linearized Navier-Stokes Equation

The dimensionless Reynolds number[16,17] $\mathrm{Re} := ul/\nu$, which is defined in terms of the kinematic viscosity ν, a characteristic length l (such as a linear extent of some rigid boundary), and a characteristic velocity u (such as the steady speed of said moving rigid boundary), serves as a measure for the importance of the inertial forces, compared to pressure and viscous forces.[18,19] For example, the Reynolds number's order of magnitude for a human swimming in water is about $\mathrm{Re} \approx 10^4$, while for an organism about $2\,\mu$m in size, such as the bacterium *E. coli*, the Reynolds number is $\mathrm{Re} \approx 10^{-4}$ or even less.[20]

In terms of these characteristic scales u, l, and ν, the summand $v_j \partial_j v_i$ in [Eq. (4.47)] is roughly of the order of magnitude[21] u^2/l, while the term $\nu \partial_j \partial_j v_i$ is of order of magnitude $\nu u/l^2$; the ratio of these two (crude) estimates is exactly the Reynolds number Re. So, for small Reynolds numbers, i.e. for $\mathrm{Re} \ll 1$, the term $[v_j \partial_j v_i]$ becomes small compared to $[\nu \partial_j \partial_j v_i]$, and thus can be neglected in equation (4.47). Omission of this term, which is non-linear in $\mathbf{v}$, thus leads to the *linearized Navier-Stokes equation*[22]

$$\varrho \partial_t v_i = f_i^{\text{ext}} - \partial_i p + \eta \partial_j \partial_j v_i\,. \tag{4.48}$$

4.2.2 Linear Viscoelasticity

One can generalize the derivation of the Navier-Stokes equation for incompressible fluids (see Sections 4.1.5 and 4.1.6), by introducing an explicit time-dependence in the dynamic viscosity η and in the rate-of-strain tensor $\dot{\gamma}_{ij}$, and connecting them in a convolution term.[23,24,25] Then, instead of (4.45), the relationship between σ_{ij} and $\dot{\gamma}_{ij}$ reads

$$\sigma_{ij}\left(\mathbf{r},t\right)=-p\left(\mathbf{r},t\right)\delta_{ij}+\int\limits_{t'=-\infty}^{t}G\left(t-t'\right)\dot{\gamma}_{ij}\left(\mathbf{r},t'\right)\,\mathrm{d}\,t'\,, \tag{4.49}$$

where the real quantity $G\left(\Delta t\right)$ [with $\Delta t=t-t'$] is called the *relaxation modulus*; it is assumed to be independent of the spatial coordinates $\mathbf{r}$. $G\left(\Delta t\right)$ describes how strain rates that occur during at a time Δt prior to t influence the stress of the fluid at time t. The range of integration, $t'\in(-\infty,t]$, is chosen accordingly, since it corresponds to $\Delta t\in[0,\infty]$, so that the system's state is determined only by its past, but not by its future. $G\left(\Delta t\right)$ is positive and monotonically decreasing[26] to 0 with increasing Δt, provided that one deals with viscoelastic *liquids*; the condition $\lim_{\Delta t\to\infty}\left(G\left(\Delta t\right)\right)=0$ means that the system is stress-free if a strain was placed on it only in the infinitely far past. This property is characteristic of liquids;[27,28] for a viscoelastic *solid*, this assumption does not hold.

A quantity related to the relaxation modulus is the *complex modulus*[29]

$$G^{*}\left(\omega\right)=\mathrm{i}\omega\int\limits_{t=0}^{\infty}G\left(t\right)\exp\left(-\mathrm{i}\omega t\right)\,\mathrm{d}\,t\,, \tag{4.50}$$

which is decomposed[30] into its real part, called the *storage modulus*[31]

$$\begin{aligned}G'\left(\omega\right)&=\mathrm{Re}\left(G^{*}\left(\omega\right)\right)\\&=\omega\int\limits_{t=0}^{\infty}G\left(t\right)\sin\left(\omega t\right)\,\mathrm{d}\,t\,,\end{aligned} \tag{4.51}$$

and its imaginary part, called the *loss modulus*:[32]

$$\begin{aligned}G''\left(\omega\right)&=\mathrm{Im}\left(G^{*}\left(\omega\right)\right)\\&=\omega\int\limits_{t=0}^{\infty}G\left(t\right)\cos\left(\omega t\right)\,\mathrm{d}\,t\,.\end{aligned} \tag{4.52}$$

With equation (4.49), the correspondingly extended Euler equation (4.38) reads, under the incompressibility condition $\partial_i v_i = 0$,

$$\begin{aligned} \varrho \left(\partial_t v_i + v_j \partial_j v_i\right) &= f_i^{\text{ext}} - \partial_i p + \int_{t'=-\infty}^{t} G\left(t-t'\right) \partial_j \dot{\gamma}_{ij}\left(t'\right) \,\mathrm{d}\, t' \\ &= f_i^{\text{ext}} - \partial_i p + \int_{t'=-\infty}^{t} G\left(t-t'\right) \partial_j \partial_j v_i\left(t'\right) \,\mathrm{d}\, t' \,, \end{aligned} \tag{4.53}$$

where some dependencies on $\mathbf{r}$ and t have been omitted for notational clarity. With this, the linearized Navier-Stokes equation (4.48) for linearly viscoelastic fluids reads

$$\varrho \partial_t v_i = f_i^{\text{ext}} - \partial_i p + \int_{t'=-\infty}^{t} G\left(t-t'\right) \partial_j \partial_j v_i\left(t'\right) \,\mathrm{d}\, t' \,. \tag{4.54}$$

D. Toneian. "Multi-Particle Collision Dynamics Simulation of Viscoelastic Fluids". Diploma thesis. TU Wien, 2015, Footnote/citation numbers and references to sections and equations have been adapted. Sections in square brackets have been added or adapted for improved clarity, as has been Eq. (4.46).

[1] L. D. Landau and E. M. Lifshitz. *Fluid Mechanics*. 2nd ed. Vol. 6. Course of Theoretical Physics. Pergamon Press, 1987.
[2] Landau and Lifshitz, *Fluid Mechanics*, § 1.
[3] Landau and Lifshitz, *Fluid Mechanics*, § 2.
[4] Landau and Lifshitz, *Fluid Mechanics*, § 2.
[5] Landau and Lifshitz, *Fluid Mechanics*, § 7.
[6] Landau and Lifshitz, *Fluid Mechanics*, § 15.
[7] G. K. Batchelor. *An Introduction to Fluid Dynamics*. Cambridge Mathematical Library. Cambridge University Press, 2000, § 3.3.
[8] Bird, Armstrong, and Hassager (1987) define the stress tensor as $\pi_{ij} = -\sigma_{ji}$.
[9] In Batchelor (2000), the indices k and l have reversed roles.
[10] H. Jeffreys. *Cartesian Tensors*. Cambridge University Press, 1931, Chapter VII, equation (20).
[11] For the dynamic viscosity, both the symbols η and μ are used in the literature.
[12] J.-P. Hansen and I. R. McDonald. *Theory of Simple Liquids*. 3rd ed. Academic Press, 2006, Section 8.3.
[13] R. B. Bird, R. C. Armstrong, and O. Hassager. *Fluid Mechanics*. 2nd ed. Vol. 1. Dynamics of Polymeric Liquids. John Wiley & Sons, 1987, §1.2.
[14] Bird, Armstrong, and Hassager, *Fluid Mechanics*, § 1.2.

[15]Landau and Lifshitz, *Fluid Mechanics*, § 15.
[16]Landau and Lifshitz, *Fluid Mechanics*, § 19.
[17]Batchelor, *An Introduction to Fluid Dynamics*, § 4.7.
[18]Batchelor, *An Introduction to Fluid Dynamics*, § 4.8.
[19]E. M. Purcell. "Life at low Reynolds number". *American Journal of Physics* **45** (1977), 3.
[20]Purcell, "Life at low Reynolds number".
[21]Landau and Lifshitz, *Fluid Mechanics*, § 20.
[22]Landau and Lifshitz, *Fluid Mechanics*, § 20.
[23]Bird, Armstrong, and Hassager, *Fluid Mechanics*, § 5.2d, equation (5.2-18).
[24]J. D. Ferry. *Viscoelastic Properties of Polymers*. 3rd ed. John Wiley & Sons, 1980, Section 1.B4, equation (7).
[25]Ferry, *Viscoelastic Properties of Polymers*, Section 1.G1, equation (59).
[26]Bird, Armstrong, and Hassager, *Fluid Mechanics*, § 5.2d.
[27]Ferry, *Viscoelastic Properties of Polymers*, Section 1.B4.
[28]Ferry, *Viscoelastic Properties of Polymers*, Section 1.G.
[29]Doi and Edwards, *The Theory of Polymer Dynamics*, Chapter 7.3, equation (7.22).
[30]Doi and Edwards, *The Theory of Polymer Dynamics*, Chapter 4.5.1.
[31]Doi and Edwards, *The Theory of Polymer Dynamics*, Equation (7.23).
[32]Doi and Edwards, *The Theory of Polymer Dynamics*, Equation (7.23).

Chapter 5

Viscoelasticity of Polymer Melts

This chapter presents theory and simulation data regarding polymer melts in MPCD simulations. Parts of the results shown are being prepared for publication by D. Toneian, G. Kahl, G. Gompper, and R. G. Winkler, with the provisional title "Simulating viscoelastic fluids by multiparticle collision dynamics – analytical and numerical velocity correlation functions".

The basics of this subject have been addressed in the thesis author's *Diplomarbeit*[1], but major progress has been achieved in the course of the author's present thesis. Where text or results from the *Diplomarbeit* have been reused, appropriate citations are provided (cf. Section 1.3).

5.1 The Rouse Model

Section 2.4 has introduced the general bead-spring model, where a polymer is represented by a series of *effective*, massive, point-like monomers, also called *beads*, connected by massless springs.

In the case of the *Rouse model*, these springs are taken to be harmonic; that is, given the positions $\mathbf{r}_i$ and $\mathbf{r}_{i-1}$ of the i-th monomer and its predecessor along the linear chain, the interaction potential obeys

$$V_{\mathrm{R}}\left(\mathbf{r}_i - \mathbf{r}_{i-1}\right) := \frac{K}{2}\left(\mathbf{r}_i - \mathbf{r}_{i-1}\right)^2, \tag{5.1}$$

where K is the *spring constant*.

In particular, there is no excluded-volume effect, such that monomers can effortlessly pass through one another. Although the minimum energy configuration is evidently the one where

[1] Toneian, "Multi-Particle Collision Dynamics Simulation of Viscoelastic Fluids".

all monomers occupy the same point in space, thermal and hydrodynamic fluctuations drive the polymer away from this mechanical equilibrium. Therefore, the *mean squared bond length*, b^2, is not zero either, but is instead given by[2,3]

$$b^2 = \frac{3k_\mathrm{B}T}{K}. \tag{5.2}$$

In this chapter, simulations are performed using a hybrid MPCD and MD method, as described in Chapter 6 (where the simulation parameter values are stated as well), with the modification that the bare MPCD particles are replaced by groups of $(N_\mathrm{S}+1)$ MPCD particles, connected via N_S springs obeying Eq. (5.1), such that the MPCD liquid represents a melt of Rouse polymers. To aid readability, MPCD units will be suppressed in what follows when reporting either simulation parameters or measured data, and $k_\mathrm{B}T = 1$, as set by the MBS thermostat in the simulations (cf. Section 6.1.4), will be implied throughout.

When comparing the measured mean square bond lengths b^2 from simulations of polymers with a prescribed spring constant K with the Rouse prediction Eq. (5.2), one discovers that there is excellent agreement, as shown in Fig. 5.1. Therefore, in the following it will be assumed that b^2 is precisely known, even though the simulation input parameter is the spring constant K.

[2] Teraoka, *Polymer Solutions*, Section 3.4.1.1.

[3] B. Kowalik and R. G. Winkler. "Multiparticle collision dynamics simulations of viscoelastic fluids: Shear-thinning Gaussian dumbbells". *The Journal of Chemical Physics* **138** (2013), 104903. Equation (3) in conjunction with $\lambda_0 = 3/(2l^2)$ below it in the text.

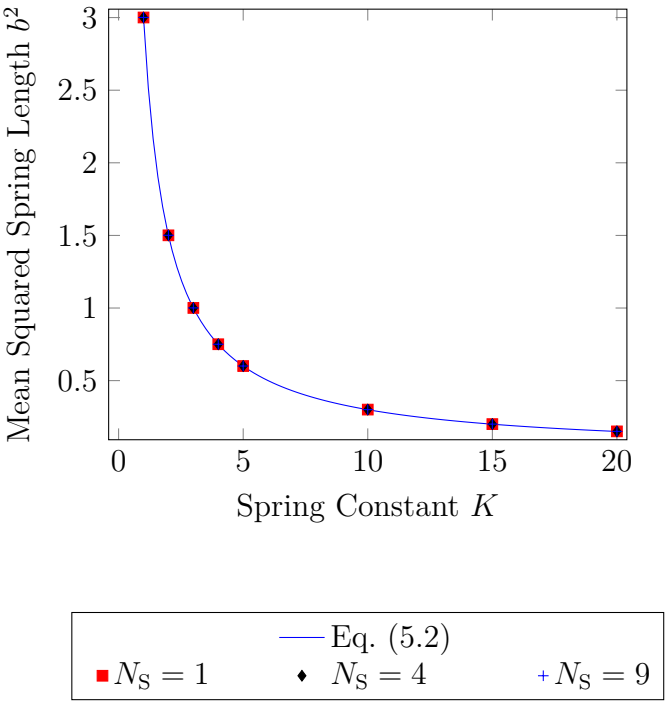

Figure 5.1: The mean squared spring length, b^2, as a function of the input parameter K, i.e. the spring constant. The symbols correspond to measured data, while the solid line corresponds to the N_S-independent Eq. (5.2). Due to excellent agreement, some symbols are hidden from view by others.

5.2 Diffusion

In studying the behavior of particles in solution, the center-of-mass diffusion coefficient D_{cm} plays a central role. For the Rouse model, it is given by[4]

$$D_{\mathrm{cm}} = \frac{k_{\mathrm{B}}T}{(N_{\mathrm{S}}+1)\,\zeta_{\mathrm{B}}}. \tag{5.3}$$

This equation can be identified with the Einstein relation,[5] $D = k_{\mathrm{B}}T/\zeta$, for a single particle diffusing (with diffusion coefficient D) in a fluid under the influence of the friction coefficient ζ. Thus, for a Rouse polymer with $N_{\mathrm{B}} = N_{\mathrm{S}}+1$ beads, each of which has a diffusion coefficient ζ_{B} in isolation, one can make an ansatz for the effective polymer friction coefficient $\zeta_{N_{\mathrm{B}}}$ of the polymer as a whole,[6]

$$\zeta_{N_{\mathrm{B}}} = N_{\mathrm{B}}\zeta_{\mathrm{B}}, \tag{5.4}$$

and correspondingly have an effective polymer center-of-mass diffusion coefficient $D_{\mathrm{cm}} = k_{\mathrm{B}}T/\zeta_{N_{\mathrm{B}}}$.

The center-of-mass diffusion coefficient can be extracted from simulation data by measuring the mean square displacement MSD of the center of mass of a polymer, and fitting the data thusly obtained to $\mathrm{MSD} = 6D_{\mathrm{cm}}t$. The result can then be compared to a theory prediction for the diffusion coefficient D_{B} of monomeric MPCD particles:[7]

$$D_{\mathrm{B}} = \frac{k_{\mathrm{B}}T\Delta t_{\mathrm{MPCD}}}{2m_{\mathrm{MPCD}}}\left(\frac{3N_c}{(1-\cos(\alpha_{\mathrm{SRD}}))\,(N_c-1+\exp(-N_c))}-1\right), \tag{5.5}$$

where Δt_{MPCD}, m_{MPCD}, α_{SRD}, and N_c are the MPCD streaming time-step, the MPCD particle mass, the SRD/MPCD collision angle, and the average number of MPCD particles per collision cell, respectively (cf. Chapter 6). For the parameters used, one computes $D_{\mathrm{B}} \approx 0.051$ and, via Eq. (5.3), $\zeta_{\mathrm{B}} \approx 19.454$.

[4] Teraoka, *Polymer Solutions*, Equations (3.152) and (3.130).
[5] Doi and Edwards, *The Theory of Polymer Dynamics*, Equation (3.10).
[6] Teraoka, *Polymer Solutions*, Equation (3.160).
[7] G. Gompper, T. Ihle, D. M. Kroll, and R. G. Winkler. *Multi-Particle Collision Dynamics: A Particle-Based Mesoscale Simulation Approach to the Hydrodynamics of Complex Fluids.* Advances in Polymer Science. Springer, 2008. Table 1.

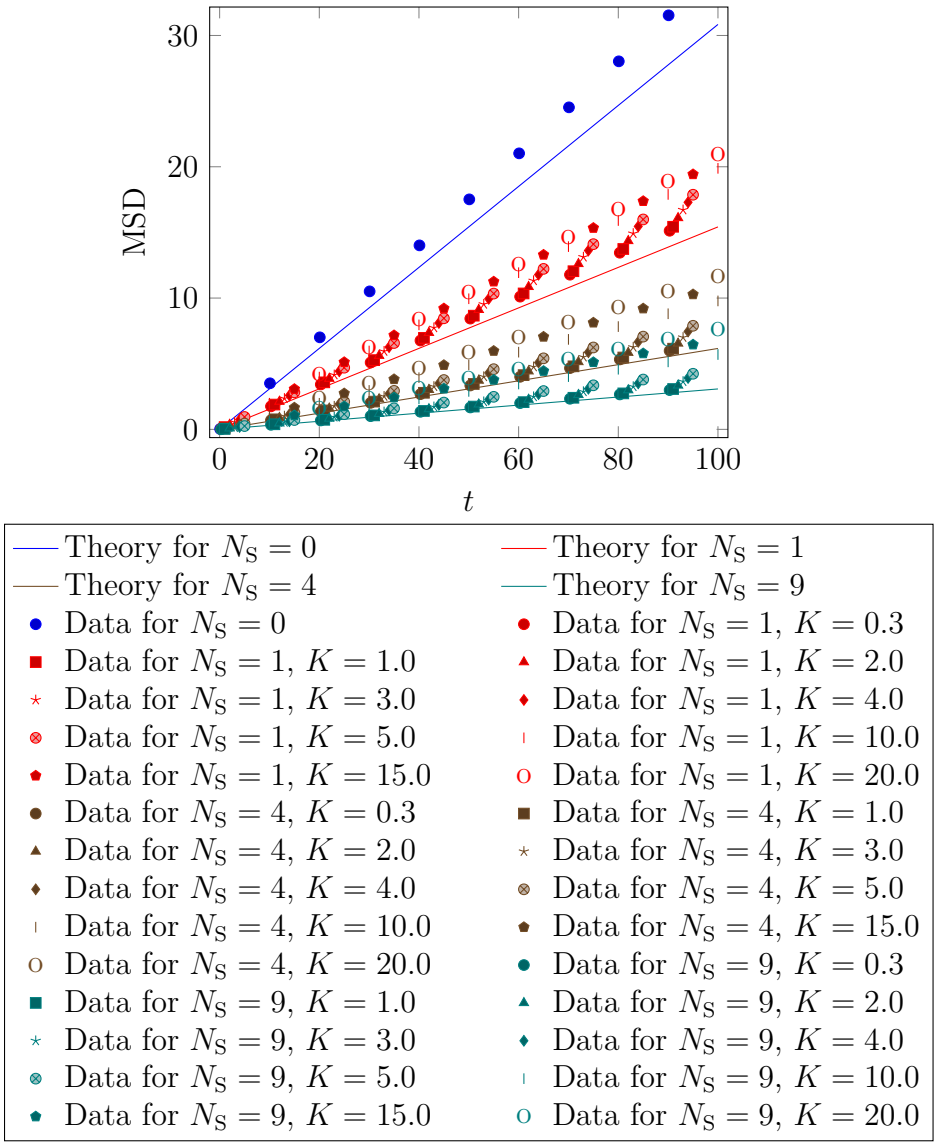

Figure 5.2: Comparison of the prediction of the mean square displacement, MSD $= 6D_{\mathrm{cm}}t$, using $\zeta_{\mathrm{B}} \approx 19.454$ as obtained from Eq. (5.5), with measured data. Only a subset of data points are shown (with different t-points chosen for different datasets) in the interest of clarity.

Fig. 5.2 shows the measured MSD as a function of simulation time t, along with the straight lines that correspond to Eq. (5.5). It is easily apparent that first, the true MSD, and hence the diffusion coefficient, is systematically underestimated, and second, that there is a dependence of MSD on the spring constant K, or conversely on the mean squared spring length b^2, which is not captured by the Rouse theory.

The Zimm model for a Θ-solvent, on the other hand, *does* predict a K-dependence, since[8]

$$D_{\mathrm{cm}} = \frac{8k_{\mathrm{B}}T}{3\eta\sqrt{6\pi^3 b^2\,(N_{\mathrm{S}}+1)}} \tag{5.6}$$

which can be expressed in terms of the spring constant K via Eq. (5.2) as

$$D_{\mathrm{cm}} = \frac{8\sqrt{k_{\mathrm{B}}TK}}{9\eta\sqrt{2\pi^3\,(N_{\mathrm{S}}+1)}}. \tag{5.7}$$

While the agreement between the data and the theory, as shown in Fig. 5.3, does seem to improve with increasing N_{S} such that one might suspect correct predictions of the qualitative behavior for very high spring counts, the quality of the match is generally lacking. For polymers with low N_{S} in particular, the reason may lie in the continuous polymer ($N_{\mathrm{S}} \to \infty$) approximation employed in deriving Eq. (5.7), which of course is violated for N_{S} values of order unity.

Regardless, Fig. 5.3 makes it clear that calculations and analyses which sensitively depend on the diffusion coefficient have to be carried out using the measured values, rather than the ones predicted by either Rouse or Zimm theories. This procedure will be implied in what follows, unless noted otherwise.

5.3 Normal Modes

Given a Rouse polymer, the equations of motion for its monomers form a set of coupled differential equations, which makes a treatment in terms of the monomer position vectors $\mathbf{r}_n$ complicated. However, one can define what is known as *normal mode coordinates* or *normal modes*, such that the equations of motion for these normal modes decouple from one another, allowing for significantly easier analysis.[9]

[8] Doi and Edwards, *The Theory of Polymer Dynamics*, Equation (4.61).
[9] Teraoka, *Polymer Solutions*, Section 3.4.2.

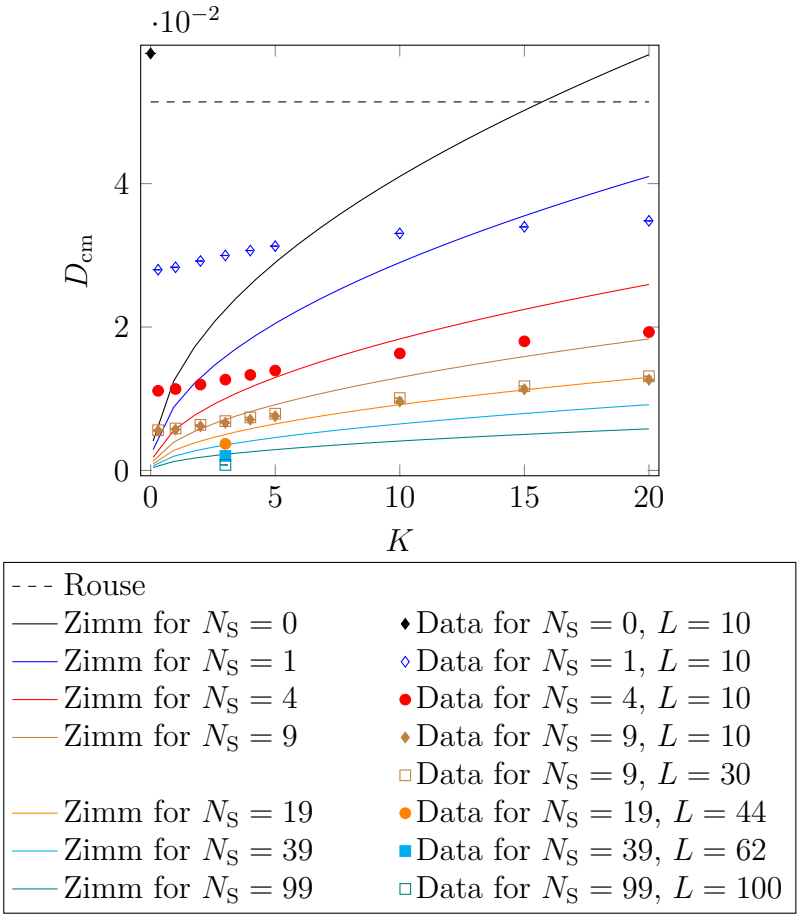

Figure 5.3: Measured diffusion constants (symbols), for various spring counts N_{S} and simulation box sizes L, as a function of the spring constant K. Lines correspond to predictions by either the Rouse (dashed, Eq. (5.5)) or Zimm (solid, Eq. (5.7)) theory. For larger spring counts ($N_{\mathrm{S}} > 9$), to counteract finite-size effects and self-interaction through periodic boundary conditions, the simulation box sizes have been scaled such that $(N_{\mathrm{S}} + 1)/L$ is approximately constant, L being restricted to integers; the fluid density ϱ has been kept constant throughout.

Unfortunately, the precise definition of the normal mode coordinates varies in the literature, partly due to the fact that many authors are interested in the continuous polymer limit of large numbers of springs N_S, where the differences in definition can typically be neglected.

Meyer et al.[10] and Durand et al.[11] define the normal modes $\mathbf{X}_p$ in a way that is valid for discrete (low-N_S) polymers, via

$$\mathbf{X}_p(t) := \frac{1}{N_\mathrm{S}+1} \sum_{n=1}^{N_\mathrm{S}+1} \mathbf{r}_n(t) \cos\left(\frac{\left(n-\frac{1}{2}\right)p\pi}{N_\mathrm{S}+1}\right), \tag{5.8}$$

with $p \in [0, N_\mathrm{S}]$. The case $p = 0$ differs from the cases $p > 0$ in that $p = 0$ describes the position of the polymer's center of mass, while the modes with $p > 0$ describe the internal degrees of freedom. In what follows, only $p > 0$ is considered.

The equations of motion for the normal modes can then be integrated to obtain the equal-time (i.e., $t' = t$) autocorrelation function, which is given by[12,13,14,15]

$$C_{p,q}^{(X)}(0) := \langle \mathbf{X}_p(t) \cdot \mathbf{X}_q(t) \rangle = \delta_{p,q} \frac{b^2}{8(N_\mathrm{S}+1)} \left[\sin\left(\frac{p\pi}{2(N_\mathrm{S}+1)}\right)\right]^{-2}, \tag{5.9}$$

which approaches $\delta_{p,q}\frac{(N_\mathrm{S}+1)b^2}{2\pi^2 p^2}$ in the limit $p \ll N_\mathrm{S}+1$. Here, $\delta_{p,q}$ is the Kronecker symbol, cf. Appendix D.1.

As is shown in Fig. 5.4, the prediction of Eq. (5.9) matches the measured equal-time normal mode autocorrelation remarkably well, with a considerable deviation only for the case where $p = 1$, $K = 0.3$, and $N_\mathrm{S} = 9$.

The time-dependent normal mode autocorrelation function[16]

$$C_{p,q}^{(X)}(t) := \langle \mathbf{X}_p(t_0+t) \cdot \mathbf{X}_q(t_0) \rangle = C_{p,q}^{(X)}(0) \cdot \exp\left(-\frac{|t|}{\tau_{\mathrm{X},p}}\right) \tag{5.10}$$

[10] H. Meyer, J. P. Wittmer, T. Kreer, P. Beckrich, A. Johner, J. Farago, and J. Baschnagel. "Static Rouse modes and related quantities: Corrections to chain ideality in polymer melts". *The European Physical Journal E* **26** (2008), 25. Equation (5).

[11] M. Durand, H. Meyer, O. Benzerara, J. Baschnagel, and O. Vitrac. "Molecular dynamics simulations of the chain dynamics in monodisperse oligomer melts and of the oligomer tracer diffusion in an entangled polymer matrix". *The Journal of Chemical Physics* **132** (2010), 194902. Equation (6).

[12] Meyer, Wittmer, Kreer, Beckrich, Johner, Farago, and Baschnagel, "Static Rouse modes and related quantities: Corrections to chain ideality in polymer melts", Equation (8).

[13] Durand, Meyer, Benzerara, Baschnagel, and Vitrac, "Molecular dynamics simulations of the chain dynamics in monodisperse oligomer melts and of the oligomer tracer diffusion in an entangled polymer matrix", Equation (11).

[14] Teraoka, *Polymer Solutions*, Equation (3.145).

[15] Doi and Edwards, *The Theory of Polymer Dynamics*, Equation (4.23).

[16] Doi and Edwards, *The Theory of Polymer Dynamics*, Equation (4.23).

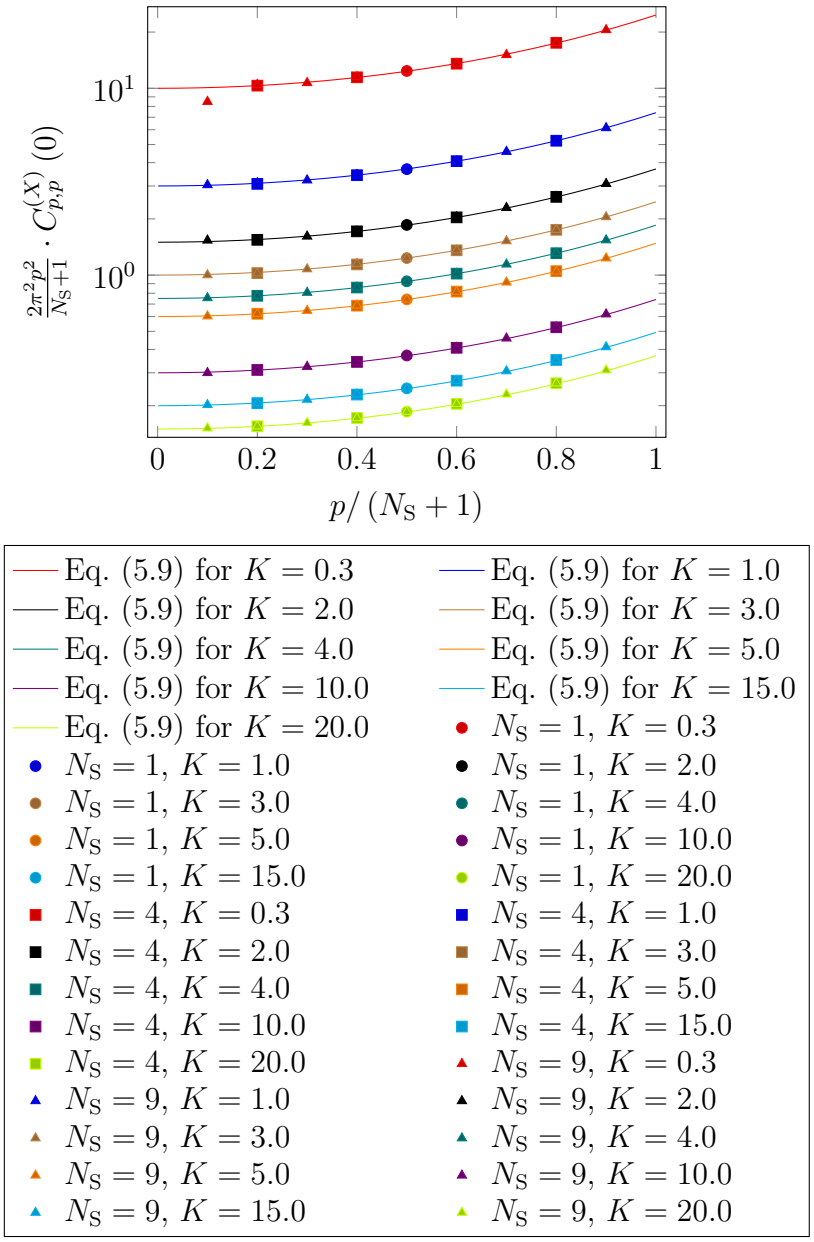

Figure 5.4: Comparison of the theoretical expression in Eq. (5.9) for the equal-time normal mode autocorrelation function (solid lines) with the measured data (symbols) for various polymer spring counts and spring constants. Different colors correspond to different spring constants K, while the different symbols correspond to different spring counts N_S.

decays exponentially with a characteristic normal mode autocorrelation time[17,18]

$$\tau_{\mathrm{X},p} := \frac{\zeta_\mathrm{B} b^2}{12 k_\mathrm{B} T \sin^2\left(\frac{p\pi}{2(N_\mathrm{S}+1)}\right)} = \frac{\zeta_\mathrm{B}}{4K \sin^2\left(\frac{p\pi}{2(N_\mathrm{S}+1)}\right)}. \tag{5.11}$$

Note that in the literature, both $\tau_{\mathrm{X},p}$ and the stress relaxation time $\tau_{\mathrm{S},p}$, to be defined below (Eq. (5.15)), are often referred to as τ_p – sometimes within one text – as if the quantities were equivalent, when the correct relationship really is[19]

$$2\tau_{\mathrm{S},p} = \tau_{\mathrm{X},p}\,. \tag{5.12}$$

Figs. 5.5 and 5.6 show the measured time-dependent normal mode autocorrelation functions for a selection of spring counts N_S and spring constants K, along with the predictions of Eqs. (5.10) and (5.11). The only parameter entering which is not an input into the simulation (treating b^2 as known, cf. Section 5.1) is the single-bead friction constant ζ_B, which enters in Eq. (5.11). In Figs. 5.5 and 5.6, ζ_B is taken to be $\zeta_\mathrm{B} = k_\mathrm{B}T/D_\mathrm{B}$ in accordance with Eq. (5.3), and $D_\mathrm{B} \approx 0.051$ as calculated via Eq. (5.5). The results confirm that the MPCD polymers behave in accordance with the Rouse model; deviations from the exponential decay law for large times t are mostly due to limited statistics in the data gathered.

[17] Durand, Meyer, Benzerara, Baschnagel, and Vitrac, "Molecular dynamics simulations of the chain dynamics in monodisperse oligomer melts and of the oligomer tracer diffusion in an entangled polymer matrix", Equation (7) and the text immediately above.

[18] Teraoka, *Polymer Solutions*.

[19] Doi and Edwards, *The Theory of Polymer Dynamics*.

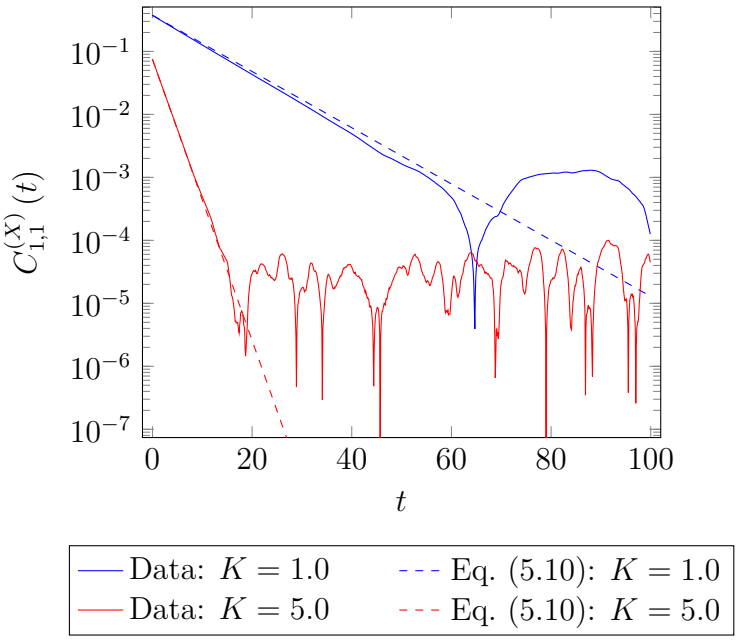

Figure 5.5: Comparison of data (solid lines) and theoretical predictions (dashed) for the time-dependent normal mode autocorrelation function, Eq. (5.10), with mode index $p = 1$, for the case where $N_S = 1$. Quantities are given in MPCD units, as described in Chapter 6.

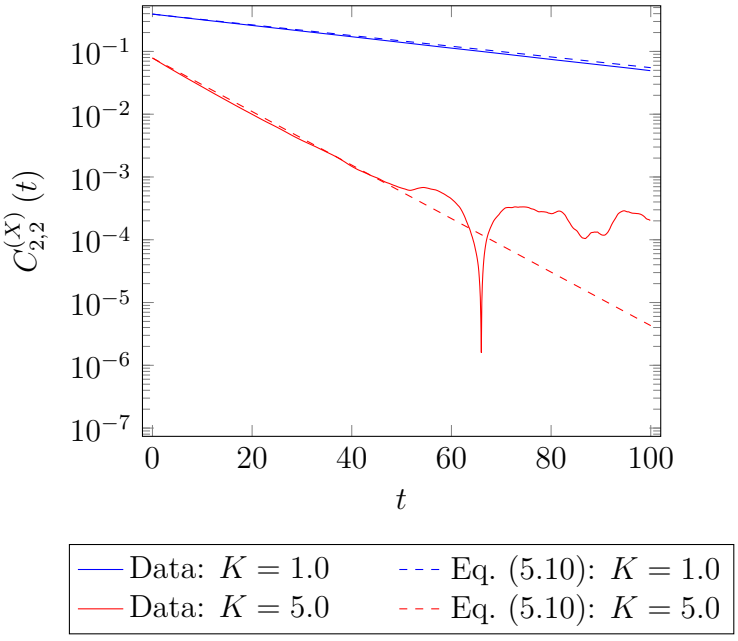

Figure 5.6: Comparison of data (solid lines) and theoretical predictions (dashed) for the time-dependent normal mode autocorrelation function, Eq. (5.10), with mode index $p = 2$, for the case where $N_S = 9$. Quantities are given in MPCD units, as described in Chapter 6.

5.4 Stress Relaxation

Owing to the Rouse model's simplicity, one can find closed expressions for its storage and loss moduli, defined in Eq. (4.51) and Eq. (4.52), respectively. They are, for the storage modulus,[20,21]

$$G'(\omega) = \varphi k_{\mathrm{B}} T \sum_{p=1}^{N_{\mathrm{S}}} \frac{\omega^2 \tau_{\mathrm{S},p}^2}{1 + \omega^2 \tau_{\mathrm{S},p}^2}\,, \tag{5.13}$$

and for the loss modulus,[22,23,24]

$$G''(\omega) = \omega\eta + \varphi k_B T \sum_{p=1}^{N_{\mathrm{S}}} \frac{\omega \tau_{\mathrm{S},p}}{1 + \omega^2 \tau_{\mathrm{S},p}^2}\,, \tag{5.14}$$

with φ being the number of polymer chains per unit volume.[25]

The *stress relaxation times* $\tau_{\mathrm{S},p}$ are given by[26]

$$\tau_{\mathrm{S},p} = \frac{\zeta_{\mathrm{B}} b^2}{24 k_{\mathrm{B}} T \sin^2\left(\frac{p\pi}{2(N_{\mathrm{S}}+1)}\right)} > 0\,. \tag{5.15}$$

Hence, the stress relaxation times are related to one another via the relation[27]

$$\frac{\tau_{\mathrm{S},p}}{\tau_{\mathrm{S},1}} = \frac{\sin^2\left(\frac{\pi}{2(N_{\mathrm{S}}+1)}\right)}{\sin^2\left(\frac{p\pi}{2(N_{\mathrm{S}}+1)}\right)}, \tag{5.16}$$

[20] Rouse, "A Theory of the Linear Viscoelastic Properties of Dilute Solutions of Coiling Polymers", Equation (30a).
[21] Y.-G. Tao, I. O. Götze, and G. Gompper. "Multiparticle collision dynamics modeling of viscoelastic fluids". *The Journal of Chemical Physics* **128** (2008), 144902. arXiv: `0802.2200 [cond-mat.soft]`. Equation (30).
[22] Rouse, "A Theory of the Linear Viscoelastic Properties of Dilute Solutions of Coiling Polymers", Equation (30b).
[23] Bird, Curtiss, Armstrong, and Hassager, *Kinetic Theory*, Equations (13.4-21) and (13.4-22).
[24] Tao, Götze, and Gompper, "Multiparticle collision dynamics modeling of viscoelastic fluids", Equation (31).
[25] Toneian, "Multi-Particle Collision Dynamics Simulation of Viscoelastic Fluids".
[26] Rouse, "A Theory of the Linear Viscoelastic Properties of Dilute Solutions of Coiling Polymers", Equation (31).
[27] Rouse, "A Theory of the Linear Viscoelastic Properties of Dilute Solutions of Coiling Polymers", Equation (31).

which for small p/N_S can be approximated[28] as $\tau_{\mathrm{S},p} \approx \tau_{\mathrm{S},1}/p^2$. η is the dynamic viscosity of the solvent the Rouse polymer is embedded in. In the following, it is assumed that $\eta = \eta_\mathrm{bare}$,[29] the dynamic viscosity of the bare MPCD fluid,[30] i.e. one consisting of point-like particles, even though no explicit solvent remains when the fluid is represented entirely by polymers.

In order to retrieve the relaxation modulus $G(t)$ from the complex modulus $G^*(\omega)$ (cf. (4.50)),

$$G^*(\omega) = \mathrm{i}\omega \int_{t'=0}^{\infty} G(t') \exp(-\mathrm{i}\omega t') \,\mathrm{d}\, t' \,, \tag{5.17}$$

one can multiply both sides of this equation by $-\mathrm{i}\omega^{-1} \exp(\mathrm{i}\omega t)$ and integrate ω over $\mathbb{R}$:

$$\int_{\omega=-\infty}^{\infty} \frac{G^*(\omega) \exp(\mathrm{i}\omega t)}{\mathrm{i}\omega} \,\mathrm{d}\,\omega = \int_{\omega=-\infty}^{\infty} \int_{t'=0}^{\infty} G(t') \exp(\mathrm{i}\omega(t-t')) \,\mathrm{d}\, t' \,\mathrm{d}\,\omega \,. \tag{5.18}$$

One can carry out the integration over ω on the right hand side, using the representation (B.5) of the Dirac delta function, to obtain

$$\begin{aligned} \int_{\omega=-\infty}^{\infty} \frac{G^*(\omega) \exp(\mathrm{i}\omega t)}{\mathrm{i}\omega} \,\mathrm{d}\,\omega &= 2\pi \int_{t'=0}^{\infty} G(t') \,\delta(t-t') \,\mathrm{d}\, t' \\ &= 2\pi G(t) \,\Theta(t) \,, \end{aligned} \tag{5.19}$$

[with the Heaviside step function $\Theta(t)$, as defined in Appendix A.]

In order to simplify the left-hand side, one can use the definitions (4.51) and (4.52) of the storage and loss moduli,

$$G^*(\omega) = G'(\omega) + \mathrm{i}G''(\omega) \,, \tag{5.20}$$

and insert the expressions (5.13) and (5.14):

$$G^*(\omega) = \varphi k_B T \sum_{p=1}^{N_\mathrm{S}} \frac{\omega^2 \tau_{\mathrm{S},p}^2}{1+\omega^2\tau_{\mathrm{S},p}^2} + \mathrm{i}\omega\eta + \mathrm{i}\varphi k_B T \sum_{p=1}^{N_\mathrm{S}} \frac{\omega\tau_{\mathrm{S},p}}{1+\omega^2\tau_{\mathrm{S},p}^2} \,. \tag{5.21}$$

[28] Doi and Edwards, *The Theory of Polymer Dynamics*, Chapter 4.1.
[29] Tao, Götze, and Gompper, "Multiparticle collision dynamics modeling of viscoelastic fluids", Section II.G.
[30] Gompper, Ihle, Kroll, and Winkler, *Multi-Particle Collision Dynamics: A Particle-Based Mesoscale Simulation Approach to the Hydrodynamics of Complex Fluids.*

Division by $\mathrm{i}\omega$ then yields

$$\frac{G^*(\omega)}{\mathrm{i}\omega} = \eta + \varphi k_B T \sum_{p=1}^{N_\mathrm{S}} \frac{\tau_{\mathrm{S},p} - \mathrm{i}\omega\tau_{\mathrm{S},p}^2}{1+\omega^2\tau_{\mathrm{S},p}^2}\,. \tag{5.22}$$

Writing the denominator as $1+\omega^2\tau_{\mathrm{S},p} = (1-\mathrm{i}\omega\tau_{\mathrm{S},p})\,(1+\mathrm{i}\omega\tau_{\mathrm{S},p})$, one can cancel one of the factors with the numerator, arriving at

$$\frac{G^*(\omega)}{\mathrm{i}\omega} = \eta + \varphi k_B T \sum_{p=1}^{N_\mathrm{S}} \frac{1}{\tau_{\mathrm{S},p}^{-1} + \mathrm{i}\omega}\,. \tag{5.23}$$

The left-hand side of (5.19) is (up to a factor of $\sqrt{2\pi}$) an inverse Fourier transformation, the result of which is[31] (see also Appendix B.2)

$$\begin{aligned}\int_{\omega=-\infty}^{\infty} \frac{G^*(\omega)\exp(\mathrm{i}\omega t)}{\mathrm{i}\omega}\,\mathrm{d}\,\omega &= \sqrt{2\pi}\mathcal{F}_\omega^{-1}\left\{\frac{G^*(\omega)}{\mathrm{i}\omega}\right\}(t)\\ &= 2\pi\eta\delta(t) + \varphi k_B T\sum_{p=1}^{N_\mathrm{S}} 2\pi\exp\left(-\frac{t}{\tau_{\mathrm{S},p}}\right)\Theta(t)\,.\end{aligned} \tag{5.24}$$

Comparison with the final result of (5.19) yields

$$G(t)\,\Theta(t) = \eta\delta(t) + \varphi k_B T\sum_{p=1}^{N_\mathrm{S}} \exp\left(-\frac{t}{\tau_{\mathrm{S},p}}\right)\Theta(t)\,. \tag{5.25}$$

Since values [of $G(t)$] for $t<0$ do not enter in the Laplace transform

$$\hat{G}(s) = \int_{t=0}^{\infty} G(t)\exp(-st)\,\mathrm{d}\,t\,, \tag{5.26}$$

the Heaviside function [$\Theta(t)$] can be replaced by unity in equation (5.25). The Laplace transform is then computed to be[32,33]

$$\hat{G}(s) = \eta + \varphi k_B T\sum_{p=1}^{N_\mathrm{S}} \frac{1}{\tau_{\mathrm{S},p}^{-1}+s}\,. \tag{5.27}$$

Toneian, "Multi-Particle Collision Dynamics Simulation of Viscoelastic Fluids", Footnote/citation numbers, references to sections and equations, and some mathematical symbols have been adapted. Sections in square brackets have been added or adapted for improved clarity.

5.5 Velocity Autocorrelation in Fourier Space: $\tilde{C}_{\mathrm{v}}^{\mathrm{T}}(\mathbf{k},t)$

The linearized Navier-Stokes equation for linearly viscoelastic fluids (4.54) reads, in the absence of external forces ($\mathbf{f}^{\mathrm{ext}}=0$),

$$\varrho\partial_t v_i(\mathbf{r},t) = -\partial_i p(\mathbf{r},t) + \int_{t'=-\infty}^{t} G(t-t')\,\partial_j\partial_j v_i(\mathbf{r},t')\,\mathrm{d}\,t'\,. \tag{5.28}$$

In order to make the mathematical treatment easier later on, let the lower integration bound be changed to 0:[34]

$$\varrho\partial_t v_i(\mathbf{r},t) = -\partial_i p(\mathbf{r},t) + \int_{t'=0}^{t} G(t-t')\,\partial_j\partial_j v_i(\mathbf{r},t')\,\mathrm{d}\,t' \tag{5.29}$$

This [assumption is justified for] a system which is in equilibrium at times $t \leq 0$. For other systems, this altered equation is only an approximation, the quality of which depends on t and on how fast $G(\Delta t)$ decays with Δt. However, arbitrarily small errors can be [achieved] with sufficiently large t, since $G(\Delta t)$ tends to 0 monotonically with $[\Delta t \to 0]$ (cf. Section 4.2.2).

The spatial Fourier transform $\mathbf{r} \to \mathbf{k}$ [of Eq. (5.29)] then leads to (cf. Appendix B.1)

$$\varrho\partial_t \tilde{v}_i(\mathbf{k},t) = -\mathrm{i}k_i\tilde{p}(\mathbf{k},t) - k_j k_j \int_{t'=0}^{t} G(t-t')\,\tilde{v}_i(\mathbf{k},t')\,\mathrm{d}\,t'\,, \tag{5.30}$$

[31] F. Oberhettinger. *Tables of Fourier Transforms and Fourier Transforms of Distributions.* Springer, 1990. Rule III.3.42.

[32] P. Dyke. *An Introduction to Laplace Transforms and Fourier Series.* Ed. by M. A. J. Chaplain, K. Erdmann, A. MacIntyre, E. Süli, M. R. Tehranchi, and J. F. Toland. 2nd ed. Springer Undergraduate Mathematics Series. Springer, 2014. Chapter 2.6.

[33] F. Oberhettinger and L. Badii. *Tables of Laplace Transforms.* Springer, 1973. Rule I.5.1.

where the tilde denotes a Fourier-transformed quantity (see Appendix A).

Let $\tilde{\mathbf{v}}$ be uniquely decomposed into a longitudinal part $\tilde{\mathbf{v}}^{\mathrm{L}}$ parallel to $\mathbf{k}$ and a transverse part $\tilde{\mathbf{v}}^{\mathrm{T}}$ perpendicular to $\mathbf{k}$ for a fixed $\mathbf{k}$, i.e. $\tilde{\mathbf{v}} = \tilde{\mathbf{v}}^{\mathrm{L}} + \tilde{\mathbf{v}}^{\mathrm{T}}$. Then, one can perform a projection of the vectors occurring in (5.30) onto the subspace perpendicular to $\mathbf{k}$ to obtain

$$\varrho \partial_t \tilde{v}_i^{\mathrm{T}}(\mathbf{k}, t) = -k^2 \int_{t'=0}^{t} G(t - t')\, \tilde{v}_i^{\mathrm{T}}(\mathbf{k}, t')\, \mathrm{d}\, t' \,. \tag{5.31}$$

Multiplication with the t-independent term $\tilde{v}_i^{\mathrm{T}}(-\mathbf{k}, 0)$ and summation over the repeated index i yields

$$\varrho \partial_t \tilde{v}_i^{\mathrm{T}}(\mathbf{k}, t)\, \tilde{v}_i^{\mathrm{T}}(-\mathbf{k}, 0) = -k^2 \int_{t'=0}^{t} G(t - t')\, \tilde{v}_i^{\mathrm{T}}(\mathbf{k}, t')\, \tilde{v}_i^{\mathrm{T}}(-\mathbf{k}, 0)\, \mathrm{d}\, t' \,. \tag{5.32}$$

Defining the velocity autocorrelation function in the Fourier subspace perpendicular to $\mathbf{k}$ as

$$\tilde{C}_{\mathrm{v}}^{\mathrm{T}}(\mathbf{k}, t) := \left\langle \tilde{\mathbf{v}}^{\mathrm{T}}(\mathbf{k}, t) \cdot \tilde{\mathbf{v}}^{\mathrm{T}}(-\mathbf{k}, 0) \right\rangle \,, \tag{5.33}$$

where the angle brackets denote statistical averaging over the stochastic value of $\tilde{\mathbf{v}}^{\mathrm{T}}(\mathbf{k}, t) \cdot \tilde{\mathbf{v}}^{\mathrm{T}}(-\mathbf{k}, 0)$, one can calculate the ensemble average on both sides of equation (5.32) to obtain the equation governing the temporal evolution of $\tilde{C}_{\mathrm{v}}^{\mathrm{T}}(\mathbf{k}, t)$:

$$\varrho \partial_t \tilde{C}_{\mathrm{v}}^{\mathrm{T}}(\mathbf{k}, t) = -k^2 \int_{t'=0}^{t} G(t - t')\, \tilde{C}_{\mathrm{v}}^{\mathrm{T}}(\mathbf{k}, t')\, \mathrm{d}\, t' \,. \tag{5.34}$$

Due to the [modified] lower integration bound being 0, this equation can conveniently be subjected to a Laplace transform $t \to s$ (denoted by the decoration of a symbol with a hat) to arrive at an algebraic equation for $\hat{\tilde{C}}_{\mathrm{v}}^{\mathrm{T}}$ (cf. Appendices C.1 and C.2),

$$\varrho \left(s \hat{\tilde{C}}_{\mathrm{v}}^{\mathrm{T}}(\mathbf{k}, s) - \tilde{C}_{\mathrm{v}}^{\mathrm{T}}(\mathbf{k}, 0) \right) = -k^2 \hat{G}(s)\, \hat{\tilde{C}}_{\mathrm{v}}^{\mathrm{T}}(\mathbf{k}, s) \,, \tag{5.35}$$

which can be rearranged to yield

$$\hat{\tilde{C}}_{\mathrm{v}}^{\mathrm{T}}(\mathbf{k}, s) = \frac{\varrho \tilde{C}_{\mathrm{v}}^{\mathrm{T}}(\mathbf{k}, 0)}{\varrho s + k^2 \hat{G}(s)} \,. \tag{5.36}$$

Toneian, "Multi-Particle Collision Dynamics Simulation of Viscoelastic Fluids", Footnote/citation numbers, references to sections and equations, and some mathematical symbols have been adapted. Sections in square brackets have been added or adapted for improved clarity.

For the Rouse model, one can insert Eq. (5.27) into Eq. (5.36) to obtain[35]

$$\hat{\tilde{C}}_{\mathrm{v}}^{\mathrm{T}}(\mathbf{k},s)=\frac{\varrho\tilde{C}_{\mathrm{v}}^{\mathrm{T}}(\mathbf{k},0)}{\varrho s+k^2\left(\eta+\varphi k_BT\sum_{p=1}^{N_{\mathrm{S}}}\left(\tau_{\mathrm{S},p}^{-1}+s\right)^{-1}\right)}\,. \tag{5.37}$$

5.5.1 $\tilde{C}_{\mathrm{v}}^{\mathrm{T}}(\mathbf{k},t)$ for Simple Fluids, $N_{\mathrm{S}}=0$[36]

The case of $N_{\mathrm{S}}=0$, i.e. the degenerate case of "polymers" consisting of only one monomer each, corresponds to the classic MPCD method, where the fluid particles propagate independently from one another during the streaming step (cf. Section 6.1). The sum in Eq. (5.37) then runs over an empty index set, leaving one with

$$\hat{\tilde{C}}_{\mathrm{v}}^{\mathrm{T}}(\mathbf{k},s)=\frac{\tilde{C}_{\mathrm{v}}^{\mathrm{T}}(\mathbf{k},0)}{s+k^2\eta\varrho^{-1}}\,. \tag{5.38}$$

An inverse Laplace transformation $s\to t$ yields[37]

$$\tilde{C}_{\mathrm{v}}^{\mathrm{T}}(\mathbf{k},t)=\tilde{C}_{\mathrm{v}}^{\mathrm{T}}(\mathbf{k},0)\exp\left(-\frac{k^2\eta}{\varrho}t\right)\,, \tag{5.39}$$

which reflects the exponential decay in time that is characteristic of simple fluids. Measurements of $\tilde{C}_{\mathrm{v}}^{\mathrm{T}}(\mathbf{k},t)$ can thus be used to determine the kinematic viscosity $\nu=\eta/\varrho$.

Comparison of the general expression Eq. (5.36) with Eq. (5.38) reveals that for simple fluids,

$$\hat{G}(s)=\eta \tag{5.40}$$

must hold. Likewise, the expression for the stress tensor in the linearly viscoelastic case, Eq. (4.49), has to reduce to the one arrived at for general incompressible fluids, Eq. (4.45).

[34] J. Farago, H. Meyer, J. Baschnagel, and A. N. Semenov. "Mode-coupling approach to polymer diffusion in an unentangled melt. II. The effect of viscoelastic hydrodynamic interactions". *Physical Review E* **85** (2012), 051807. Equation (27).

[35] Toneian, "Multi-Particle Collision Dynamics Simulation of Viscoelastic Fluids".

[36] Toneian, "Multi-Particle Collision Dynamics Simulation of Viscoelastic Fluids".

[37] Oberhettinger and Badii, *Tables of Laplace Transforms*, Rule II.2.2.

This is achieved by

$$G(t-t') = \eta\delta(t-t'), \tag{5.41}$$

where the Dirac delta function $\delta(t-t')$ manifestly expresses the fact that for simple fluids, "the stress tensor depends only on the instantaneous value of the shear rate, but not its history."[38] Of course, a Laplace transform of $G(t-t') = \eta\delta(t-t')$ yields the expression identified above, $\hat{G}(s) = \eta$, as is required for consistency.

Fig. 5.7 shows the excellent agreement of $\tilde{C}_{\mathrm{v}}^{\mathrm{T}}(\mathbf{k}, t)$ obtained in the simulations for $N_{\mathrm{S}} = 0$ with the theoretical prediction Eq. (5.39) for correlation times $t \lesssim 50$. For larger times, the reliability of the data measured diminishes, due to a decrease in the correlation function by more than an order of magnitude, to a level where the limited statistics causes significant deviations. Not only do the data now disagree with the prediction of exponential decay, but additionally, the data for Fourier vectors of identical magnitude, but along different directions, are in disagreement with one another, a phenomenon that clashes with the fact that the simulation algorithm does not distinguish between the three Cartesian axes. For discrepancies due to limited statistics, however, it is to be expected that the random noise would affect some curves stronger than others, purely by chance.

From Fig. 5.8, one can see that deviations from the theoretical predictions occur at smaller correlation times t the larger the magnitude k of the Fourier vector $\mathbf{k}$. This feature is due to larger Fourier vectors probing smaller structures in real space, where randomness is not as readily averaged out.

As will become apparent in what follows, the same sources of statistical errors will occur for proper polymers, where $N_{\mathrm{S}} \neq 0$.

[38] Toneian, "Multi-Particle Collision Dynamics Simulation of Viscoelastic Fluids".

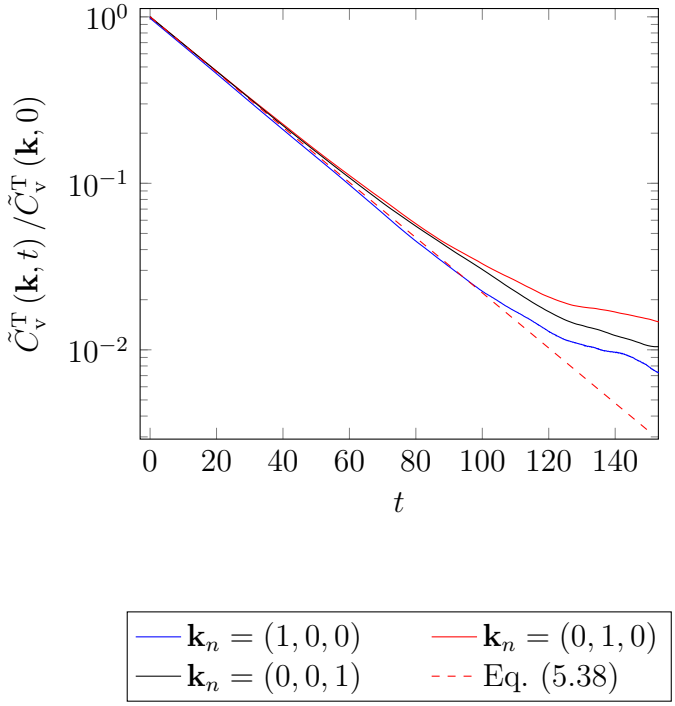

Figure 5.7: Normalized velocity autocorrelation function in $\mathbf{k}$-transverse Fourier space, $\tilde{C}_{\mathrm{v}}^{\mathrm{T}}(\mathbf{k}, t) / \tilde{C}_{\mathrm{v}}^{\mathrm{T}}(\mathbf{k}, 0)$, as a function of time t (cf. Eq. (5.39)). The vector $\mathbf{k}_n$ is related to $\mathbf{k}$ via $k_i = 2\pi k_{n,i}/L$, L being the length of the cubic simulation volume, and $|\mathbf{k}_n| = 1$ for all curves shown. Simulation data have been collected over about $7.5 \cdot 10^7$ simulation steps.

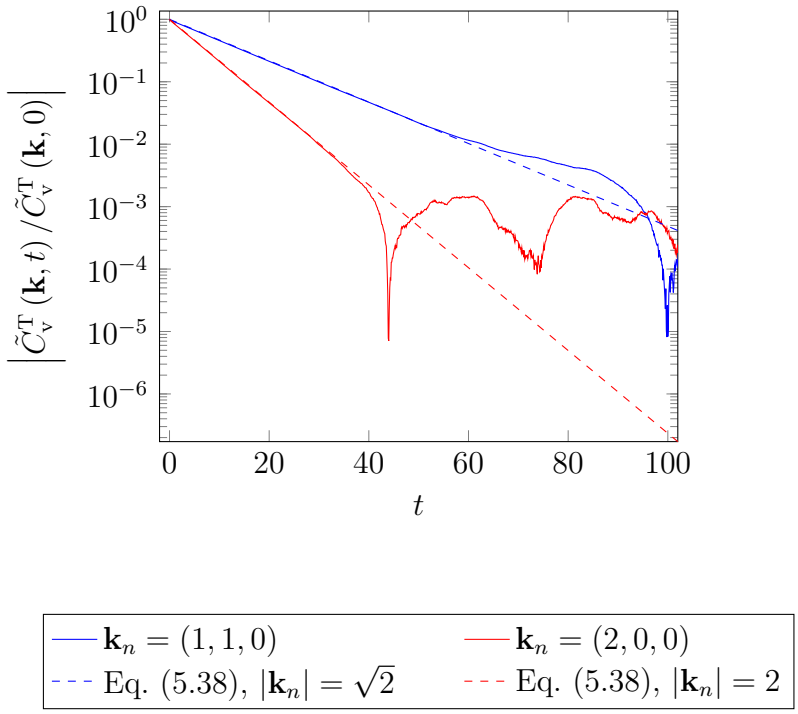

Figure 5.8: As in Fig. 5.7, but with values for $\mathbf{k}_n$ such that $|\mathbf{k}_n| > 1$ (as labeled), and with the vertical axis showing *absolute* values of $\tilde{C}_{\mathrm{v}}^{\mathrm{T}}(\mathbf{k},t)/\tilde{C}_{\mathrm{v}}^{\mathrm{T}}(\mathbf{k},0)$. The spike of the red curve ($\mathbf{k}_n = (2,0,0)$) at $t \approx 45$ corresponds to a change of sign of $\tilde{C}_{\mathrm{v}}^{\mathrm{T}}(\mathbf{k},t)/\tilde{C}_{\mathrm{v}}^{\mathrm{T}}(\mathbf{k},0)$ from positive to negative. The data gathered deviate from the theoretical curve for smaller t as $|\mathbf{k}_n|$ grows.

5.5.2 $\tilde{C}_{\mathrm{v}}^{\mathrm{T}}(\mathbf{k},t)$ for Rouse Polymers, $N_{\mathrm{S}} \neq 0$

In order to compute the inverse Laplace transform $\tilde{C}_{\mathrm{v}}^{\mathrm{T}}(\mathbf{k},t)$ of $\hat{\tilde{C}}_{\mathrm{v}}^{\mathrm{T}}(\mathbf{k},s)$, as given in Eq. (5.36), let the denominator of the right-hand side,

$$D(s) := \varrho s + k^2 \left(\eta + \varphi k_{\mathrm{B}} T \sum_{p=1}^{N_{\mathrm{S}}} \left(s + \tau_{\mathrm{S},p}^{-1} \right)^{-1} \right), \tag{5.42}$$

be multiplied by $W(s) := \prod_{p=1}^{N_{\mathrm{S}}} \left(\tau_{\mathrm{S},p}^{-1} + s \right)$, yielding

$$P(s) := D(s) W(s) = \left(\varrho s + k^2 \eta \right) W(s) + k^2 \varphi k_{\mathrm{B}} T \sum_{n=1}^{N_{\mathrm{S}}} \prod_{\substack{p=1 \\ p \neq n}}^{N_{\mathrm{S}}} \left(\tau_{\mathrm{S},p}^{-1} + s \right), \tag{5.43}$$

which is a polynomial in s of degree $N_{\mathrm{S}} + 1$.[39]

Let P_n, $n = 1, \ldots, M$, be the M distinct roots of $\varrho^{-1} P(s)$, each of multiplicity M_n, so that $\sum_{n=1}^{M} M_n = N_{\mathrm{S}} + 1$. Then, one can write $P(s) = \varrho \prod_{m=1}^{M} (s - P_m)^{M_m}$. For $W(s)$, which is also a polynomial in s, let W_n be the coefficients of s^n, so that $W(s) = \sum_{m=0}^{N_{\mathrm{S}}} W_n s^n$.

Then, Eq. (5.37) can be written as

$$\hat{\tilde{C}}_{\mathrm{v}}^{\mathrm{T}}(\mathbf{k},s) = \varrho \tilde{C}_{\mathrm{v}}^{\mathrm{T}}(\mathbf{k},0) \frac{W(s)}{P(s)} = \tilde{C}_{\mathrm{v}}^{\mathrm{T}}(\mathbf{k},0) \sum_{n=0}^{N_{\mathrm{S}}} W_n \frac{s^n}{\prod_{m=1}^{M} (s - P_m)^{M_m}}, \tag{5.44}$$

showing that, in essence, the inverse Laplace transform of $s^n \prod_{m=1}^{M} (s - P_m)^{-M_m}$ has to be found. Using Laplace transformation tables,[40,41] and noting that the degree of the enumerator's polynomial is higher than that of the denominator's, one finds

$$\begin{aligned} \tilde{C}_{\mathrm{v}}^{\mathrm{T}}(\mathbf{k},t) &= \tilde{C}_{\mathrm{v}}^{\mathrm{T}}(\mathbf{k},0) \sum_{n=0}^{N_{\mathrm{S}}} W_n \sum_{m=1}^{M} \exp(P_m t) \sum_{l=1}^{M_m} \frac{A_{nml}(P_m)\, t^{M_m - l}}{(M_m - l)!\,(l-1)!}, \\ A_{nml}(x) &:= \frac{\mathrm{d}^{l-1}}{\mathrm{d}\, x^{l-1}} \left(x^n \prod_{\substack{j=1 \\ j \neq m}}^{M} (x - P_j)^{-M_j} \right). \end{aligned} \tag{5.45}$$

[39] Toneian, "Multi-Particle Collision Dynamics Simulation of Viscoelastic Fluids".

[40] Bateman Manuscript Project. *Tables of Integral Transforms.* Ed. by A. Erdélyi. Vol. 1. McGraw-Hill, 1954, Rule 5.2.21. The rule seems to be incorrect in using $<$ instead of $\leq$, as comparison with Rule 5.2.20 therein, or with Rule 2.1.4.8 in Prudnikov et al. below, suggests.

[41] A. P. Prudnikov, Y. A. Brychkov, and O. I. Marichev. *Integrals and Series. Inverse Laplace Transforms.* Vol. 5. Gordon and Breach Science Publishers, 1992, Rule 2.1.4.8.

In the cases where $P(s)$ only has simple roots, i.e. if $M_n = 1$ for all n, the result simplifies to[42,43,44]

$$\tilde{C}_{\mathrm{v}}^{\mathrm{T}}(\mathbf{k},t) = \tilde{C}_{\mathrm{v}}^{\mathrm{T}}(\mathbf{k},0) \sum_{n=0}^{N_{\mathrm{S}}} W_n \sum_{m=1}^{N_{\mathrm{S}}+1} P_m^n \exp(P_m t) \prod_{\substack{j=1 \\ j\neq m}}^{N_{\mathrm{S}}+1} (P_m - P_j)^{-1}. \tag{5.46}$$

$\tilde{C}_{\mathrm{v}}^{\mathrm{T}}(\mathbf{k},t)$ for Rouse Dimers, $N_{\mathbf{S}} = 1$[45]

In the simplest case of a proper polymer, i.e. for dimers, $N_{\mathrm{S}} = 1$, there is only one stress relaxation time, $\tau_{\mathrm{S},1}$, which can be computed from Eq. (5.15) to be

$$\tau_{\mathrm{S},p} = \frac{\zeta_{\mathrm{B}} b^2}{12 k_{\mathrm{B}} T}. \tag{5.47}$$

With the storage and loss moduli, Eq. (5.13) and Eq. (5.14), reducing to

$$G'(\omega) = \varphi k_{\mathrm{B}} T \frac{\omega^2 \tau_{\mathrm{S},1}^2}{1 + \omega^2 \tau_{\mathrm{S},1}^2}, \tag{5.48}$$

$$G''(\omega) = \omega\eta + \varphi k_{\mathrm{B}} T \frac{\omega \tau_{\mathrm{S},1}}{1 + \omega^2 \tau_{\mathrm{S},1}^2}, \tag{5.49}$$

one finds

$$\hat{G}(s) = \eta + \varphi k_B T \frac{1}{\tau_{\mathrm{S},1}^{-1} + s}. \tag{5.50}$$

The polynomial $P(s)$ is given by

$$P(s) = \left(\varrho s + k^2 \eta\right)\left(\tau_{\mathrm{S},1}^{-1} + s\right) + k^2 \varphi k_B T, \tag{5.51}$$

its two roots being

$$P_1 = p_A - \mathrm{i} p_B \tag{5.52}$$

$$P_2 = p_A + \mathrm{i} p_B \tag{5.53}$$

[42] Oberhettinger and Badii, *Tables of Laplace Transforms*, Rule II.2.78.
[43] Bateman Manuscript Project, *Tables of Integral Transforms*, Rule 5.2.20.
[44] Toneian, "Multi-Particle Collision Dynamics Simulation of Viscoelastic Fluids".
[45] Toneian, "Multi-Particle Collision Dynamics Simulation of Viscoelastic Fluids".

where

$$\begin{aligned} p_A &:= -\frac{\tau_{\mathrm{S},1}^{-1} + k^2\varrho^{-1}\eta}{2}\,, \\ p_B &:= -\mathrm{i}\sqrt{\frac{\left(\tau_{\mathrm{S},1}^{-1} + k^2\varrho^{-1}\eta\right)^2}{4} - k^2\varrho^{-1}\left(\eta\tau_{\mathrm{S},1}^{-1} + \varphi k_B T\right)}\,, \end{aligned} \tag{5.54}$$

have been defined. Note that $p_A \in \mathbb{R}_-$, and p_B is either purely real or purely imaginary.

The solution to Eq. (5.45) thus reads, if $p_B \neq 0$,

$$\frac{\tilde{C}_{\mathrm{v}}^{\mathrm{T}}(\mathbf{k},t)}{\tilde{C}_{\mathrm{v}}^{\mathrm{T}}(\mathbf{k},0)} = \frac{\exp(p_A t)}{p_B}\left(\left(\tau_{\mathrm{S},1}^{-1} + p_A\right)\sin(p_B t) + p_B\cos(p_B t)\right)\,, \tag{5.55}$$

which is a natural representation if $p_B \in \mathbb{R}_+$. Otherwise, if $p_B \notin \mathbb{R}_+$ and $p_B \neq 0$, one has $p_C := \mathrm{i}p_B \in \mathbb{R}_+$, in which case Eq. (5.55) is more naturally written as the equivalent

$$\frac{\tilde{C}_{\mathrm{v}}^{\mathrm{T}}(\mathbf{k},t)}{\tilde{C}_{\mathrm{v}}^{\mathrm{T}}(\mathbf{k},0)} = \frac{\exp(p_A t)}{p_C}\left(\left(\tau_{\mathrm{S},1}^{-1} + p_A\right)\sinh(p_C t) + p_C\cosh(p_C t)\right)\,. \tag{5.56}$$

From this relation, one can extract the asymptotic behavior of $\tilde{C}_{\mathrm{v}}^{\mathrm{T}}(\mathbf{k},t)$ for constant $\mathbf{k}$ and $t \to \infty$, namely

$$\tilde{C}_{\mathrm{v}}^{\mathrm{T}}(\mathbf{k},t) \sim \exp\left(\left(p_A + p_C\right)t\right)\,, \tag{5.57}$$

which is an exponential decay since $\mathrm{Re}\,(p_A + p_C) < 0$ for $k \neq 0$. Taylor expansion of $(p_A + p_C)$ for small k, i.e. the slowly decaying modes, yields, taking into account only the dominant contributions for large t,

$$\tilde{C}_{\mathrm{v}}^{\mathrm{T}}(\mathbf{k},t) \sim \exp\left(-k^2\varrho^{-1}\left(\eta + \varphi k_B T\tau_{\mathrm{S},1}\right)t\right)\,. \tag{5.58}$$

Comparison of this result with the result for simple fluids, Eq. (5.39), reveals that in the limit of long correlation times, the dimer fluid behaves as if it was simple, albeit with a modified dynamic viscosity, $\eta \mapsto \eta + \varphi k_B T\tau_{\mathrm{S},1}$.

The degenerate case $p_B = 0$ produces a similar asymptotic behavior,

$$\frac{\tilde{C}_{\mathrm{v}}^{\mathrm{T}}(\mathbf{k},t)}{\tilde{C}_{\mathrm{v}}^{\mathrm{T}}(\mathbf{k},0)} = \exp(p_A t)\left(1 + t\left(\tau_{\mathrm{S},1}^{-1} + p_A\right)\right)\,. \tag{5.59}$$

The corresponding data for $N_\mathrm{S} = 1$ are shown in Figs. 5.9 and 5.10 for the spring constant $K = 0.3$. As was the case for the simple fluid, the agreement for different directions of the Fourier vector is good, up until a point $t \gtrsim 100$ (for $|\mathbf{k}_n| = 1$), where deviations due to limited statistics start to occur. Fig. 5.11 demonstrates the agreement between the simulation data and the theoretical expression Eq. (5.55). The stress relaxation time $\tau_{\mathrm{S},1}$ used in the prediction has not been computed from Eq. (5.15) due to the inaccurate predictions it makes (cf. Fig. 5.15 below), but has rather been extracted from simulation data to be $\tau_{\mathrm{S},1} \approx 13.47$.

$\tilde{C}_\mathrm{v}^\mathrm{T}(\mathbf{k}, t)$ for Rouse Decamers, $N_\mathrm{S} = 9$

Longer polymers, with $N_\mathrm{S} = 9$, have been studied in simulations for various spring constants K. Fig. 5.12 shows the absolute value of the normalized autocorrelation $\tilde{C}_\mathrm{v}^\mathrm{T}(\mathbf{k}, t)/\tilde{C}_\mathrm{v}^\mathrm{T}(\mathbf{k}, 0)$ as a function of the correlation time t, for $K = 1$, with data for other spring constants shown in Fig. 5.13. Again, one can observe discrepancies between the curves for Fourier unit vectors $\mathbf{k}$ pointing along the different Cartesian axes for times greater than about 40. As before, curves for different directions of $\mathbf{k}$, but same magnitude k, should be equivalent due to isotropy, so that deviations are ascribed to statistical noise in view of the multiple orders of magnitude $\tilde{C}_\mathrm{v}^\mathrm{T}(\mathbf{k}, t)$ has dropped by $t \approx 40$.

Fig. 5.14 compares the simulation data with the general solution for $\tilde{C}_\mathrm{v}^\mathrm{T}(\mathbf{k}, t)$, Eq. (5.45). Here, slightly different values of K are shown, highlighting two features: First, that the decamer fluid $N_\mathrm{S}+1 = 10$ can exhibit a behavior that is similar to the dimer case for low spring constants (top-left panel, cf. Fig. 5.9), or similar to simple Newtonian fluids for high K (bottom-right panel, cf. Fig. 5.7), or produce entirely novel characteristics, such as the plateau developing in the range $50 \lesssim t \lesssim 100$ for $K = 1$ (top-right panel), particularly in the theory curve.

Second, Fig. 5.14 demonstrates that, also for larger polymers, the prediction Eq. (5.45) yields very satisfactory results over multiple orders of magnitude in the decay of the correlation function $\tilde{C}_\mathrm{v}^\mathrm{T}(\mathbf{k}, t)$, despite using only a single fitting parameter, $\tau_{\mathrm{S},1}$; the other $\tau_{\mathrm{S},p}$ are inferred via Eq. (5.16) from $\tau_{\mathrm{S},1}$.

[46] G. Gompper, T. Ihle, D. M. Kroll, and R. G. Winkler. *Multi-Particle Collision Dynamics: A Particle-Based Mesoscale Simulation Approach to the Hydrodynamics of Complex Fluids.* Advances in Polymer Science. Springer, 2008. Table 1.

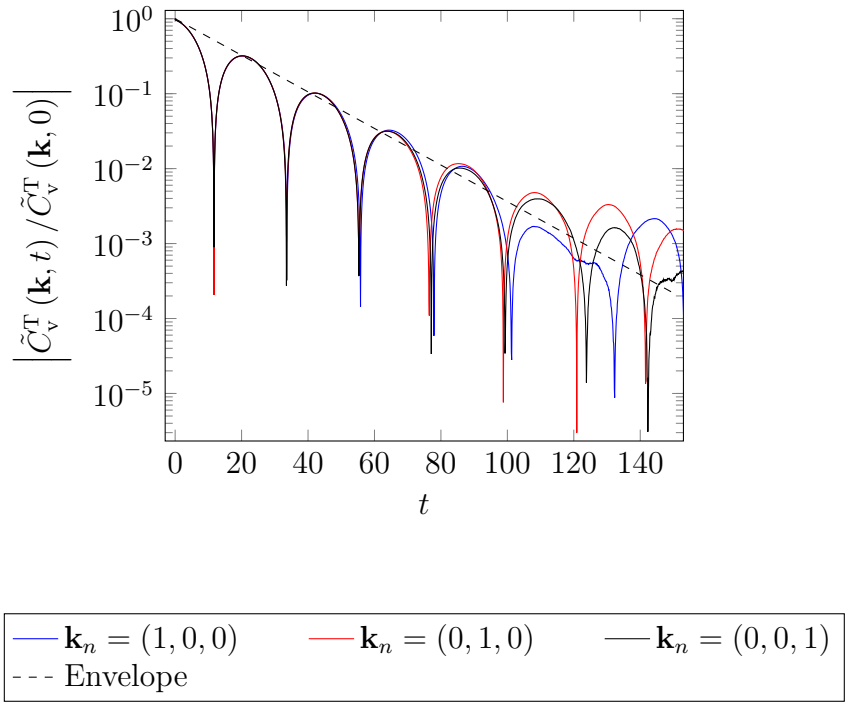

Figure 5.9: Absolute value of $\tilde{C}_{\mathrm{v}}^{\mathrm{T}}(\mathbf{k},t)$, normalized by $\tilde{C}_{\mathrm{v}}^{\mathrm{T}}(\mathbf{k},0)$, for a fluid consisting of MPCD dimers, i.e. with $N_{\mathrm{S}} = 1$ springs per polymer and a spring constant $K = 0.3$. The graph shows the dependence of $\tilde{C}_{\mathrm{v}}^{\mathrm{T}}(\mathbf{k},t)$ on the time t for various directions of the Fourier vector $\mathbf{k}$ (as labeled), with $\mathbf{k}_n$ being defined via $k_i = 2\pi k_{n,i}/L$, $L = 30$ being the side length of the cubic simulation volume. The simulation data have been collected over a period of about $1.1 \cdot 10^8$ simulation steps. The dashed curve shows the numerically evaluated prefactor ("envelope") in Eq. (5.55), i.e. $\exp(p_A t)$, with $k^2 = (2\pi/L)^2 = (2\pi/30)^2$, $\varrho = 10$, and $\eta = \varrho\nu \approx 8.705$ derived from theory.[46] The first stress relaxation time $\tau_{\mathrm{S},1} \approx 13.47$ required in this model has been fitted to all available data with $|\mathbf{k}_n| = 1$, with the fit restricted to the data in the interval $0 \leq t \leq 60$; the upper bound has been automatically chosen from a discrete set of candidates such that the error estimate on the fit parameter is minimal.

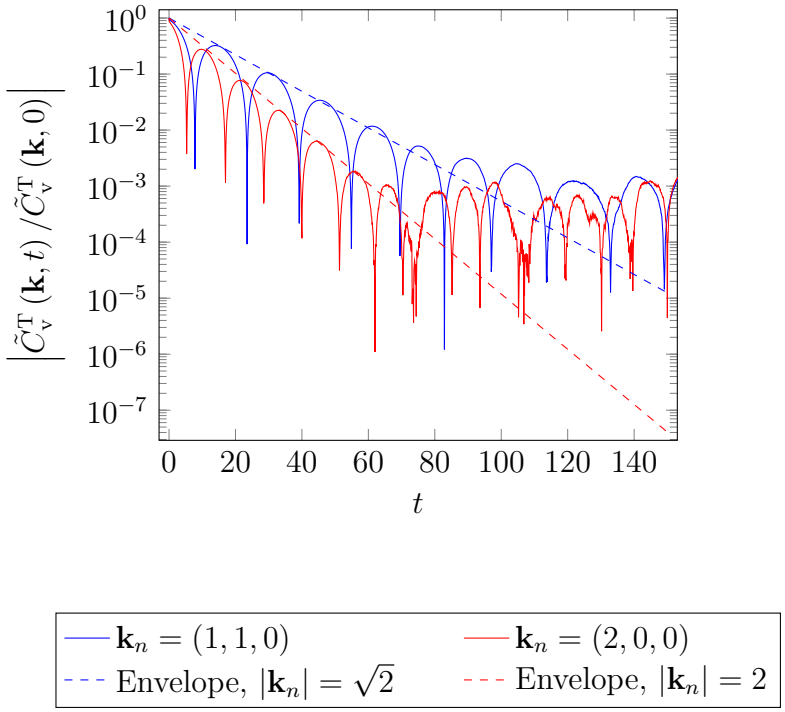

Figure 5.10: As in Fig. 5.9, except that data and envelopes for $\mathbf{k}_n$ with $|\mathbf{k}_n| \neq 1$ are shown.

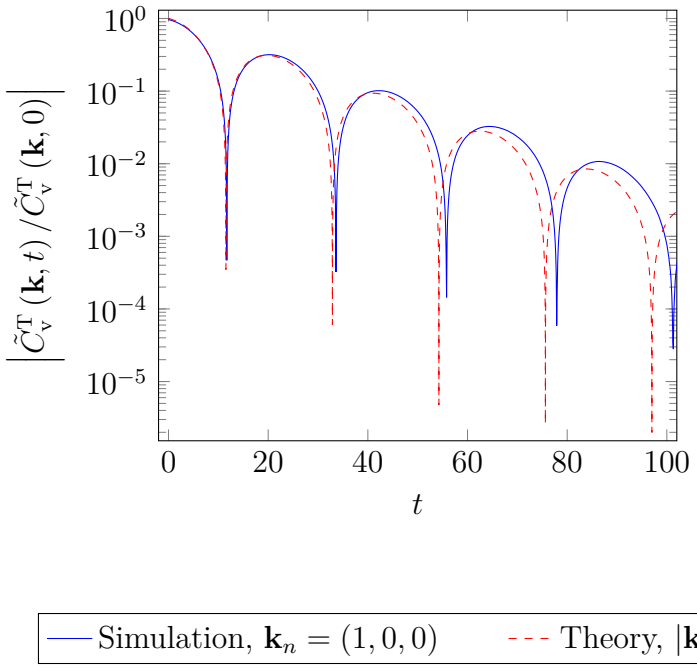

Figure 5.11: The same data as in Fig. 5.9, with the addition of the dashed curve computed from Eq. (5.55). The parameters for the latter are as specified in the caption of Fig. 5.9, and $\varphi = \varrho/(N_{\mathrm{S}}+1) = 5$.

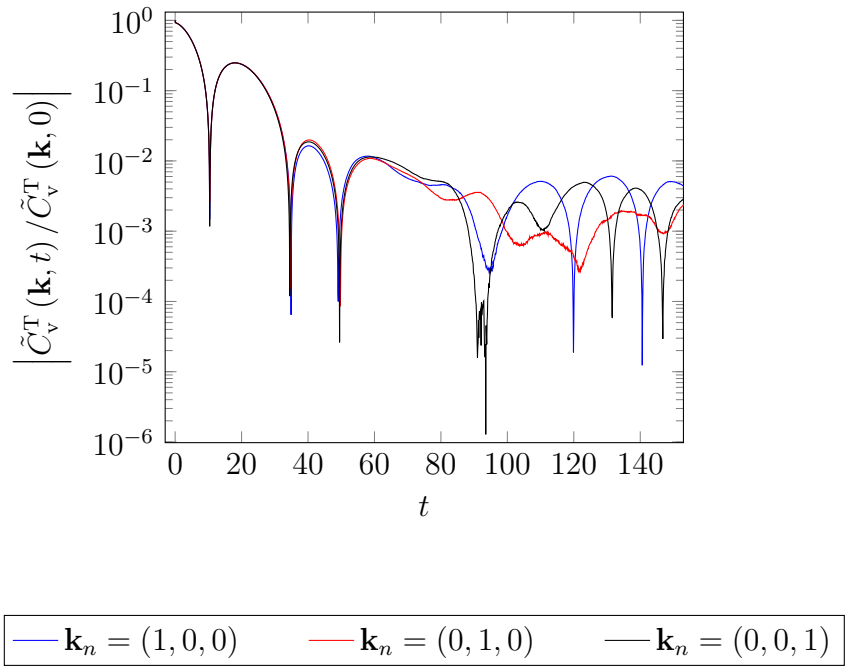

Figure 5.12: Simulation data of the absolute value of $\tilde{C}_{\mathrm{v}}^{\mathrm{T}}(\mathbf{k}, t)/\tilde{C}_{\mathrm{v}}^{\mathrm{T}}(\mathbf{k}, 0)$ for an MPCD fluid consisting of polymers with 10 monomers each (i.e. $N_{\mathrm{S}} = 9$), with spring constant $K = 1$. As before, $\mathbf{k}_n$ is defined via $k_i = 2\pi k_{n,i}/L$. The simulation data are collected over approximately $3.7 \cdot 10^7$ simulation steps.

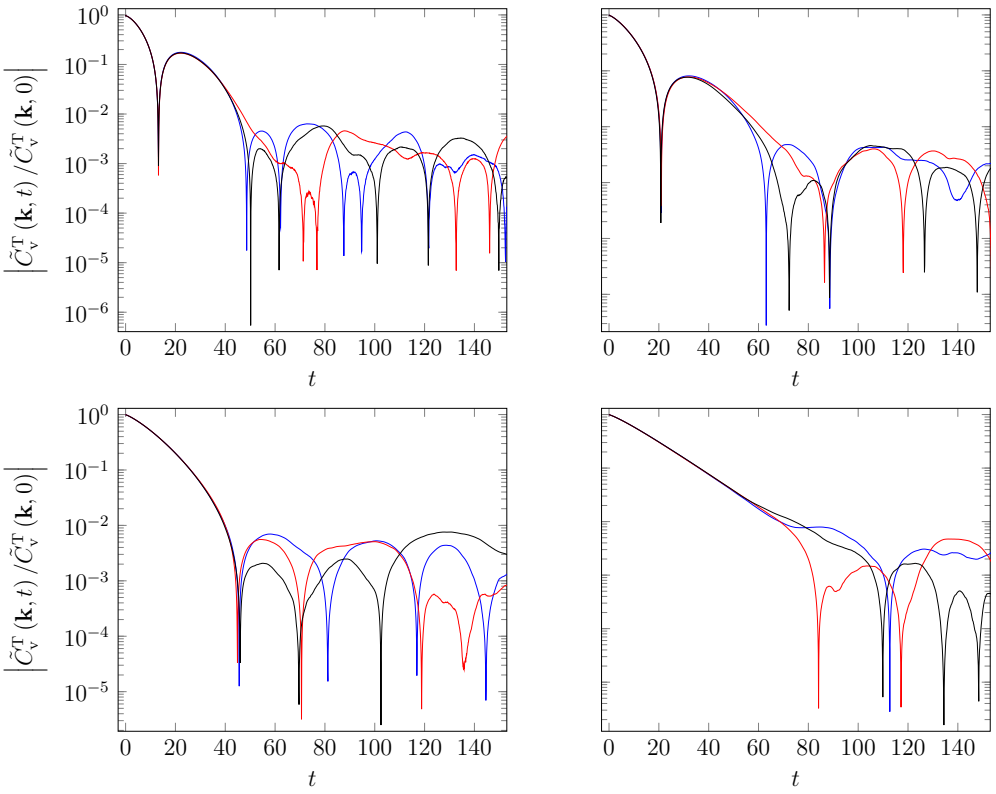

Figure 5.13: Normalized $\tilde{C}_{\mathrm{v}}^{\mathrm{T}}(\mathbf{k},t)$ as a function of the correlation time t, for $N_{\mathrm{S}} = 9$ and spring constants $K = 2$ (top-left), $K = 5$ (top-right), $K = 10$ (bottom-left), and $K = 15$ (bottom-right), with $\mathbf{k}_n$ defined as before: ——: $\mathbf{k}_n = (1,0,0)$, ——: $\mathbf{k}_n = (0,1,0)$, ——: $\mathbf{k}_n = (0,0,1)$.

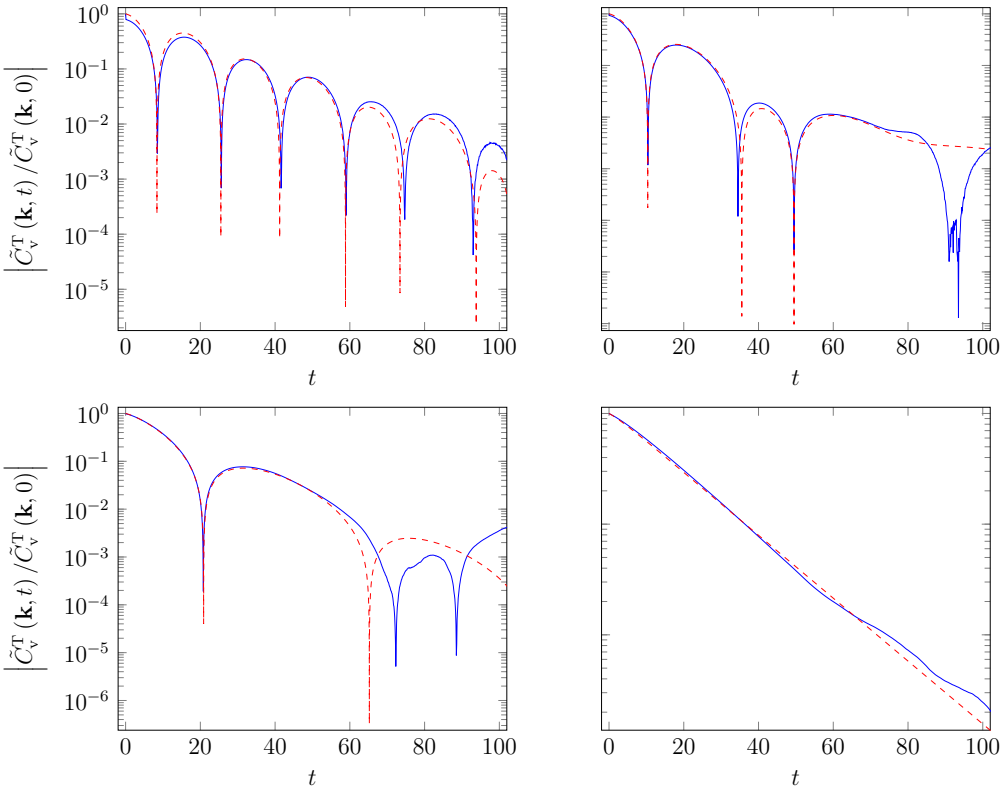

Figure 5.14: Comparison of simulation data (——) and theory (- - -, Eq. (5.45)) for $\tilde{C}_{\mathrm{v}}^{\mathrm{T}}(\mathbf{k},t)$, as a function of time t, with spring constants $K = 0.3$ (top-left), $K = 1$ (top-right), $K = 5$ (bottom-left), and $K = 15$ (bottom-right). With input parameters $k^2 = (2\pi/L)^2 = (2\pi/30)^2$, $\varrho = 10$, $\varphi = \varrho/(N_{\mathrm{S}}+1) = 5$, and $\eta = \varrho\nu \approx 8.705$, the first stress relaxation times $\tau_{\mathrm{S},1}$ have been found via a least-squares fit to be $\tau_{\mathrm{S},1} \approx 254.68$ ($K = 0.3$), $\tau_{\mathrm{S},1} \approx 86.73$ ($K = 1$), $\tau_{\mathrm{S},1} \approx 15.04$ ($K = 5$), and $\tau_{\mathrm{S},1} \approx 3.26$ ($K = 15$). The other stress relaxation times $\tau_{\mathrm{S},j}$, $1 < j \leq N_{\mathrm{S}}$ have been computed via Eq. (5.16).

Since the first polymer stress relaxation time $\tau_{\mathrm{S},1}$ can be extracted via a least-squares fit from measured autocorrelation data $\tilde{C}_{\mathrm{v}}^{\mathrm{T}}(\mathbf{k}, t)$, one can compare the N_{S}- and K-dependences of the thusly obtained values with the Rouse theory predictions, Eq. (5.15). The results, shown in Fig. 5.15, demonstrate very good agreement throughout the considered K range for dimers, $N_{\mathrm{S}} = 1$. For higher degrees of polymerization, $N_{\mathrm{S}} = 9$, the theory describes the qualitative behavior quite satisfactorily, but overestimates the stress relaxation times $\tau_{\mathrm{S},1}$ when the bead friction coefficient ζ_{B} entering Eq. (5.15) is computed from theory, $\zeta_{\mathrm{B}} \approx 19.454$ (cf. Section 5.2).

This overestimation of $\tau_{\mathrm{S},1}$ is equivalent to an overestimation of ζ_{B}, or alternatively (or additionally), to an underestimation of the diffusion coefficient. While the former possibility is unlikely in view of the results of Section 5.3 – unless Eq. (5.3) or Eq. (5.12) should be violated –, the possibility of an underestimation of the diffusion coefficient has been demonstrated to be realized in Fig. 5.2. Why only some of the closely linked quantities $\tau_{\mathrm{S},1}$, $\tau_{\mathrm{X},1}$, ζ_{B}, and D_{cm} (cf. Section 5.2 and Eqs. (5.12) and (5.15)) should described well by the theory, while predictions for others deviate substantially from data, remains unclear at the moment. Nevertheless, it is noteworthy that Eq. (5.15) produces considerably better results after adjusting the bead friction coefficient's assumed value.

Finally, Fig. 5.16 show simulation data for polymers with $N_{\mathrm{S}} + 1 = 100$ monomers; unfortunately, evaluating Eq. (5.45) has been numerically prohibitive. Also, long polymers are costly in terms of simulation time, since a substantial increase in the simulation volume (and hence, a cubic increase both in volume and in the number of particles) is necessary to avoid self-interaction of the long polymers, so that polymers of high degree of polymerization (i.e. large N_{S}) could not be included in the analysis above.

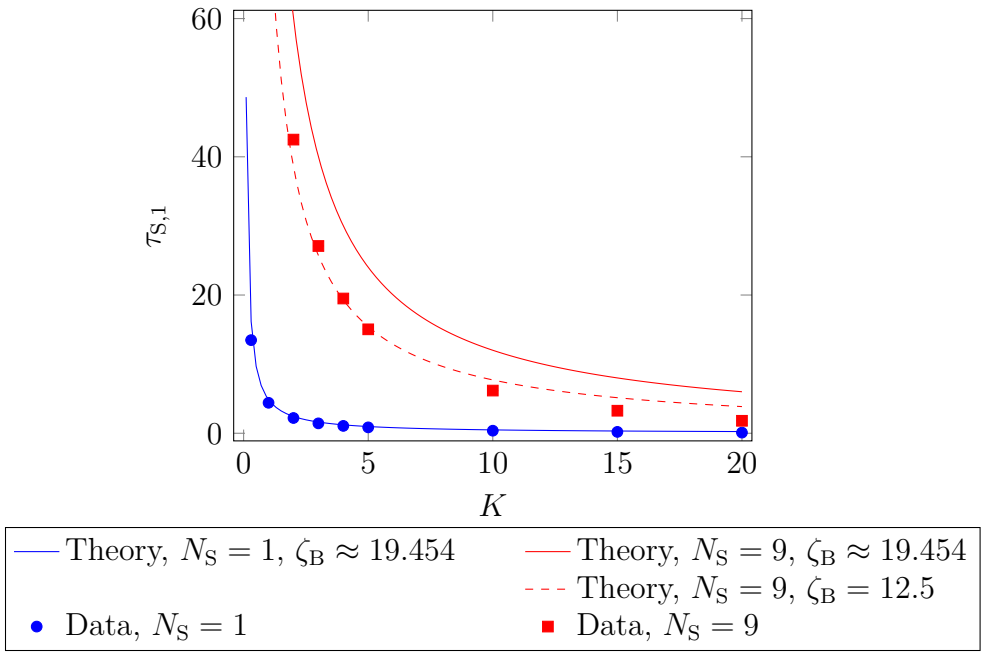

Figure 5.15: First stress relaxation times, $\tau_{S,1}$, as obtained through least-square fits from $\tilde{C}_{\mathrm{v}}^{\mathrm{T}}(\mathbf{k},t)$ data (symbols), compared to the Rouse model prediction Eq. (5.15). Solid lines are obtained by using the bead friction coefficient calculated from theory, $\zeta_B \approx 19.454$, while the dashed line uses a reduced friction coefficient, $\zeta_B = 12.5$, chosen such that the fit of the data to the functional form of Eq. (5.15) is improved.

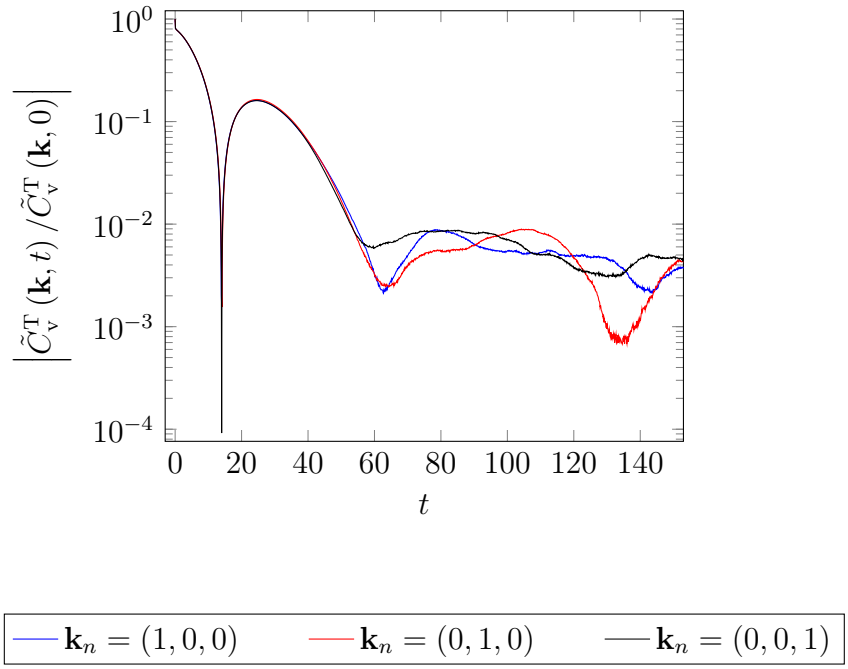

Figure 5.16: Simulation data for $N_{\mathrm{S}} = 99$ and $K = 3$, but with a larger simulation volume of $L = 100$ to avoid self-interaction of the long polymers via periodic images.

5.6 Conclusions and Outlook

The generalized MPCD simulation method developed in this part of the thesis, where individual MPCD particles are linked via harmonic potentials into linear polymers with N_S springs each, is shown to be well-described by the theoretical framework presented: Individual polymers are treated as in the Rouse model, and on the level of continuum hydrodynamics, an ansatz of linear viscoelasticity is made.

There is excellent agreement between theory and simulation regarding the relationship of the spring constant K and the mean squared spring length b^2 (cf. Section 5.1). Similarly, the normal mode analysis in Section 5.3 produces outstanding results, without relying on any parameters derived from simulations; in particular, the normal mode autocorrelation times $\tau_{\mathrm{X},p}$ agree to a remarkable degree with simulation data.

While the polymers' centers of mass follow the expected diffusion laws, i.e. the mean square displacement is a linear function of time, the diffusion coefficient is systematically underestimated by the theory predictions for the friction coefficient (cf. Section 5.2).

This mismatch seems to be related to the overestimation of the stress relaxation times $\tau_{\mathrm{S},p}$ (Fig. 5.15). This observation warrants further investigation, particularly because it suggests that the relationship Eq. (5.12) between normal mode autocorrelation times and stress relaxation times does not hold in this system.

Lastly, the analytic solution for the Fourier-space velocity autocorrelation function $\tilde{C}_\mathrm{v}^\mathrm{T}(\mathbf{k}, t)$ is derived in Section 5.5 and shown to reproduce data to a high degree of accuracy for a variety of polymer parameters, given that one fits the first stress relaxation time to the data.

This research establishes the presented extension of MPCD as an efficient way of simulating inherently non-Newtonian fluids that is accessible to theoretical treatment and predictions, which should greatly simplify the tuning of the viscoelastic properties of the fluid, as would be required if one wanted to model a specific experiment.

From the point of view of method development, it would be interesting to investigate the effects different choices of polymer architecture or spring potential would have on the fluid. Regarding the use of the method, the fact that existing MPCD simulations with Newtonian fluids should be able to be adapted with reasonable effort to this generalized method opens up a wide field of possible application scenarios, where non-Newtonian behavior might be found to cause significant changes in the qualitative system behavior, or where the importance of non-Newtonian behavior is already known, but neglected due to limited computational or methodological capacity.

Chapter 6

Multi-Particle Collision Dynamics (MCPD) and Molecular Dynamics (MD)

6.1 Introduction: MPCD for Simple Fluids

Multi-Particle Collision Dynamics (MPC or MPCD for short) is a class of particle-based simulation techniques, introduced by Malevantes and Kapral.[1]

It is instructional to consider first the simplest variant of an MPC system in three spatial dimensions: Let the coordinate system be Cartesian, with the axes named x, y, and z, or alternatively 1, 2, and 3, respectively. Let the primary simulation volume be a cuboid of side lengths $L_i = l_i a_0$, $i \in \{1, 2, 3\}$, where $l_i \in \mathbb{N}_+$. So, L_i is a positive integer multiple of a characteristic length a_0, which serves as the length scale of the system and as such is set to unity. The origin of the coordinate system is chosen such that it coincides with a corner of the primary simulation volume, and the axes are aligned such that the primary simulation volume lies entirely within the first octant of the coordinate system.

The fluid is modeled by a number $N_{\mathrm{MPCD}} \in \mathbb{N}_+$ of point-like MPC particles. Each of them is an abstract representation of a volume of the fluid that is large compared to the individual fluid molecules, but small compared to $V_{\mathrm{MPCD}} := L_1 L_2 L_3$, the volume of the simulated system. Each MPC particle $i \in \mathbb{I} := \{x \in \mathbb{N}_+ \mid x \leq N_{\mathrm{MPCD}}\}$ has a position, taking on continuous values $\mathbf{r}_i \in \mathbb{R}^3$, which, depending on the boundary conditions applied and the way these are implemented, may be further restricted to some continuous subset of $\mathbb{R}^3$. The MPC particle velocities, $\mathbf{v}_i \in \mathbb{R}^3$, are unconstrained. For simple fluids, each MPC particle has the same mass $m_i = m_{\mathrm{MPCD}}$, which is the system's reference mass and is set to 1.

The MPC algorithm then consists of two alternating phases. In the *streaming phase*, each MPC particle is propagated independently from all other particles. With the fixed propagation time being called Δt_{MPCD}, and ignoring here, for the sake of simplicity, both the possible presence of external force fields and the issue of boundary conditions (see Section 6.1.3), the streaming step thus is simply an update of the particle positions in accordance with ballistic motion:

$$\mathbf{r}_i\left(t + \Delta t_{\mathrm{MPCD}}\right) = \mathbf{r}_i\left(t\right) + \mathbf{v}_i\left(t\right) \cdot \Delta t_{\mathrm{MPCD}}\,. \tag{6.1}$$

For the subsequent *collision phase*, the primary simulation volume is partitioned into cubic *collision cells*, the side lengths of which are what defines the system's length scale a_0. The collision cells are tiled such that each point in the simulation volume can be uniquely assigned to one collision cell. Then, all MPC particles that are momentarily located within a given collision cell interact with one another (but not with any particles outside that collision cell), in a way that conserves the total mass, linear momentum, and energy contained in each individual collision cell.[2]

With these properties, the only missing ingredient essential to the derivation of the Navier-Stokes equation (cf. Section 4.1) is spatial isotropy. Since the orientation of the collision cell cubes distinguishes three directions, the system is not strictly isotropic. However, it is conventional to assume that isotropy is satisfied to a sufficient degree, such that, for suitable simulation parameters (such as the simulation time-step Δt_{MPCD}), one can expect MPC to reproduce Navier-Stokes-like behavior.[3,4,5]

6.1.1 Stochastic Rotation Dynamics (SRD)

In the initial and most common variant of MPC, called *stochastic rotation dynamics*[6] and abbreviated *SRD*, the collision rule is as follows: For each collision cell c, the largest set $\mathbb{I}_c \subseteq \mathbb{I}$ of MPC particle indices with the property that for each $i \in \mathbb{I}_c$, $\mathbf{r}_i$ lies in the collision cell c, is identified. Then, the collision cell's center-of-mass velocity

$$\mathfrak{v}_c := \frac{\sum_{i\in\mathbb{I}_c} m_i \mathbf{v}_i}{\sum_{i\in\mathbb{I}_c} m_i} \tag{6.2}$$

is calculated, where $\mathbf{v}_i$ is the i-th MPC particle velocity prior to the collision. With this, the MPC particle velocities in the center-of-mass frame of the collision cell are obtained:

$$\mathfrak{v}_i := \mathbf{v}_i - \mathfrak{v}_c \,. \tag{6.3}$$

Next, in the collision cell's center-of-mass frame, the $\mathfrak{v}_i$ are rotated by a fixed angle α_{SRD} around a randomly chosen unit vector $\mathbf{R}$; it is uniformly sampled from $\mathbb{S}_2$ (cf. Appendix E), independently so for each collision cell and time-step. Decomposing $\mathfrak{v}_i = \mathfrak{v}_i^{\perp} + \mathfrak{v}_i^{\parallel}$ uniquely into a part $\mathfrak{v}_i^{\parallel} := (\mathfrak{v}_i \cdot \mathbf{R})\,\mathbf{R}$ parallel to $\mathbf{R}$ and a part $\mathfrak{v}_i^{\perp} := \mathfrak{v}_i - \mathfrak{v}_i^{\parallel}$ perpendicular to $\mathbf{R}$, the result of the rotation of $\mathfrak{v}_i$ around $\mathbf{R}$ is[7]

$$\begin{aligned}
\mathfrak{v}_i' &:= \mathfrak{v}_i^{\parallel} + \cos(\alpha_{\mathrm{SRD}})\,\mathfrak{v}_i^{\perp} + \left|\mathfrak{v}_i^{\perp}\right| \sin(\alpha_{\mathrm{SRD}})\,\frac{\mathbf{R}\times\mathfrak{v}_i}{|\mathbf{R}\times\mathfrak{v}_i|} \\
&= \mathfrak{v}_i^{\parallel} + \cos(\alpha_{\mathrm{SRD}})\,\mathfrak{v}_i^{\perp} + \sin(\alpha_{\mathrm{SRD}})\,(\mathbf{R}\times\mathfrak{v}_i) \\
&= (\mathfrak{v}_i\cdot\mathbf{R})\,\mathbf{R} + \cos(\alpha_{\mathrm{SRD}})\,(\mathfrak{v}_i - (\mathfrak{v}_i\cdot\mathbf{R})\,\mathbf{R}) + \sin(\alpha_{\mathrm{SRD}})\,(\mathbf{R}\times\mathfrak{v}_i)\ ,
\end{aligned} \tag{6.4}$$

since $|\mathbf{R}\times\mathfrak{v}_i| = \left|\mathfrak{v}_i^{\perp}\right|$. The post-collision velocities obtained in the simulation system's frame of reference then are finally

$$\mathbf{v}_i' := \mathfrak{v}_c + \mathfrak{v}_i' \,. \tag{6.5}$$

Since the collision cell's center-of-mass frame is defined by the condition that the sum of all linear momenta in that reference frame is zero, i.e. $\sum_{i\in\mathbb{I}_c} m_i\mathfrak{v}_i = 0$, rotation of all $\mathfrak{v}_i$ around the same axis conserves the linear momentum of the entire collision cell. Also, the collision cell's mass content is conserved, so that energy is unchanged as well. Finally, since the procedure is evidently isotropic, all the conditions for an MPC collision step are satisfied (cf. Section 6.1).

It should be noted, however, that SRD violates conservation of angular momentum. While this deficiency can be repaired at the cost of computational efficiency,[8] in most simulations where MPC particles move slowly compared to the speed of sound[9] the deviation from Navier-Stokes-type behavior due to unphysical changes in angular momentum during the collision step is negligible. [10]

6.1.2 Grid Shift[11,12,13]

If one uses a fixed grid to define the collision cells, one breaks the system's symmetry under Galilei transformations: Imagine a fluid in a situation where the mean free path λ during the time-step Δt_{MPCD} is substantially smaller than the collision cell size a_0. Then, given a particular collision cell c, the set of MPC particles $\mathbb{I}_c(t)$ in that cell at time t is going to contain mostly the same members as $\mathbb{I}_c(t + \Delta t_{\mathrm{MPCD}})$, the set of MPC particles in the same collision cell c in the next time-step. Statistically, the states of the MPC particles in $\mathbb{I}_c(t)$ are therefore going to be correlated over a timespan large compared to the streaming time-step Δt_{MPCD}.

However, if one superimposes a global, fixed, and non-zero velocity $\mathbf{u}$ on the entire system, the correlation time changes in general, since now, the sets $\mathbb{I}_c(t)$ and $\mathbb{I}_c(t + \Delta t_{\mathrm{MPCD}})$ may share [fewer] members. This means that the statistical properties of a system's MPC particles depend on the observer's inertial frame, thus breaking Galilean symmetry.

In the case where λ is large compared to a_0, this effect is negligible, since then $\mathbb{I}_c(t)$ and $\mathbb{I}_c(t + \Delta t_{\mathrm{MPCD}})$ are mostly disjoint for arbitrary $\mathbf{u}$.

This deficiency of broken Galilean symmetry can be eliminated by independently sampling three random numbers X_1, X_2, and X_3 from $U\left(\left[-\frac{a_0}{2}, \frac{a_0}{2}\right]\right)$ and shifting either the entire collision cell grid by $\mathbf{X} = (X_1, X_2, X_3)$ with reference to its fixed position in the previous scenario, or equivalently, by shifting the positions of all MPC particles by $-\mathbf{X}$ (for the handling of boundary conditions see Section 6.1.3).

This grid shift does not, however, fix the broken rotational symmetry due to the grid's cubic unit cell, which distinguishes three spatial directions in the system. Like most of the literature, the present work will not deal with this issue further.

6.1.3 Boundary Conditions

The boundary conditions used in this work are *periodic boundary conditions* and *Lees-Edwards boundary conditions*, both described below. Of course, others can be used with MPC as well, such as *no-slip boundary conditions* in scenarios where extended solids, such as confining walls, are involved: there, one imposes that the velocity component tangential to the surface of the solid-fluid interface is continuous across the interface, i.e. the fluid does not slip along the solid's surface – a condition experimentally verified under certain conditions.[14] However, implementing these boundary conditions without introducing artifacts is non-trivial.[15,16]

Periodic Boundary Conditions

Periodic boundary conditions are defined by the property that, during the collision step, each MPC particle i has its position vector components $r_{i,j}$, $j \in \{1,2,3\}$, mapped to the *image coordinates*

$$r'_{i,j} := r_{i,j} + c_{i,j} L_j \,, \tag{6.6}$$

where the $c_{i,j} \in \mathbb{Z}$ are chosen such that $r'_{i,j} \in [0, L_j)$.

For the collision step, it is only these image coordinates that are of importance. However, the real MPC particle coordinates $r_{i,j}$ are not replaced by these image coordinates, so that during the streaming steps, the MPC particles effectively move in an unbounded system, that is only virtually folded back into the primary simulation volume for MPC collisions.

This procedure makes the handling of distances easier, for example when observing diffusion behavior: if one is interested in how far a certain MPC particle travels during a given time interval, one does not have to keep track of how often the primary simulation volume's boundaries have been crossed.

There is a possible downside to having the MPC particles propagate without bounds: if particles move far away from the origin, the numerical accuracy of the floating-point variables storing the positions degrades, as the density of representable real numbers decreases with increasing modulus.[17,18] However, this effect would be noticeable only for simulations running many orders of magnitude longer than what was necessary in this work.

Lees-Edwards Boundary Conditions[19,20]

Lees and Edwards[21] introduced a generalization of the periodic boundary conditions that enables one to impose a specific, possibly time-dependent, uniform shear on the simulated system.

Let the shear act in the x-y-plane in the sense that with increasing y, the mean velocity v_x along the x direction increases, and let

$$\dot{\gamma} := \frac{\mathrm{d}\, v_x}{\mathrm{d}\, r_y} \tag{6.7}$$

denote the shear rate, which is time-independent in this work.

Imagine, at the beginning of the simulation, having periodic images of the primary simulation volume along the x, y, and z directions. Label the primary simulation volume by $n_x = n_y = n_z = 0$; the image adjacent to that along the positive x direction is labeled $n_x = 1$, $n_y = n_z = 0$, and so on. Then, as the simulation time progresses, imagine the layers with y-label $n_y = 1$ moving with a constant velocity

$$u := \dot{\gamma} L_y \,, \tag{6.8}$$

with L_y being the length of the primary simulation volume along the y direction. Similarly, the $n_y = -1$ images move with $-u$ along the x direction, and in general, an image with label n_y moves with $n_y u$ along the x direction. So, after a simulation time t, the coordinates of the origins of the images are $(n_x L_x + n_y u t, n_y L_y, n_z L_z)$ with respect to the origin of the primary simulation cell.

Recall that the MPC particles are thought to propagate in unbounded space during the streaming phase, and that it is necessary to temporarily fold the MPC particle coordinates into the primary simulation volume for the collision phase. To achieve this, one first finds, for each MPC particle i, which simulation volume image it falls into, by computing

$$n_{i,j} := \left\lfloor \frac{r_{i,j}}{L_j} \right\rfloor \tag{6.9}$$

for $j \in \{1, 2, 3\}$. Then, the MPC particle's image coordinates are calculated as

$$r'_{i,j} = r_{i,j} - n_{i,j} L_j - n_{i,2} n_y u t \delta_{j,1} \,, \tag{6.10}$$

where $\delta_{i,j}$ is the Kronecker symbol. Additionally, the MPC particle's velocity along the x direction is temporarily changed to

$$v'_{i,j}(t) := \mathbf{v}_i j(t) - n_y u \delta_{j,1} \tag{6.11}$$

to account for the additional speed gained through the applied shear. Next, the MPC collision algorithm is executed with the image positions $\mathbf{r}'_i$ and image velocities $\mathbf{v}'_i$. Finally, the changed MPC particle velocities are transformed from the image in the primary simulation volume to the proper position in unbounded space, by undoing the transformation (6.11):

$$\mathbf{v}_i j(t + \Delta t_{\mathrm{MPCD}}) := v'_{i,j}(t + \Delta t_{\mathrm{MPCD}}) - n_y u \delta_{j,1}\,. \tag{6.12}$$

The Lees-Edwards boundary conditions have the periodic boundary conditions as the special case $\dot{\gamma} = 0$, as can easily be seen.

6.1.4 Maxwell-Boltzmann-Scaling Thermostat

The MPC algorithm conserves energy, and thus models a microcanonical ensemble. However, many interesting phenomena, such as the dynamics of polymers in solution, arise due to thermal fluctuations.[22] In order to introduce those fluctuations into the simulation scheme, one can employ various methods to realize a canonical ensemble where the system temperature T is fixed. Another reason one might need to couple the system to a heat bath is that, if external forces act on the MPC particles, one may introduce energy into the system that may accumulate if not removed via thermal contact.

In this work, the *Maxwell-Boltzmann-Scaling* thermostat, introduced by Huang et al.,[23] is implemented, which operates locally on the collision cells: For each collision cell c with member particle indices in $\mathbb{I}_c$, let N_c be the number of MPC particles currently being in that collision cell. If $N_c = 1$, no action is performed, since then, no change in energy can be accomplished without violating momentum conservation. In the case $N_c > 1$, a random variable E'_k is sampled from the gamma distribution (A.11), with the distribution parameters being $a = \frac{f}{2}$ and $b = k_B T$; here, $f = 3(N_c - 1)$ is the number of velocity degrees of freedom left in

the collision cell's center-of-mass frame, so that

$$E'_k \sim f_\Gamma\left(E'_k; \frac{f}{2}, k_BT\right) = \frac{1}{E'_k\Gamma\left(\frac{f}{2}\right)}\left(\frac{E'_k}{k_BT}\right)^{\frac{f}{2}} \exp\left(-\frac{E'_k}{k_BT}\right). \tag{6.13}$$

Equation (6.13) is derived from the Maxwell-Boltzmann distribution of three-dimensional velocity vectors, with the constraint of momentum conservation.

With the center-of-mass velocity of MPC particle i being $\mathfrak{v}_i$, the current center-of-mass kinetic energy

$$E_k := \frac{1}{2}m_{\mathrm{MPCD}}\sum_{i\in\mathbb{I}_c}\mathfrak{v}_i^2 \tag{6.14}$$

is calculated, a random E'_k is chosen according to equation (6.13), and the center-of-mass velocities are scaled via

$$\mathfrak{v}_i \mapsto \sqrt{\frac{E'_k}{E_k}}\mathfrak{v}_i\,, \tag{6.15}$$

with the result that after scaling, the center-of-mass kinetic energy of the collision cell c is E'_k.

Toneian, "Multi-Particle Collision Dynamics Simulation of Viscoelastic Fluids", Footnote/citation numbers, references to sections and equations, and some mathematical symbols have been adapted, as have been phrases in square brackets.

---

[1] A. Malevanets and R. Kapral. "Mesoscopic model for solvent dynamics". *The Journal of Chemical Physics* **110** (1999), 8605.

[2] Gompper, Ihle, Kroll, and Winkler, *Multi-Particle Collision Dynamics: A Particle-Based Mesoscale Simulation Approach to the Hydrodynamics of Complex Fluids*, Chapter 1.

[3] U. Frisch, B. Hasslacher, and Y. Pomeau. "Lattice-Gas Automata for the Navier-Stokes Equation". *Physical Review Letters* **56** (1986), 1505.

[4] Gompper, Ihle, Kroll, and Winkler, *Multi-Particle Collision Dynamics: A Particle-Based Mesoscale Simulation Approach to the Hydrodynamics of Complex Fluids*, Chapter 1.

[5] T. Ihle and D. M. Kroll. "Stochastic rotation dynamics. I. Formalism, Galilean invariance, and Green-Kubo relations". *Physical Review E* **67** (2003), 066705. Section I.A.

[6] T. Ihle and D. M. Kroll. "Stochastic rotation dynamics: A Galilean-invariant mesoscopic model for fluid flow". *Physical Review E* **63** (2001), 020201.

[7] D. Koks. *Explorations in Mathematical Physics*. 1st ed. Springer, 2006. Chapter 4.2.

[8] H. Noguchi, N. Kikuchi, and G. Gompper. "Particle-based mesoscale hydrodynamic techniques". *Europhysics Letters* (2007).

[9] Landau and Lifshitz, *Fluid Mechanics*, § 44.

6.2 MPCD with coupled Molecular Dynamics (MD)

MPC can easily be extended to simulate more complex systems than just fluids of one species, with applications ranging from the modeling of binary fluids to systems of biological cells and vesicles.[24]

In this work, the emphasis lies on the dynamics of linear polymers and the behavior of viscoelastic fluids. Here, polymers are represented by linking together several MPC particles by suitable potentials.

While it is easy to find an analytic solution for the streaming-step propagation of two MPC particles coupled by a harmonic potential,[25] the solutions become increasingly more complicated, or even inaccessible, as soon as one generalizes this to other interaction potentials and/or more constituents per polymer. So, instead of trying to find exact solutions in terms of closed expressions, the motion of the individual MPC particles is approximately calculated by the *velocity Verlet*

[10]Gompper, Ihle, Kroll, and Winkler, *Multi-Particle Collision Dynamics: A Particle-Based Mesoscale Simulation Approach to the Hydrodynamics of Complex Fluids*, Chapter 2.1.1.

[11]Ihle and Kroll, "Stochastic rotation dynamics: A Galilean-invariant mesoscopic model for fluid flow".

[12]Ihle and Kroll, "Stochastic rotation dynamics. I. Formalism, Galilean invariance, and Green-Kubo relations", Section A.

[13]Gompper, Ihle, Kroll, and Winkler, *Multi-Particle Collision Dynamics: A Particle-Based Mesoscale Simulation Approach to the Hydrodynamics of Complex Fluids*, Chapter 2.1.

[14]Batchelor, *An Introduction to Fluid Dynamics*, Chapter 3.3.

[15]A. Lamura, G. Gompper, T. Ihle, and D. M. Kroll. "Multi-particle collision dynamics: Flow around a circular and a square cylinder". *Europhysics Letters* **56** (2001), 319.

[16]A. Lamura and G. Gompper. "Numerical study of the flow around a cylinder using multi-particle collision dynamics". *The European Physical Journal E - Soft Matter* **9** (2002), 477.

[17]*IEEE Standard for Floating-Point Arithmetic*. Institute of Electrical and Electronics Engineers.

[18]D. Goldberg. "What every computer scientist should know about floating-point arithmetic". *ACM Computing Surveys* **23** (1991), 5.

[19]Allen and Tildesley, *Computer Simulation of Liquids*, Chapter 8.2.

[20]Kowalik and Winkler, "Multiparticle collision dynamics simulations of viscoelastic fluids: Shear-thinning Gaussian dumbbells", Appendix A.

[21]A. W. Lees and S. F. Edwards. "The computer study of transport processes under extreme conditions". *Journal of Physics C: Solid State Physics* **5** (1972), 1921.

[22]Gompper, Ihle, Kroll, and Winkler, *Multi-Particle Collision Dynamics: A Particle-Based Mesoscale Simulation Approach to the Hydrodynamics of Complex Fluids*, Chapter 1.

[23]C. Huang, A. Chatterji, G. Sutmann, G. Gompper, and R. G. Winkler. "Cell-level canonical sampling by velocity scaling for multiparticle collision dynamics simulations". *Journal of Computational Physics* **229** (2010), 168.

algorithm as follows.[26] Let $\mathbf{r}_i(t)$, $\mathbf{v}_i(t)$, and $\mathbf{a}_i(t)$ be the position, velocity, and acceleration of the i-th MPC particle at time t, respectively, and let Δt be the simulation time-step. Then, the updated positions $\mathbf{r}_i(t+\Delta t)$ are calculated as

$$\mathbf{r}_i(t+\Delta t) = \mathbf{r}_i(t) + \mathbf{v}_i(t)\,\Delta t + \frac{1}{2}\mathbf{a}_i(t)\,(\Delta t)^2 \,. \tag{6.16}$$

The updated velocities are computed via

$$\mathbf{v}_i(t+\Delta t) = \mathbf{v}_i(t) + \frac{\mathbf{a}_i(t) + \mathbf{a}_i(t+\Delta t)}{2}\Delta t \,. \tag{6.17}$$

Of course, for the accelerations $\mathbf{a}_i(t+\Delta t)$ to be available, the updated positions $\mathbf{r}_i(t+\Delta t)$ of all interaction partners have to be computed beforehand, since

$$\mathbf{a}_i(t) := -\frac{\partial}{\partial \mathbf{r}_i(t)} U(\mathbf{r}_1(t), \mathbf{r}_2(t), \ldots) \,, \tag{6.18}$$

where $U(\mathbf{r}_1(t), \mathbf{r}_2(t), \ldots)$ is the system's potential energy at time t. U evidently depends on the positions of the interacting particles, but the velocity Verlet algorithm in unsuitable if there is a dependence on the velocities; since the calculation of the updated velocities (6.17) requires knowledge of the updated accelerations, having the latter be influenced by the former would create a circular dependency.

For the velocity Verlet algorithm, being equivalent to the original Verlet algorithm,[27] an error of $(\Delta t)^4$ in the updated positions can be estimated, and an error of $(\Delta t)^2$ in the prediction of the updated velocities.[28] While velocity verlet exhibits inaccuracies in the estimation of the velocity and a violation of conservation of energy on long timescales,[29] these deficiencies are not too worrisome in SRD simulations, because first, the velocities are subjected to a random rotation during the SRD collision step anyway, and second, the system energy and velocities undergo random rescalings due to the thermostat (see Section 6.1.4).

The main advantage of the velocity Verlet algorithm is its conceptual and computational simplicity. In particular, the number of values one needs to store and access are small, so that the algorithm does not additionally constrain the system size one is able to simulate by requiring storage of otherwise unneeded values. Furthermore, since accessing memory that is not local to the GPU's computation unit costs a considerable amount of time, minimizing the amount of data needed to update a given polymer is beneficial for the simulation performance.

Toneian, "Multi-Particle Collision Dynamics Simulation of Viscoelastic Fluids", Footnote/citation numbers, references to sections and equations, and some mathematical symbols have been adapted.

6.3 Simulation Parameters

6.3.1 System Properties

Unless noted otherwise, the simulation parameters for results shown were as follows:

The primary system volume had dimensions $L_x = L_y = L_z = 30a_0$. The SRD rotation angle α_{SRD} was fixed at 2.27, corresponding to about 130°. The temperature was set to $k_BT = 1$, the MPC streaming time was $\Delta t_{\mathrm{MPCD}} = 0.1$. The statistical average number of MPC particles per collision cell was set to $N_c = 10$.

6.3.2 System Initialization

When initializing the simulation, $N_{\mathrm{MPCD}} := N_c L_x L_y L_z a_0^{-3}$ MPC particles are created in total. With N_{S} being the number of springs per MPC polymer, i.e. $N_{\mathrm{S}} + 1$ being the number of MPC particles per polymer, this populates the simulation volume with $N_{\mathrm{Polymer}} := N_{\mathrm{MPCD}} / (N_{\mathrm{S}} + 1)$ MPC polymers; the simulation parameters are chosen such that $N_{\mathrm{Polymer}} \in \mathbb{N}_+$.

[24] Gompper, Ihle, Kroll, and Winkler, *Multi-Particle Collision Dynamics: A Particle-Based Mesoscale Simulation Approach to the Hydrodynamics of Complex Fluids.*

[25] Kowalik and Winkler, "Multiparticle collision dynamics simulations of viscoelastic fluids: Shear-thinning Gaussian dumbbells", Section III.A.

[26] D. Frenkel and B. Smit. *Understanding Molecular Simulation. From Algorithms to Applications.* 2nd ed. Academic Press, 2002, Chapter 4.3.1.

[27] Frenkel and Smit, *Understanding Molecular Simulation*, Chapter 4.3.1.

[28] Frenkel and Smit, *Understanding Molecular Simulation*, Chapter 4.2.3.

[29] Frenkel and Smit, *Understanding Molecular Simulation*, Chapter 4.3.

For each MPC polymer, the position $\mathbf{r}_1$ of the first MPC particle is sampled randomly from a uniform distribution $U([0, L_x) \times [0, L_y) \times [0, L_z))$ over the primary simulation volume. For each subsequent MPC particle $i + 1$ of that same MPC polymer, the initial position $\mathbf{r}_{i+1}$ is set to be $\mathbf{r}_i + s\mathbf{X}$, where $\mathbf{X} \sim U\left([0, 1)^3\right)$, and s is a scaling factor that is described below. The thusly chosen $\mathbf{r}_i$ is rejected if it lies outside of the primary simulation volume. If this would not be done, the newly generated particle would be mapped onto a potentially very distant location due to the boundary conditions employed, which could create unphysically highly stretched polymer bonds. On the other hand, this rejection mechanism is cause for a relatively depleted zone around the borders of the primary simulation volume. However, this imbalance in the mass distribution is expected to average out after the warmup phase described below.

The scaling parameter s is chosen to be the root-mean-square bond length b in the case for dimers, since there, this quantity can be readily obtained from the spring constant and vice versa. [For larger polymers, $s = 1$ is set for historical reasons, which is however inconsequential since this still allows for the springs to reach their equilibrium state during simulation warmup.]

The initial velocities of the MPC particles are chosen randomly and independently, with each Cartesian component being drawn from a normal distribution with zero mean and unity variance. This immediately yields the Maxwell-Boltzmann distribution for the magnitudes of the velocities, which is the correct distribution in systems where there is no external force; for other systems, the warmup time defined below has to be chosen such that a steady state can develop during warumup. The magnitudes of the velocities, which depend on the fluid's temperature, are scaled from their initialization value to the physically correct one by the thermostat applied (see Section 6.1.4).

After the system has been set up by choosing the initial positions and velocities of all MPC particles, a number of the usual MPC simulation steps is performed in what is called the *warmup phase* of the simulation. The goal of these steps is to let the system evolve to a point where the artifacts introduced by the initialization algorithm described above have averaged out and a steady state is reached, so that measurements of quantities one is interested in can be expected to accurately represent the physical behavior of an ideally-prepared system. Consequently, all measurements are performed only after the warmup phase has concluded.

Toneian, "Multi-Particle Collision Dynamics Simulation of Viscoelastic Fluids", Footnote/citation numbers, references to sections and equations, and some mathematical symbols have been adapted, as has been the sentence in square brackets.

Chapter 7

OpenMPCD

7.1 Introduction

When the author started work on his *Diplomarbeit*, to the best of his knowledge, no publicly available code for MPCD was available. Hence, a new implementation of the simulation technique had to be written, which originally was called *MPCDSim*.

The intention has always been to produce a piece of software that would be useful not only to the author, but to a wide audience of people interested in MPCD, Molecular Dynamics, and the analysis of simulation data.

While the software is, of course, still far from perfect or complete, and, as with all sufficiently complex pieces of computer code, probably not free from bugs, it has improved considerably in terms of stability, versatility, and performance in the course of the present dissertation, and is now – after being renamed to *OpenMPCD*[1] – available to the interested reader as open source at `https://openmpcd.org`. The new name has been chosen in the style of many open sources projects, in hopes of conveying a sort of *openness*, in the sense that the software is free to use, modify, and distribute, and that contributions are very welcome. A software announcement paper for the peer-reviewed literature is in preparation.

[1] Toneian, *OpenMPCD*.

7.2 Overview

OpenMPCD consists of two parts: First, there is the simulation package, which performs the computer experiments using the Stochastic Rotation Dynamics (SRD) variant of MPCD, coupled with Molecular Dynamics (MD) to simulate complex MPCD fluids and/or solutes dissolved therein. The simulation package is written in object-oriented C++ and makes extensive use of *CUDA*, an extension of the C++ language (and others) that allows programs to be written to execute on *Graphics Processing Units* (*GPUs*).

The second part of OpenMPCD is a data analysis package, written in Python to facilitate easier and more interactive exploration of new simulation results, and more rapid development of scripts that combine tools provided by the OpenMPCD analysis library to transform and post-process simulation output.

7.3 Design Goals and Features

Whether or not, or to what extent, the following design goals have been achieved is open for judgment, but in developing OpenMPCD, the following principles have been kept in mind:

- **Correctness**
  As much as the subsequent design goals are beneficial for the developer and/or user of OpenMPCD, the utility of the software hinges on its ability to produce correct results, insofar the model, simulation technique, and computer characteristics allow.

  As has been said above, it is unlikely for a large program to contain no mistakes, but there are ways to reduce the likelihood of a significant error remaining undetected. In particular, care was taken to employ coding patterns that reduce possibilities for human error in developing or using the software, such as C++ exception handling, use of the "resource acquisition is initialization" (RAII) paradigm, debug assertions (i.e. "sanity checks" that are executed in debug builds, but not in production), and use of existing, high-quality libraries, like the C++ standard library, Boost, or Thrust.

Furthermore, the vast majority of the code is covered by *unit tests* and/or *integration tests* that are executed automatically as soon as changes to the OpenMPCD package are uploaded. This way, errors inadvertently introduced, or functionality not performing as to the specification, can be spotted early and corrected. In addition, the tests serve as secondary documentation, describing the intended behavior. While unit tests cover individual functions, the integration tests check physical properties, such as conservation of momentum and/or energy (depending on the simulation run), or statistical velocity distributions of particles in different flow profiles.

- **Modularity**
  In order to make the code more maintainable, and at the same time allow new developers to familiarize themselves with parts of the code without needing to understand its entirety at once, the software has been designed in a modular way.

  Classes that represent either physical objects, such as a particular type of solute, or encapsulate related functionality, such as GPU memory management, are decoupled from one another to a reasonable extent, and grouped into a descriptive hierarchy of namespaces. For example, the `OpenMPCD::CUDA::MPCSolute::StarPolymers::Instrumentation` namespace hosts functionality related to recording the state of a collection of star polymers (which are solutes, as opposed to the `MPCFluid`) in a CUDA-enabled simulation. These measurements, as well as others, are coordinated by the `OpenMPCD::CUDA::Instrumentation` class, which automatically calls the user's measurement code in regular intervals, and takes care of saving the results to disk at the end of the simulation.

  This modularity also allows users to add new functionality, such as a new kind of measurement, or a new kind of solute, by mimicking existing classes and registering them with the scheduling code.

- **Configurability**
  To provide not only developers, but also users, with comfort and flexibility, most simulation parameters can be set in a reasonably simple configuration file that is read at runtime, so that no re-compilation is necessary between simulations.

- **Documentation**
  Great care has been taken to document as much of the code as possible. In particular, almost all classes, functions, parameters and variables have been documented in the code via comments employing `Doxygen` syntax, which allows for automatic creation of HTML and/or LaTeX documentation, also available at `https://openmpcd.org`. Furthermore, descriptive names are chosen for all code entities to better convey the (intended) behavior of the program. Lastly, a short introduction has been written that serves as a starting point for new users, detailing the compilation and linking process, simple configuration, and execution of the software.

- **Parallelism and Performance**
  Since MPCD is, by construction, a very parallel algorithm, the code has been written with concurrent execution in mind. In particular, the use of parallel computing resources on GPUs, and in particular their high-bandwidth memory, provides for performance that is hard to achieve on CPUs alone.

- **Reproducibility**
  When looking at old data, one may find oneself wondering how these data came to be – what simulation parameters were used, were the data produced prior to fixing a significant error, have the data been included in a particular analysis?

  To avoid such questions, or provide easy answers to them, OpenMPCD offers multiple types of data provenance: First, the OpenMPCD simulation and analysis code is version-controlled via `git`, such that even very minor changes in the codebase are recorded in a way that allows exact reconstruction of the state of the sourcecode at a particular version. At the time of writing, OpenMPCD consists of well over 1500 such so-called *commits*.

  Second, simulation data produced by OpenMPCD is always saved along with the input configuration (and input state of solutes, if applicable), the `git` commit (i.e. the version) of the source code, and the seed used for the pseudo-random number generator. This enables the user to reproduce past simulation runs, although reproducibility is not perfect due to the fact that concurrent writes to shared (GPU) memory do not guarantee a particular order of execution, and floating-point arithmetic is not associative (i.e. the order two values are added to a third matters).

- **Convenience**

  In order to avoid repetitive tasks, the analysis part of the OpenMPCD package provides functionality that is commonly used in data analysis, such as routines for visualizing data, comfortable means of fitting data to models, querying simulation data and metadata, or performing statistical analysis of data, such as de-correlation of time series.[2,3,4]

  Also, tools are provided for creating and handling data, such that one can conveniently specify, in a few lines of Python code, that one wants to prepare a battery of simulations for all possible combinations of parameters A, B, and C, unless a sufficient number of data points have been gathered already, and submit that array of simulations to a central batch system for execution. Likewise, from all the simulations that have already been completed, one can easily filter all simulations that satisfy a certain set of conditions and use those in post-hoc data analysis.

7.4 Conclusions and Outlook

Having released the *OpenMPCD* simulation and analysis package as open source, the author hopes that it will prove useful to other researches, both those who intend to use functionality already implemented, as well as those who might want to extend the software to suit their needs. All kinds of contributions and feedback are, of course, most welcome.

Areas for improvements include the addition of support for new types of solutes and solvents, performance optimizations, and parallelization across multiple GPUs, possibly on multiple compute nodes (e.g. via MPI). This parallelization would allow one to simulate systems that are so large that the fluid does not fit into a single GPU's main memory, which is currently the main bottleneck limiting applicability of the code to complex simulation scenarios.

[2] D. R. Kent IV, R. P. Muller, A. G. Anderson, W. A. Goddard III, and M. T. Feldmann. "Efficient algorithm for "on-the-fly" error analysis of local or distributed serially correlated data". *Journal of Computational Chemistry* **28** (2007), 2309.

[3] H. Flyvbjerg and H. G. Petersen. "Error estimates on averages of correlated data". *The Journal of Chemical Physics* **91** (1989), 461.

[4] R. M. Lee, G. J. Conduit, N. Nemec, P. López Ríos, and N. D. Drummond. "Strategies for improving the efficiency of quantum Monte Carlo calculations". *Physical Review E* **83** (2011), 066706.

Appendix A

Notation and Mathematical Conventions

Definitions When defining a new quantity in terms of previously introduced quantities, the symbols := and =: are used. For example, if one wanted to define a new quantity X as the sum of the known objects g and h, one could synonymously write either

$$X := g + h \tag{A.1}$$

or

$$g + h =: X \tag{A.2}$$

Special Sets The set $\mathbb{N}_0$ is the set of natural numbers, including 0, and $\mathbb{N}_+$ is the set of natural numbers, excluding 0. $\mathbb{Z}$ is the set of integers. $\mathbb{R}$ is the set of real numbers, $\mathbb{R}_+$ is the set of real numbers greater than 0, and $\mathbb{R}_-$ is the set of real numbers smaller than 0. The set of complex numbers is denoted by $\mathbb{C}$.

The unit 2-sphere, that is the set of all points which lie a (Euclidean) distance 1 away from the center of the coordinate system, is denoted by

$$\mathbb{S}_2 := \left\{ \mathbf{r} \in \mathbb{R}^3 \mid |\mathbf{r}| = 1 \right\} . \tag{A.3}$$

Vectors Vectors are denoted by bold letters, such as $\mathbf{R}$ or $\mathbf{v}_i$, where i is part of the

symbol's name, e.g. in the case in situations where the index i serves to designate a particular particle's velocity. The components of a vector, usually with respect to a Cartesian coordinate system with axes x, y, and z, or synonymously 1, 2, and 3, are referred to as, for example, R_x or R_1, where no bold face is used. If the vector itself had an index, as in the case $\mathbf{v}_i$, the y-component of $\mathbf{v}_i$ is denoted by $v_{i,y}$ or equivalently $v_{i,2}$. The norm $|\mathbf{R}|$ of a vector is, unless noted otherwise, to be understood as the Euclidean norm:

$$|\mathbf{R}| := \sqrt{R_1^2 + R_2^2 + R_3^2} \tag{A.4}$$

The scalar product, or dot product, between two vectors $\mathbf{a}$ and $\mathbf{b}$, is denoted by $\mathbf{a} \cdot \mathbf{b}$, while the cross product is written $\mathbf{a} \times \mathbf{b}$.

Index notation Throughout this document, the *index notation* is used, along with the *Einstein summation convention* – that is, repeated indices are summed over, although the summation sign is suppressed. Partial derivatives with respect to time are denoted by ∂_t, while partial derivatives with respect to the spatial coordinate i are written as ∂_i.

Fourier transformation Unless noted otherwise, the Fourier transform of a function f is synonymously denoted by either $\tilde{f}$ or $\mathcal{F}\{f\}$. Similarly, the inverse Fourier transform of $\tilde{f}$ is written f or $\mathcal{F}^{-1}\left\{\tilde{f}\right\}$.

If it is desired to explicitly assign a symbol for the argument of the transformation's resultant function, the notation chosen is $\tilde{f}(\omega)$ or $\mathcal{F}\{f\}(\omega)$ for the Fourier transform, and $f(t)$ or $\mathcal{F}^{-1}\left\{\tilde{f}\right\}(t)$ for its inversion. It may be necessary to be specific about the argument that is transformed, e.g. to avoid ambiguity. In such a case, the notation $\tilde{f}(\mathbf{r},\omega) = \mathcal{F}_t\{f(\mathbf{r},t)\}(\mathbf{r},\omega)$ or $f(\mathbf{r},t) = \mathcal{F}_\omega^{-1}\left\{\tilde{f}(\mathbf{r},\omega)\right\}(\mathbf{r},t)$ is chosen.

While the arguments can, of course, be named arbitrarily, it is customary to call them $\mathbf{k}$ if the transformed argument of f is a (vector of) spatial coordinates $\mathbf{r}$, and ω if the transformed variable is the time t. In the definition of the Fourier transform and its inverse, the following convention, called *unitary angular frequency*

convention, is used:

$$\mathcal{F}\{f\}(\mathbf{k}) = \tilde{f}(\mathbf{k}) := (2\pi)^{-\frac{D}{2}} \int_{\mathbb{R}^D} f(\mathbf{r}) \exp(-\mathrm{i}\mathbf{k}\cdot\mathbf{r}) \,\mathrm{d}\, r^D\,, \tag{A.5}$$

$$\mathcal{F}^{-1}\left\{\tilde{f}\right\}(\mathbf{r}) = f(\mathbf{r}) = (2\pi)^{-\frac{D}{2}} \int_{\mathbb{R}^D} \tilde{f}(\mathbf{k}) \exp(\mathrm{i}\mathbf{k}\cdot\mathbf{r}) \,\mathrm{d}\, k^D\,. \tag{A.6}$$

Here, D is the dimension of the vector space the argument affected by the (inverse) Fourier transformation is an element of. Since the integration range is the entire $\mathbb{R}^D$, said function has to be defined at least in the cases where the transformed argument takes on values in $\mathbb{R}^D$.

Laplace transformation Similarly, the (unilateral) Laplace transform of a function f is denoted by $\hat{f}$ or $\mathcal{L}\{f\}$, while the inversion of the Laplace transform is written $\mathcal{L}^{-1}\left\{\hat{f}\right\}$. The arguments of the original and the transformed functions may be specified, if required, as in the case of Fourier transforms.

The arguments of $\hat{f}$ are usually named s if the transformed argument of f was the time t, and vice versa. The Laplace transform of f is defined by

$$\mathcal{L}\{f\}(s) = \hat{f}(s) := \int_{t=0}^{\infty} f(t) \exp(-st) \,\mathrm{d}\, t\,. \tag{A.7}$$

Special functions Given a complex number $z \in \mathbb{C}$ with $z = x + \mathrm{i}y$, $x \in \mathbb{R}$, $y \in \mathbb{R}$, the *real part* of z is denoted by $\mathrm{Re}(z) := x$, while the *imaginary part* is written as $\mathrm{Im}(z) := y$.

The convention and notation chosen for the *Heaviside step function* is

$$\Theta(x) := \begin{cases} 0, & x < 0 \\ \frac{1}{2}, & x = 0 \\ 1, & x > 0 \end{cases}. \tag{A.8}$$

The *floor function* is defined as

$$\lfloor x \rfloor := \max(\{z \in \mathbb{Z} \mid z \leq x\})\,. \tag{A.9}$$

The *gamma function*[1] is defined on $\mathbb{R}_+$ by

$$\Gamma(x) := \int_{y=0}^{\infty} y^{x-1} \exp(-y) \, \mathrm{d}\, y \,. \tag{A.10}$$

Probability Distributions and Sampling of Random Numbers The sampling of a random variable X from a given probability distribution function F is denoted by $X \sim F$.

Given an interval $I \subset \mathbb{R}$, the *uniform probability distribution* over the interval I is called $U(I)$.

The *gamma distribution*[2] has two parameters $a \in \mathbb{R}_+$, $b \in \mathbb{R}_+$ and is defined for $x \in \mathbb{R}$ by

$$f_\Gamma(x; a, b) := \frac{1}{b^a \Gamma(a)} x^{a-1} \exp\left(-\frac{x}{b}\right) \Theta(x) \,. \tag{A.11}$$

Toneian, "Multi-Particle Collision Dynamics Simulation of Viscoelastic Fluids", Footnote/citation numbers and references to sections and equations have been adapted.

[1] R. V. Hogg, J. W. McKean, and A. T. Craig. *Introduction to Mathematical Statistics*. 7th ed. Pearson, 2012, Chapter 3.3.

[2] Hogg, McKean, and Craig, *Introduction to Mathematical Statistics*, Equation (3.3.1).

Appendix B

Properties of the Fourier Transformation

B.1 Fourier Transformation of Derivatives

Given a function $f(\mathbf{r})$ and its Fourier transform $\tilde{f}(\mathbf{k})$, the inverse Fourier transform of $\tilde{f}(\mathbf{k})$is given by equation (A.6):

$$f(\mathbf{r}) = (2\pi)^{-\frac{D}{2}} \int_{\mathbb{R}^D} \tilde{f}(\mathbf{k}) \exp(\mathrm{i}\mathbf{k}\cdot\mathbf{r}) \, \mathrm{d}\, k^D \,. \tag{B.1}$$

Taking the derivative ∂_j of this equation with respect to the j-component of $\mathbf{r}$, one can write

$$\begin{aligned} \partial_j f(\mathbf{r}) &= (2\pi)^{-\frac{D}{2}} \int_{\mathbb{R}^D} \tilde{f}(\mathbf{k}) \, \partial_j \exp(\mathrm{i}\mathbf{k}\cdot\mathbf{r}) \, \mathrm{d}\, k^D \\ &= (2\pi)^{-\frac{D}{2}} \int_{\mathbb{R}^D} \tilde{f}(\mathbf{k}) \, \mathrm{i}k_j \exp(\mathrm{i}\mathbf{k}\cdot\mathbf{r}) \, \mathrm{d}\, k^D \,. \end{aligned} \tag{B.2}$$

Defining $g(\mathbf{r}) := \partial_j f(\mathbf{r})$ and comparing the equation above with (A.6), i.e.

$$g(\mathbf{r}) = (2\pi)^{-\frac{D}{2}} \int_{\mathbb{R}^D} \tilde{g}(\mathbf{k}) \exp(\mathrm{i}\mathbf{k}\cdot\mathbf{r}) \, \mathrm{d}\, k^D \,, \tag{B.3}$$

one sees that

$$\tilde{g}\left(\mathbf{k}\right) = \mathrm{i}k_j \tilde{f}\left(\mathbf{k}\right) . \tag{B.4}$$

B.2 Fourier Transform of 1 and the Dirac Delta Function

The Dirac delta function δ can be represented as[1]

$$\delta\left(t - t'\right) = \frac{1}{2\pi} \int\limits_{\omega=-\infty}^{\infty} \exp\left(\mathrm{i}\left(t - t'\right)\omega\right) \,\mathrm{d}\,\omega\,, \tag{B.5}$$

which, conversely, allows one to define the inverse Fourier transform of 1 via

$$\int\limits_{\omega=-\infty}^{\infty} 1 \cdot \exp\left(\mathrm{i}t\omega\right) \,\mathrm{d}\,\omega = 2\pi\delta\left(t\right). \tag{B.6}$$

Since the Dirac delta function is even in its argument, also the relation

$$\int\limits_{\omega=-\infty}^{\infty} \exp\left(-\mathrm{i}t\omega\right) \,\mathrm{d}\,\omega = 2\pi\delta\left(t\right) \tag{B.7}$$

holds.

Toneian, "Multi-Particle Collision Dynamics Simulation of Viscoelastic Fluids", Footnote/citation numbers and references to sections and equations have been adapted.

[1] F. W. J. Olver, D. W. Lozier, R. F. Boisvert, and C. W. Clark, eds. *NIST Handbook of Mathematical Functions*. Cambridge University Press, 2010, Equation (1.17.12).

Appendix C

Properties of the Laplace Transformation

C.1 Laplace Transformation of Derivatives

For a given function $f(t)$, let $g(t) := \partial_t f(t)$. Then, inserting $g(t)$ into equation (A.7), one can write for the Laplace transform of $g(t)$

$$\begin{aligned}\hat{g}(s) &:= \int_{t=0}^{\infty} g(t) \exp(-st)\, \mathrm{d}\, t \\ &= \int_{t=0}^{\infty} (\partial_t f(t)) \exp(-st)\, \mathrm{d}\, t \\ &= [f(t) \exp(-st)]_{t=0}^{\infty} - \int_{t=0}^{\infty} f(t) (\partial_t \exp(-st))\, \mathrm{d}\, t\,.\end{aligned} \tag{C.1}$$

Assuming that the upper boundary term tends to 0, i.e.

$$\lim_{t\to\infty} (f(t) \exp(-st)) = 0\,, \tag{C.2}$$

one arrives at the following expression for the Laplace transform of a derivative $g(t) := \partial_t f(t)$:

$$\begin{aligned}\hat{g}(s) &= -f(0) + s \int_{t=0}^{\infty} f(t) \exp(-st)\, \mathrm{d}\, t \\ &= s\hat{f}(s) - f(0)\,.\end{aligned} \tag{C.3}$$

C.2 Convolution Theorem

Given two functions $f(t)$ and $g(t)$ and defining their convolution to be

$$h(t) := \int_{\tau=0}^{t} f(\tau)\, g(t-\tau)\ \mathrm{d}\tau\,, \tag{C.4}$$

one can calculate the Laplace transform $\hat{h}(s)$ of $h(t)$ by insertion of equation (C.4) into the definition (A.7):

$$\begin{aligned}
\hat{h}(s) &:= \int_{t=0}^{\infty} h(t) \exp(-st)\ \mathrm{d}t \\
&= \int_{t=0}^{\infty} \int_{\tau=0}^{t} f(\tau)\, g(t-\tau) \exp(-st)\ \mathrm{d}\tau\ \mathrm{d}t \\
&= \int_{t=0}^{\infty} \int_{\tau=0}^{\infty} f(\tau)\, g(t-\tau) \exp(-st)\, \Theta(t-\tau)\ \mathrm{d}\tau\ \mathrm{d}t\,.
\end{aligned} \tag{C.5}$$

Interchanging the order of integration and defining $u(t) := t - \tau$ for a fixed τ, one can perform the change of integration variables $t \to u$,

$$\begin{aligned}
\mathrm{d}t &= \mathrm{d}u\,, \\
u(t=0) &= -\tau\,, \\
u(t=\infty) &= \infty\,,
\end{aligned} \tag{C.6}$$

so that

$$\begin{aligned}
\hat{h}(s) &= \int_{\tau=0}^{\infty} \int_{u=-\tau}^{\infty} f(\tau)\, g(u) \exp(-s(u+\tau))\, \Theta(u)\ \mathrm{d}u\ \mathrm{d}\tau \\
&= \int_{\tau=0}^{\infty} \int_{u=0}^{\infty} f(\tau)\, g(u) \exp(-s(u+\tau))\ \mathrm{d}u\ \mathrm{d}\tau \\
&= \int_{\tau=0}^{\infty} f(\tau) \exp(-s\tau)\ \mathrm{d}\tau \int_{u=0}^{\infty} g(u) \exp(-su)\ \mathrm{d}u \\
&= \hat{f}(s)\, \hat{g}(s)\ .
\end{aligned} \tag{C.7}$$

Toneian, "Multi-Particle Collision Dynamics Simulation of Viscoelastic Fluids", Footnote/citation numbers and references to sections and equations have been adapted.

Appendix D

Tensors

D.1 The Kronecker Tensor δ_{ij}

The Kronecker tensor δ_{ij} is defined such that

$$\delta_{ij} = \begin{cases} 1, & i = j \\ 0, & i \neq j \end{cases} . \tag{D.1}$$

Evidently, the Kronecker tensor is symmetric: $\delta_{ij} = \delta_{ji}$.

D.2 The Levi-Civita Tensor ε_{ijk}

The Levi-Civita tensor ε_{ijk} is defined as

$$\varepsilon_{ijk} = \begin{cases} 1, & (i,j,k) \text{ is an even permutation of } (1,2,3) \\ -1, & (i,j,k) \text{ is an odd permutation of } (1,2,3) \\ 0, & \text{else} \end{cases} . \tag{D.2}$$

Therefore, ε_{ijk} is anti-symmetric in all pairs of its indices, i.e. $\varepsilon_{ijk} = -\varepsilon_{jik}$, $\varepsilon_{ijk} = -\varepsilon_{kji}$, and $\varepsilon_{ijk} = -\varepsilon_{ikj}$.

D.3 Symmetric and Anti-Symmetric Parts of a Tensor

Any tensor T_{ij} of order 2 can be decomposed into a symmetric part $S_{ij} = S_{ji}$ and an anti-symmetric part $A_{ij} = -A_{ji}$:

$$T_{ij} = \underbrace{\frac{1}{2}\left(T_{ij} + T_{ji}\right)}_{=:S_{ij}} + \underbrace{\frac{1}{2}\left(T_{ij} - T_{ji}\right)}_{=:A_{ij}} . \tag{D.3}$$

Pairs of indices of higher-order tensors can be symmetrized (denoted by parentheses) and anti-symmetrized (denoted by square brackets) in an analogous manner; for example,

$$\begin{aligned} T_{i(jk)l} &:= \frac{1}{2}\left(T_{ijkl} + T_{ikjl}\right) \\ T_{i[jk]l} &:= \frac{1}{2}\left(T_{ijkl} - T_{ikjl}\right) . \end{aligned} \tag{D.4}$$

The contraction of the Levi-Civita tensor with a symmetric tensor S_{jk} of order 2 is 0. To prove this, let $a \in \{1,2,3\}$ be an arbitrary index. Furthermore, let $b \in \{1,2,3\} \setminus \{a\}$ and finally $c \in \{1,2,3\} \setminus \{a,b\}$. Then,

$$\begin{aligned} \varepsilon_{ajk} S_{jk} &= \varepsilon_{abc} S_{bc} + \varepsilon_{acb} S_{cb} \\ &= \varepsilon_{abc} S_{bc} - \varepsilon_{abc} S_{bc} = 0 . \end{aligned} \tag{D.5}$$

Contraction of the Levi-Civita tensor ε_{ajk} with an anti-symmetric tensor A_{jk}, on the other hand, gives

$$\begin{aligned} \varepsilon_{ajk} A_{jk} &= \varepsilon_{abc} A_{bc} + \varepsilon_{acb} A_{cb} \\ &= 2\varepsilon_{abc} A_{bc} = 2\varepsilon_{acb} A_{cb} . \end{aligned} \tag{D.6}$$

Therefore, for a general tensor T of order n, one obtains

$$\varepsilon_{ji_x i_y} T_{i_1 i_2 \ldots i_x i_y \ldots i_n} = \varepsilon_{ji_x i_y} T_{i_1 i_2 \ldots [i_x i_y] \ldots i_n} . \tag{D.7}$$

Toneian, "Multi-Particle Collision Dynamics Simulation of Viscoelastic Fluids", Footnote/citation numbers and references to sections and equations have been adapted.

Appendix E

Uniform Sampling from the 2-Sphere

There are various methods[1,2,3,4,5,6,7] that can be used to uniformly sample from the n-sphere $\mathbb{S}_n$ in general, and the 2-sphere $\mathbb{S}_2$ in particular. For this thesis, only the latter was relevant, and the following algorithm was used:

Let $X_1 \sim U([0,1])$ and independently $X_2 \sim U([0,1))$. Then, let $z := 2X_1 - 1$ and $\varphi := 2\pi X_2$, so that z is uniformly distributed over $[-1,1]$ and φ is uniformly distributed over $[0,2\pi)$. Finally, the Cartesian coordinates R_1, R_2, and R_3 of the uniformly sampled, random unit vector $\mathbf{R} \in \mathbb{S}_2$ are

$$\begin{aligned} R_1 &:= \sqrt{1-z^2}\cos(\varphi) \\ R_2 &:= \sqrt{1-z^2}\sin(\varphi) \\ R_3 &:= z\,. \end{aligned} \tag{E.1}$$

The implementation in *OpenMPCD* deviates from the algorithm just described in that no guarantee is given on whether the end points of the distribution function intervals have non-zero probability of being sampled. The reason for this is that the primitive random number generators provided by various operating systems and programming libraries do not agree whether either end point of the interval is part of the set of possible results. While it is mathematically possible to construct a function that has the same range of return values for any operating system or library used, it comes at a cost in computational efficiency.

> However, one can convince oneself that the question of whether the interval end points can be sampled is of little importance in practice: The computations were performed with IEEE-754[8,9] double-precision (i.e. 64-bit) arithmetic. One can roughly estimate the number of distinct floating point values in the interval $[0, 1]$: since there are about approximately 2^{64} distinct and finite floating point values, about half of which are positive, and since about half of the exponents are smaller than 0, there are of the order of $2^{62} \approx 4.6 \cdot 10^8$ representable numbers in $[0, 1]$, such that the addition or omission of the boundary points only has a negligible impact.

Toneian, "Multi-Particle Collision Dynamics Simulation of Viscoelastic Fluids", Footnote/citation numbers and references to sections and equations have been adapted, and the name "MPCDSim" has been replaced by "OpenMPCD".

[1] Y. Tashiro. "On methods for generating uniform random points on the surface of a sphere". *Annals of the Institute of Statistical Mathematics* **29** (1977), 295.

[2] G. Marsaglia. "Choosing a Point from the Surface of a Sphere". *The Annals of Mathematical Statistics* **43** (1972), 645.

[3] E. W. Weisstein. *Sphere Point Picking.* URL: `http://mathworld.wolfram.com/SpherePointPicking.html`.

[4] E. Allahyarov and G. Gompper. "Mesoscopic solvent simulations: Multiparticle-collision dynamics of three-dimensional flows". *Physical Review E* **66** (2002), 036702. Appendix.

[5] M. E. Muller. "A note on a method for generating points uniformly on n-dimensional spheres". *Communications of the ACM* **2** (1959), 19.

[6] J. M. Cook. "Rational formulae for the production of a spherically symmetric probability distribution". *Mathematics of Computation* **11** (1957), 81.

[7] J. S. Hicks and R. F. Wheeling. "An efficient method for generating uniformly distributed points on the surface of an n-dimensional sphere". *Communications of the ACM* **2** (1959), 17.

[8] *IEEE Standard for Floating-Point Arithmetic.*

[9] Goldberg, "What every computer scientist should know about floating-point arithmetic".

Appendix F

Notation in Polymer Literature

In Tables F.1 to F.3, a number of books and papers used in this thesis have (part of) their notation regarding polymer physics compared to one another and to the present text.

Description	this work	Doi[1]	Teraoka[2]	Rouse[3]	Forsman[4]
Number of springs	N_S	$N-1$ [5]	$N-1$ [6]	N [7]	n
Number of beads	$N_\mathrm{B}=N_\mathrm{S}+1$	N	N	$N+1$	$n+1$
Mean-squared bond length	b^2		b^2 [8]	$\sigma^2=\frac{3}{2}\beta$ [9]	$3/2n\beta^2$
Spring constant	K		k_sp [10]		
Friction coefficient per bead	ζ_B		ζ [11]		
Friction coefficient per normal mode	—		ζ_i [12]		
Inconsistencies		see footnote[13]	see footnote[14]		see footnote[15]

Table F.1: Comparison of notations in polymer literature

[1] M. Doi and S. F. Edwards. *The Theory of Polymer Dynamics.* Oxford University Press, 1994.
[2] I. Teraoka. *Polymer Solutions. An Introduction to Physical Properties.* John Wiley & Sons, 2002.
[3] P. E. Rouse. "A Theory of the Linear Viscoelastic Properties of Dilute Solutions of Coiling Polymers". *The Journal of Chemical Physics* **21** (1953), 1272.
[4] W. C. Forsman, ed. *Polymers in Solution. Theoretical Considerations and Newer Methods of Characterization.* Springer, 1986.
[5] M. Doi and S. F. Edwards. *The Theory of Polymer Dynamics.* Oxford University Press, 1994, Section 4.1.
[6] I. Teraoka. *Polymer Solutions. An Introduction to Physical Properties.* John Wiley & Sons, 2002, Section 3.4.
[7] P. E. Rouse. "A Theory of the Linear Viscoelastic Properties of Dilute Solutions of Coiling Polymers". *The Journal of Chemical Physics* **21** (1953), 1272. Last Paragraph on Page 1273.

Description	this work	Kalathi[16]	Lin[17]	Meyer[18]	Padding[19]
Number of springs	N_S	$N-1$ [20][21]	N_e-1 [22]	$N-1$ [23]	N [24]
Number of beads	$N_\mathrm{B}=N_\mathrm{S}+1$	N	N_e	N	$N+1$
Mean-squared bond length	b^2	b^2 [25][26]			b^2 [27]
Spring constant	K				k [28]
Friction coefficient per bead	ζ_B				ζ [29]
Friction coefficient per normal mode	—				
Inconsistencies					

Table F.2: Comparison of notations in polymer literature (continued)

[8] I. Teraoka. *Polymer Solutions. An Introduction to Physical Properties.* John Wiley & Sons, 2002, Implied in Paragraph 2 of Section 3.4.1.1.

[9] P. E. Rouse. "A Theory of the Linear Viscoelastic Properties of Dilute Solutions of Coiling Polymers". *The Journal of Chemical Physics* **21** (1953), 1272. End of first Paragraph on Page 1274.

[10] I. Teraoka. *Polymer Solutions. An Introduction to Physical Properties.* John Wiley & Sons, 2002, Section 3.4.

[11] I. Teraoka. *Polymer Solutions. An Introduction to Physical Properties.* John Wiley & Sons, 2002, Section 3.4.1.2.

[12] I. Teraoka. *Polymer Solutions. An Introduction to Physical Properties.* John Wiley & Sons, 2002, Equation (3.130).

[13] The Rouse relaxation time τ_R is used inconsistently, without distinguishing between stress and normal mode relaxation times, which, among other things, explains the appearance of the factor 2 in Equation (7.31).

[14] Equation (3.158) contains an error: it should read π^2 where it reads π.

[15] The relaxation times in Eq. (6.32) seem to be normal mode relaxation times, but they are used as stress relaxation times in Eq. (6.31).

[16] J. T. Kalathi, S. K. Kumar, M. Rubinstein, and G. S. Grest. "Rouse Mode Analysis of Chain Relaxation in Homopolymer Melts". *Macromolecules* **47** (2014), 6925. J. T. Kalathi, S. K. Kumar, M. Rubinstein, and G. S. Grest. "Rouse mode analysis of chain relaxation in polymer nanocomposites". *Soft Matter* **11** (2015), 4123.

[17] Y.-H. Lin. *Polymer Viscoelasticity. Basics, Molecular Theories, and Experiments.* 2nd ed. World Scientific, 2011.

[18] H. Meyer, J. P. Wittmer, T. Kreer, P. Beckrich, A. Johner, J. Farago, and J. Baschnagel. "Static Rouse modes and related quantities: Corrections to chain ideality in polymer melts". *The European Physical Journal E* **26** (2008), 25.

[19] J. T. Padding. *Theory of Polymer Dynamics.* lecture notes accompanying the Han-sur-Lesse 2005 Advanced Physical Chemistry course. 2005.

[20] J. T. Kalathi, S. K. Kumar, M. Rubinstein, and G. S. Grest. "Rouse Mode Analysis of Chain Relaxation in Homopolymer Melts". *Macromolecules* **47** (2014), 6925. Last Paragraph on Page 6925.

[21] J. T. Kalathi, S. K. Kumar, M. Rubinstein, and G. S. Grest. "Rouse mode analysis of chain relaxation in polymer nanocomposites". *Soft Matter* **11** (2015), 4123. Page 4125.

[22] Y.-H. Lin. *Polymer Viscoelasticity. Basics, Molecular Theories, and Experiments.* 2nd ed. World Scientific, 2011, Appendix 9.B, Page 171.

Description	this work	Rubinstein[30]
Number of springs	N_S	N [31]
Number of beads	$N_\mathrm{B} = N_\mathrm{S} + 1$	$N + 1$
Mean-squared bond length	b^2	b^2 [32]
Spring constant	K	k [33]
Friction coefficient per bead	ζ_B	ζ [34]
Friction coefficient per normal mode	—	
Inconsistencies		

Table F.3: Comparison of notations in polymer literature (continued)

[23]H. Meyer, J. P. Wittmer, T. Kreer, P. Beckrich, A. Johner, J. Farago, and J. Baschnagel. "Static Rouse modes and related quantities: Corrections to chain ideality in polymer melts". *The European Physical Journal E* **26** (2008), 25. Section 3.

[24]J. T. Padding. *Theory of Polymer Dynamics*. lecture notes accompanying the Han-sur-Lesse 2005 Advanced Physical Chemistry course. 2005. Section 2.3.

[25]J. T. Kalathi, S. K. Kumar, M. Rubinstein, and G. S. Grest. "Rouse Mode Analysis of Chain Relaxation in Homopolymer Melts". *Macromolecules* **47** (2014), 6925. Last Paragraph on Page 6925.

[26]J. T. Kalathi, S. K. Kumar, M. Rubinstein, and G. S. Grest. "Rouse mode analysis of chain relaxation in polymer nanocomposites". *Soft Matter* **11** (2015), 4123. Page 4125.

[27]J. T. Padding. *Theory of Polymer Dynamics*. lecture notes accompanying the Han-sur-Lesse 2005 Advanced Physical Chemistry course. 2005. Section 2.3.

[28]J. T. Padding. *Theory of Polymer Dynamics*. lecture notes accompanying the Han-sur-Lesse 2005 Advanced Physical Chemistry course. 2005. Section 2.3.

[29]J. T. Padding. *Theory of Polymer Dynamics*. lecture notes accompanying the Han-sur-Lesse 2005 Advanced Physical Chemistry course. 2005. Section 2.3.

[30]M. Rubinstein and R. H. Colby. *Polymer Physics*. 3rd ed. Oxford University Press, 2003.

[31]M. Rubinstein and R. H. Colby. *Polymer Physics*. 3rd ed. Oxford University Press, 2003, Section 2.3.

[32]M. Rubinstein and R. H. Colby. *Polymer Physics*. 3rd ed. Oxford University Press, 2003, Section 2.3.

[33]M. Rubinstein and R. H. Colby. *Polymer Physics*. 3rd ed. Oxford University Press, 2003, Section 2.3.

[34]M. Rubinstein and R. H. Colby. *Polymer Physics*. 3rd ed. Oxford University Press, 2003, Section 2.3.

Appendix G

License

[1] *Creative Commons Attribution 4.0 International (CC BY 4.0).* URL: `https://creativecommons.org/licenses/by/4.0/legalcode`.

List of Symbols

Special Symbols

$A!$	Factorial of A, i.e. $A \cdot (A-1) \cdot \ldots \cdot 2 \cdot 1$
$a := b$	Defines the left-hand side a in terms of the right-hand side b
$a =: b$	Defines the right-hand side b in terms of the left-hand side a
$\cdot$	Depending on the arguments, the inner product of two vectors, the product of two scalars, or the product of a scalar and a vector
$\times$	Cross product of two vectors
$\otimes$	Outer product, or tensor product, of two vectors
$\lvert A \rvert$	Absolute value of A (if a scalar), or the magnitude of A (if a vector)
$\langle A \rangle$	The expectation value of a random variable A
$\langle A \rangle_B$	The expectation value of a random variable A, given B
$X \sim N$	Denotes that a random variable X is sampled from the distribution N
$\lfloor x \rfloor$	Floor function applied to x
$\oint$	Surface integral
$\tilde{f}$	Fourier transform of a function f
$\hat{f}$	Laplace transform of a function f

Numbers

$\mathbb{1}$	Identity (or unity) matrix

Greek Letters

α	Asymmetry ratio in a telechelic star polymer
$\hat{\boldsymbol{\alpha}}$	Unit vector along the Cartesian α direction, with α being either x, y, or z
α_{FRC}	Fixed angle formed by three consecutive backbone atoms in the freely rotating chain (FRC) model
α_{SRD}	Collision angle in the Stochastic Rotation Dynamic (SRD) variant of the MPCD simulation technique
$\Gamma(x)$	Gamma function of argument x
$\dot{\gamma}$	Rate of strain tensor
$\dot{\gamma}$	Shear rate
$\dot{\gamma}^*(\hat{\mathbf{B}}, \lambda)$	Critical shear rate for the given direction $\hat{\mathbf{B}}$ of the external magnetic field and magnetic interaction strength λ
Δt_{MPCD}	Streaming time step in the MPCD simulation technique
δ	Dirac delta distribution (or function)
$\delta_{\alpha\beta}$	Kronecker symbol
ε	Levi-Civita symbol, cf. Appendix D.2
$\epsilon_{\alpha\beta}$	Energy scale of WCA potential for the interaction of two monomers (of types α and β, respectively) in the star polymer model
ϵ_{WCA}	The energy scale in the Weeks-Chandler-Andersen potential

ζ	Friction coefficient
ζ_{B}	Friction coefficient of a single bead in a polymer bead-spring model
$\zeta_{N_{\mathrm{B}}}$	Friction coefficient of a polymer with N_{B} beads
ζ_{S}	Second viscosity
η	Dynamic viscosity
η_{bare}	Dynamic viscosity of a bare MPCD fluid
$\Theta(x)$	The Heaviside step function, which takes on the values 0, 1/2, or 1, for $x < 0$, $x = 0$, and $x > 0$, respectively
θ	Opening angle of the cone on which the next backbone atom lies in the freely rotating chain (FRC) model
κ^2	Relative shape anisotropy
Λ_1^2	Smallest eigenvalue of the gyration tensor S
Λ_2^2	Middle eigenvalue of the gyration tensor S
Λ_3^2	Largest eigenvalue of the gyration tensor S
λ	Magnetic interaction strength parameter in the MFSP model
λ	Mean free path of a particle in MPCD simulations
ν	Kinematic viscosity
ϱ	Mass density of a system

σ_α	Soft-core radius of a monomer (of type α) in the star polymer model
σ_{WCA}	The length scale in the Weeks-Chandler-Andersen potential
$\tau_{\mathrm{S},i}$	i-th stress relaxation time of a Rouse polymer
$\tau_{\mathrm{X},p}$	p-th normal mode autocorrelation time in a Rouse polymer
$\tau^*(\hat{\mathbf{B}}, \lambda)$	Scaling time, dependent on the given direction $\hat{\mathbf{B}}$ of the external magnetic field and magnetic interaction strength λ, used to rescale MFSP shear rates
φ	Number of polymers per unit volume
χ_G	Orientational angle
$\boldsymbol{\omega}$	Angular velocity vector, with Cartesian components ω_x, ω_y, and ω_z
$\boldsymbol{\Omega}$	Eckart angular velocity vector, with Cartesian components Ω_x, Ω_y, and Ω_z

Latin Letters

A	Subscript denoting a star polymer's arm particle(s)
a_0	Unit length, and length of the collision cell, in the MPCD simulation technique
b	Asphericity
b	Root of the mean squared length of a polymer bond
b^2	Mean-squared length of a bond in a bead-spring polymer having only one type of spring
b_{FJC}	Fixed backbone bond length in the freely jointed chain (FJC) model
b_{FRC}	Fixed backbone bond length in the freely rotating chain (FRC) model
$\mathbb{C}$	Set of complex numbers
C	Subscript denoting a star polymer's core particle
$C_{\mathrm{v}}^{\mathrm{T}}$	Inverse Fourier-transform of autocorrelation of Fourier-transformed velocity vectors, with **k**-parallel part projected out
$\tilde{C}_{\mathrm{v}}^{\mathrm{T}}$	Autocorrelation of Fourier-transformed velocity vectors, with **k**-parallel part projected out
$\hat{\tilde{C}}_{\mathrm{v}}^{\mathrm{T}}$	Laplace-transform of autocorrelation of Fourier-transformed velocity vectors, with **k**-parallel part projected out
$C_{p,q}^{(X)}(t)$	Time-dependent autocorrelation of the p-th and q-th normal mode of a Rouse polymer
c	Acylindricity

D_t	Substantial derivative
D	Diffusion coefficient
D_α	Hard-core radius of a monomer (of type α) in the star polymer model
D_B	Diffusion coefficient of a single bead in a polymer bead-spring model
D_cm	Center-of-mass diffusion coefficient of a bead-spring polymer
D_FENE	FENE equilibrium distance
D_WCA	The distance offset in the modified Weeks-Chandler-Andersen potential
$\boldsymbol{\mathcal{E}}^{(i)}$	i-th Eckart frame vector, with components $\mathcal{E}_\alpha^{(i)}$
E_pot	Potential energy
$\boldsymbol{\mathcal{F}}^{(i)}$	i-th Eckart vector, with components $\mathcal{F}_\alpha^{(i)}$
$\mathcal{F}_t\left\{f\right\}(\omega)$	Fourier transform of a function f, taking the argument t to ω
$\mathcal{F}_\omega^{-1}\left\{f\right\}(t)$	Inverse Fourier transform of a function f, taking the argument ω to t
f	Number of arms per magnetically functionalized star polymer
f	Number of arms in a telechelic star polymer
f_Γ	Gamma distribution
$\mathcal{G}$	Three-dimensional Gram matrix, with components $\mathcal{G}_{ij}$
G	Relaxation Modulus
G'	Storage modulus
G''	Loss modulus
G^*	Complex modulus

$\mathcal{I}$	Eckart moment of inertia tensor, with Cartesian components $\mathcal{I}_{\mu\nu}$
$\mathbb{I}$	Index set enumerating MPCD particles
$\mathrm{Im}\,(A)$	Imaginary part b of the complex number $A = a + \mathrm{i}b$
I	Moment of inertia tensor, with Cartesian components $I_{\mu\nu}$
i	Imaginary unit, $+\sqrt{-1}$
K	Spring constant in a polymer bead-spring model
$K_{\alpha\beta}$	Energy scale of FENE potential for the interaction of two monomers (of types α and β, respectively) in the star polymer model
K_{FENE}	Spring constant in the FENE potential
K_{FJC}	Spring constant in the Hookean potential equivalent to the jointed chain (FJC) model's end-to-end vector distribution
$\mathbf{k}$	Fourier vector $\mathbf{k}$ with components k_α
k	Magnitude of the vector $\mathbf{k}$
k_{B}	Boltzmann's constant
$k_{\mathrm{B}}T$	Thermal energy
$\mathbf{k}_n$	Vector with integer components $k_{n,\alpha}$, related to the Fourier vector via $k_i = 2\pi k_{n,i}/L$, where L is the side length of the cubic simulation volume
$\lvert\mathbf{k}_n\rvert$	Magnitude of the vector $\mathbf{k}_n$

$\mathcal{L}_t\{f\}(s)$	Laplace transform of a function f, taking the argument t to s
$\mathcal{L}_s^{-1}\{f\}(t)$	Inverse Laplace transform of a function f, taking the argument s to t
$\mathbf{L}$	Angular momentum vector, with Cartesian components L_x, L_y, and L_z
L_α	Length of the primary MPCD simulation volume along the α Cartesian direction, if specified
L^2	Mean-squared magnitude of the end-to-end vector of a polymer
$l_{\alpha\beta}$	Equilibrium distance in the FENE potential for the interaction of two monomers (of types α and β, respectively) in the star polymer model
M	Subscript denoting a star polymer's magnetic particle(s)
MSD	Mean-squared displacement of a polymer, as its movement is tracked over time
m_G	Orientational resistance
m_i	Mass of particle i
m_{MPCD}	Unit mass in the MPCD simulation technique

$\mathbb{N}_+$	Natural numbers, excluding 0
$\mathbb{N}_0$	Natural numbers, including 0
N	Number of monomers per star polymer
N_A	Number of solvophilic monomers in each arm of a telechelic star polymer
N_B	Number of solvophobic monomers in each arm of a telechelic star polymer
N_B	Number of beads in a polymer, described in the bead-spring model
N_C	Number of magnetic clusters in a MSFP
N_c	Average number of MPCD particles in a collision cell
N_MPCD	Number of MPCD particles in a particular simulation
N_Polymer	Number of polymers in an MPCD simulation
N_S	Number of springs in a polymer, described in the bead-spring model
n	Degree of polymerization, in the context of a chemical description of a polymer
n_A	Number of arm particles per star polymer arm
$\mathrm{P}(A)$	The probability distribution for a random variable A
$\mathbf{p}_i$	The momentum vector for an object i, such as a monomer

$\boldsymbol{\mathcal{R}}^{(i)}$	i-th Eckart reference position vector, with components $\mathcal{R}_\alpha^{(i)}$
$\tilde{\mathcal{R}}^{(i)}$	i-th Eckart reference position vector in instantaneous Eckart frame
$\mathbb{R}$	Set of real numbers
$\mathbb{R}_-$	Set of strictly negative real numbers
$\mathbb{R}_+$	Set of strictly positive real numbers
$\mathbf{R}$	Vector from the first to the last monomer of a polymer, with components R_α
$\mathbf{R}$	Random rotation axis in the MPCD simulation technique
Re	Reynolds number
$\mathrm{Re}\,(A)$	Real part a of the complex number $A = a + \mathrm{i}b$
R	Distance from the first to the last monomer of a polymer
$R_{\alpha\beta}$	Maximum deviation from FENE equilibrium distance for the interaction of two monomers (of types α and β, respectively) in the star polymer model
R_{FENE}	Maximum elongation in the FENE potential
R_g	Radius of gyration
$\mathbf{r}_i$	Position vector for an object i, such as a monomer
$r_{i,\alpha}$	α-th Cartesian component of the position vector $\mathbf{r}_i$
$\mathbf{r}'_i$	Position of the periodic image of particle i in the MPCD simulation technique, with components $r'_{i,\alpha}$
$\mathbb{S}_2$	The two-sphere, i.e. the two-dimensional manifold of points in three dimensions with Euclidean distance of 1 to the origin
$\mathbb{S}_n$	The n-Sphere, i.e. the n-dimensional manifold obtained by generalizing the two-sphere $\mathbb{S}_2$
S	Gyration tensor
T	Thermodynamic temperature
t	Time
t_{MPCD}	Unit time in the MPCD simulation technique

$U([a,b])$	Uniform distribution in the range $[a,b]$, with each possible outcome being equally likely
$\mathbf{u}$	Flow field of the solvent
u_α	α component of the flow field of the solvent
$\mathrm{Var}(A)$	Variance of the random variable A
V_{FENE}	FENE potential
V_{FJC}	Hookean potential equivalent to the jointed chain (FJC) model's end-to-end vector distribution
V_{MPCD}	Volume of the primary simulation box in an MPCD simulation
V_{R}	Harmonic spring potential in the Rouse model
$V_{\mathrm{WCA}}(r)$	The (modified) Weeks-Chandler-Andersen (WCA) potential (cf. Eq. (2.13))
$\boldsymbol{\mathfrak{v}}_c$	Velocity of the center of mass of the MPCD collision cell c
$\boldsymbol{\mathfrak{v}}_i$	Velocity of particle i in the center-of-mass frame of its MPCD collision cell
$\mathbf{v}_i$	Velocity vector for an object i, such as a monomer
$\mathbf{v}'_i$	Velocity of the periodic image of particle i in the MPCD simulation technique, with components $v'_{i,\alpha}$
Wi	Weissenberg number, a dimensionless measure of shear rate
$\mathbf{X}_p$	p-th normal mode of a Rouse polymer
$\mathbb{Z}$	Set of integer numbers

Bibliography

Allahyarov, E. and Gompper, G. "Mesoscopic solvent simulations: Multiparticle-collision dynamics of three-dimensional flows". *Physical Review E* **66** (2002), 036702. DOI: 10.1103/physreve.66.036702.

Allen, M. P. and Tildesley, D. J. *Computer Simulation of Liquids*. Reprint by The Ipswich Book Co Ltd in 1991. Clarendon Press, 1987.

Batchelor, G. K. *An Introduction to Fluid Dynamics*. Cambridge Mathematical Library. Cambridge University Press, 2000.

Bateman Manuscript Project. *Tables of Integral Transforms*. Ed. by A. Erdélyi. Vol. 1. McGraw-Hill, 1954.

Beezer, R. A. *A First Course in Linear Algebra*. 3.50. Congruent Press, 2015.

Berthelot, D. "Sur le mélange des gaz". *Comptes rendus hebdomadaires des séances de l'Académie des Sciences* **126** (1898), 1703.

Bird, R. B., Armstrong, R. C., and Hassager, O. *Fluid Mechanics*. 2nd ed. Vol. 1. Dynamics of Polymeric Liquids. John Wiley & Sons, 1987.

Bird, R. B., Curtiss, C. F., Armstrong, R. C., and Hassager, O. *Kinetic Theory*. 2nd ed. Vol. 2. Dynamics of Polymeric Liquids. John Wiley & Sons, 1987.

Blaak, R. and Likos, C. N. "Self-assembly of magnetically functionalized star-polymer nanocolloids". *The European Physical Journal E* **41** (2018), 3. DOI: 10.1140/epje/i2018-11614-y.

Bois, J. *Rudiments of Polymer Physics*. 2002. URL: http://pimprenelle.lps.ens.fr/biolps/sites/default/files/teaching/4/poly_elast.pdf (visited on 2019-01-28).

Capone, B., Coluzza, I., Blaak, R., Lo Verso, F., and Likos, C. N. "Hierarchical self-assembly of telechelic star polymers: from soft patchy particles to gels and diamond crystals". *New Journal of Physics* **15** (2013), 095002. DOI: 10.1088/1367-2630/15/9/095002.

Capone, B., Coluzza, I., LoVerso, F., Likos, C. N., and Blaak, R. "Telechelic Star Polymers as Self-Assembling Units from the Molecular to the Macroscopic Scale". *Physical Review Letters* **109** (2012), 238301. DOI: 10.1103/physrevlett.109.238301.

Compendium of Chemical Terminology. Version 2.3.3. International Union of Pure and Applied Chemistry. 2014. DOI: 10.1351/goldbook. URL: https://goldbook.iupac.org/.

Cook, J. M. "Rational formulae for the production of a spherically symmetric probability distribution". *Mathematics of Computation* **11** (1957), 81. DOI: 10.1090/S0025-5718-1957-0690630-7.

Creative Commons Attribution 3.0 Unported (CC BY 3.0). URL: https://creativecommons.org/licenses/by/3.0/legalcode.

Creative Commons Attribution 4.0 International (CC BY 4.0). URL: https://creativecommons.org/licenses/by/4.0/legalcode.

Daoud, M. and Williams, C. E., eds. *Soft Matter Physics*. Springer, 1999.

Dhont, J. K. G., Gompper, G., Nägele, G., Richter, D., and Winkler, R. G., eds. *Soft Matter. From Synthetic to Biological Materials*. Vol. 1. Schriften des Forschungszentrums Jülich, Reihe Schlüsseltechnologien / Key Technologies. Forschungszentrum Jülich, 2008.

Dhont, J. K. G., Gompper, G., and Richter, D., eds. *Soft Matter: Complex Materials on Mesoscopic Scales*. Vol. 10. Matter and Materials. Forschungszentrum Jülich, 2002.

Doi. *Introduction to Polymer Physics*. Oxford University Press, 1996.

Doi, M. and Edwards, S. F. *The Theory of Polymer Dynamics*. Oxford University Press, 1994.

Durand, M., Meyer, H., Benzerara, O., Baschnagel, J., and Vitrac, O. "Molecular dynamics simulations of the chain dynamics in monodisperse oligomer melts and of the oligomer tracer diffusion in an entangled polymer matrix". *The Journal of Chemical Physics* **132** (2010), 194902. DOI: 10.1063/1.3420646.

Dyke, P. *An Introduction to Laplace Transforms and Fourier Series*. Ed. by M. A. J. Chaplain, K. Erdmann, A. MacIntyre, E. Süli, M. R. Tehranchi, and J. F. Toland. 2nd ed. Springer Undergraduate Mathematics Series. Springer, 2014. DOI: 10.1007/978-1-4471-6395-4.

Eckart, C. "Some Studies Concerning Rotating Axes and Polyatomic Molecules". *Physical Review* **47** (1935), 552. DOI: 10.1103/PhysRev.47.552.

Farago, J., Meyer, H., Baschnagel, J., and Semenov, A. N. "Mode-coupling approach to polymer diffusion in an unentangled melt. II. The effect of viscoelastic hydrodynamic interactions". *Physical Review E* **85** (2012), 051807. DOI: 10.1103/physreve.85.051807.

Ferry, J. D. *Viscoelastic Properties of Polymers*. 3rd ed. John Wiley & Sons, 1980.

Fixman, M. "Radius of Gyration of Polymer Chains". *The Journal of Chemical Physics* **36** (1962), 306. DOI: 10.1063/1.1732501.

Flyvbjerg, H. and Petersen, H. G. "Error estimates on averages of correlated data". *The Journal of Chemical Physics* **91** (1989), 461. DOI: 10.1063/1.457480.

Forsman, W. C., ed. *Polymers in Solution. Theoretical Considerations and Newer Methods of Characterization*. Springer, 1986. DOI: 10.1007/978-1-4899-0465-2.

Frenkel, D. and Smit, B. *Understanding Molecular Simulation. From Algorithms to Applications*. 2nd ed. Academic Press, 2002.

Frisch, U., Hasslacher, B., and Pomeau, Y. "Lattice-Gas Automata for the Navier-Stokes Equation". *Physical Review Letters* **56** (1986), 1505. DOI: 10.1103/PhysRevLett.56.1505.

Furlani, E. P. *Permanent Magnet and Electromechanical Devices. Materials, Analysis, and Applications*. 1st ed. Academic Press Series in Electromagnetism. Academic Press, 2001.

Goldberg, D. "What every computer scientist should know about floating-point arithmetic". *ACM Computing Surveys* **23** (1991), 5. DOI: 10.1145/103162.103163.

Gompper, G., Ihle, T., Kroll, D. M., and Winkler, R. G. *Multi-Particle Collision Dynamics: A Particle-Based Mesoscale Simulation Approach to the Hydrodynamics of Complex Fluids*. Advances in Polymer Science. Springer, 2008. DOI: 10.1007/12_2008_5.

Gompper, G. and Schick, M., eds. *Polymer Melts and Mixtures*. Vol. 1. Soft Matter. Wiley-VCH, 2006.

Grest, G. S., Kremer, K., Milner, S. T., and Witten, T. A. "Relaxation of Self-Entangled Many-Arm Star Polymers". *Macromolecules* **22** (1989), 1904. DOI: 10.1021/ma00194a065.

Hadjichristidis, N., Pitsikalis, M., Iatrou, H., Driva, P., Sakellariou, G., and Chatzichristidi, M. "Polymers with Star-Related Structures: Synthesis, Properties, and Applications". Ed. by K. Matyjaszewski and M. Möller. Vol. 6. Polymer Science: A Comprehensive Reference. Elsevier, 2012. Chap. 6.03, 29. DOI: 10.1016/B978-0-444-53349-4.00161-8.

Hamley, I. W. *Introduction to Soft Matter – Revised Edition. Synthetic and Biological Self-Assembling Materials*. John Wiley & Sons, 2007.

Hansen, J.-P. and McDonald, I. R. *Theory of Simple Liquids*. 2nd ed. Academic Press, 1990.

— *Theory of Simple Liquids*. 3rd ed. Academic Press, 2006.

Hicks, J. S. and Wheeling, R. F. "An efficient method for generating uniformly distributed points on the surface of an n-dimensional sphere". *Communications of the ACM* **2** (1959), 17. DOI: 10.1145/377939.377945.

Hogg, R. V., McKean, J. W., and Craig, A. T. *Introduction to Mathematical Statistics*. 7th ed. Pearson, 2012.

Hsiao, K.-W., Schroeder, C. M., and Sing, C. E. "Ring Polymer Dynamics Are Governed by a Coupling between Architecture and Hydrodynamic Interactions". *Macromolecules* **49** (2016), 1961. DOI: 10.1021/acs.macromol.5b02357.

Huang, C., Chatterji, A., Sutmann, G., Gompper, G., and Winkler, R. G. "Cell-level canonical sampling by velocity scaling for multiparticle collision dynamics simulations". *Journal of Computational Physics* **229** (2010), 168. DOI: 10.1016/j.jcp.2009.09.024.

Huang, C.-C., Sutmann, G., Gompper, G., and Winkler, R. G. "Tumbling of polymers in semidilute solution under shear flow". *Europhysics Letters* **93** (2011), 54004. DOI: 10.1209/0295-5075/93/54004.

IEEE Standard for Floating-Point Arithmetic. Institute of Electrical and Electronics Engineers. DOI: 10.1109/IEEESTD.2008.4610935.

Ihle, T. and Kroll, D. M. "Stochastic rotation dynamics: A Galilean-invariant mesoscopic model for fluid flow". *Physical Review E* **63** (2001), 020201. DOI: 10.1103/physreve.63.020201.

— "Stochastic rotation dynamics. I. Formalism, Galilean invariance, and Green-Kubo relations". *Physical Review E* **67** (2003), 066705. DOI: 10.1103/physreve.67.066705.

International Union of Pure and Applied Chemistry. *Compendium of Polymer Terminology and Nomenclature. IUPAC Recommendations 2008*. RSC Publishing, 2009.

Isihara, A. *Condensed Matter Physics*. Dover Publications, 2007.

Jackson, J. D. *Classical Electrodynamics*. 3rd ed. John Wiley & Sons, 1999.

Jaramillo-Cano, D., Formanek, M., Likos, C. N., and Camargo, M. "Star Block-Copolymers in Shear Flow". *The Journal of Physical Chemistry B* **122** (2018), 4149. DOI: 10.1021/acs.jpcb.7b12229.

Jeffreys, H. *Cartesian Tensors*. Cambridge University Press, 1931.

Jones, R. A. L. *Soft Condensed Matter*. 1st ed. Oxford University Press, 2002.

Jung, C. W. and Jacobs, P. "Physical and chemical properties of superparamagnetic iron oxide MR contrast agents: Ferumoxides, ferumoxtran, ferumoxsil". *Magnetic Resonance Imaging* **13** (1995), 661. DOI: 10.1016/0730-725X(95)00024-B.

Kalathi, J. T., Kumar, S. K., Rubinstein, M., and Grest, G. S. "Rouse Mode Analysis of Chain Relaxation in Homopolymer Melts". *Macromolecules* **47** (2014), 6925. DOI: 10.1021/ma500900b.

— "Rouse mode analysis of chain relaxation in polymer nanocomposites". *Soft Matter* **11** (2015), 4123. DOI: 10.1039/C5SM00754B.

Kent IV, D. R., Muller, R. P., Anderson, A. G., Goddard III, W. A., and Feldmann, M. T. "Efficient algorithm for "on-the-fly" error analysis of local or distributed serially correlated data". *Journal of Computational Chemistry* **28** (2007), 2309. DOI: 10.1002/jcc.20746.

Koks, D. *Explorations in Mathematical Physics*. 1st ed. Springer, 2006. DOI: 10.1007/978-0-387-32793-8.

Kowalik, B. and Winkler, R. G. "Multiparticle collision dynamics simulations of viscoelastic fluids: Shear-thinning Gaussian dumbbells". *The Journal of Chemical Physics* **138** (2013), 104903. DOI: 10.1063/1.4792196.

Kremer, K. and Grest, G. S. "Molecular dynamics (MD) simulations for polymers". *Journal of Physics: Condensed Matter* **2** (1990), SA295. DOI: 10.1088/0953-8984/2/S/045.

Kröger, M. "Simple models for complex nonequilibrium fluids". *Physics Reports* **390** (2004), 453. DOI: 10.1016/j.physrep.2003.10.014.

Lamura, A. and Gompper, G. "Numerical study of the flow around a cylinder using multi-particle collision dynamics". *The European Physical Journal E - Soft Matter* **9** (2002), 477. DOI: 10.1140/epje/i2002-10107-0.

Lamura, A., Gompper, G., Ihle, T., and Kroll, D. M. "Multi-particle collision dynamics: Flow around a circular and a square cylinder". *Europhysics Letters* **56** (2001), 319.

Landau, L. D. and Lifshitz, E. M. *Fluid Mechanics*. 2nd ed. Vol. 6. Course of Theoretical Physics. Pergamon Press, 1987.

Lee, R. M., Conduit, G. J., Nemec, N., López Ríos, P., and Drummond, N. D. "Strategies for improving the efficiency of quantum Monte Carlo calculations". *Physical Review E* **83** (2011), 066706. DOI: 10.1103/PhysRevE.83.066706.

Lees, A. W. and Edwards, S. F. "The computer study of transport processes under extreme conditions". *Journal of Physics C: Solid State Physics* **5** (1972), 1921.

Likos, C. N. "Effective interactions in soft condensed matter physics". *Physics Reports* **348** (2001), 267. DOI: 10.1016/S0370-1573(00)00141-1.

Lin, Y.-H. *Polymer Viscoelasticity. Basics, Molecular Theories, and Experiments*. 2nd ed. World Scientific, 2011.

Lo Verso, F. and Likos, C. N. "End-functionalized polymers: Versatile building blocks for soft materials". *Polymer* **49** (2008), 1425. DOI: 10.1016/j.polymer.2007.11.051.

Lorentz, H. A. "Ueber die Anwendung des Satzes vom Virial in der kinetischen Theorie der Gase". *Annalen der Physik* **248** (1881), 127. DOI: 10.1002/andp.18812480110.

Louck, J. D. and Galbraith, H. W. "Eckart vectors, Eckart frames, and polyatomic molecules". *Reviews of Modern Physics* **48** (1976), 69. DOI: 10.1103/RevModPhys.48.69.

Malevanets, A. and Kapral, R. "Mesoscopic model for solvent dynamics". *The Journal of Chemical Physics* **110** (1999), 8605. DOI: 10.1063/1.478857.

Marsaglia, G. "Choosing a Point from the Surface of a Sphere". *The Annals of Mathematical Statistics* **43** (1972), 645. DOI: 10.1214/aoms/1177692644.

Meyer, H., Wittmer, J. P., Kreer, T., Beckrich, P., Johner, A., Farago, J., and Baschnagel, J. "Static Rouse modes and related quantities: Corrections to chain ideality in polymer melts". *The European Physical Journal E* **26** (2008), 25. DOI: 10.1140/epje/i2007-10250-0.

Miao, M. S., Van Camp, P. E., Van Doren, V. E., Ladik, J. J., and Mintmire, J. W. "Conformation and electronic structure of polyethylene: A density-functional approach". *Physical Review B* **54** (1996), 10430. DOI: 10.1103/PhysRevB.54.10430.

Muller, M. E. "A note on a method for generating points uniformly on n-dimensional spheres". *Communications of the ACM* **2** (1959), 19. DOI: 10.1145/377939.377946.

Noguchi, H., Kikuchi, N., and Gompper, G. "Particle-based mesoscale hydrodynamic techniques". *Europhysics Letters* (2007). DOI: 10.1209/0295-5075/78/10005.

Oberhettinger, F. *Tables of Fourier Transforms and Fourier Transforms of Distributions*. Springer, 1990. DOI: 10.1007/978-3-642-74349-8.

Oberhettinger, F. and Badii, L. *Tables of Laplace Transforms*. Springer, 1973. DOI: 10.1007/978-3-642-65645-3.

Olver, F. W. J., Lozier, D. W., Boisvert, R. F., and Clark, C. W., eds. *NIST Handbook of Mathematical Functions*. Cambridge University Press, 2010.

Online Etymology Dictionary. *Polymer*. URL: https://www.etymonline.com/word/polymer (visited on 2019-01-16).

Padding, J. T. *Theory of Polymer Dynamics*. lecture notes accompanying the Han-sur-Lesse 2005 Advanced Physical Chemistry course. 2005.

Painter, P. C. and Coleman, M. M. *Essentials of Polymer Science and Engineering*. DEStech Publications, 2009.

Prudnikov, A. P., Brychkov, Y. A., and Marichev, O. I. *Integrals and Series. Inverse Laplace Transforms*. Vol. 5. Gordon and Breach Science Publishers, 1992.

Purcell, E. M. "Life at low Reynolds number". *American Journal of Physics* **45** (1977), 3. DOI: 10.1119/1.10903.

Ripoll, M., Winkler, R. G., and Gompper, G. "Star Polymers in Shear Flow". *Physical Review Letters* **96** (2006), 188302. DOI: 10.1103/PhysRevLett.96.188302.

— "Hydrodynamic screening of star polymers in shear flow". *The European Physical Journal E* **23** (2007), 349. DOI: 10.1140/epje/i2006-10220-0.

Rouse, P. E. "A Theory of the Linear Viscoelastic Properties of Dilute Solutions of Coiling Polymers". *The Journal of Chemical Physics* **21** (1953), 1272. DOI: 10.1063/1.1699180.

Rubinstein, M. and Colby, R. H. *Polymer Physics*. 3rd ed. Oxford University Press, 2003.

Sablić, J., Delgado-Buscalioni, R., and Praprotnik, M. "Application of the Eckart frame to soft matter: rotation of star polymers under shear flow". *Soft Matter* **13** (2017), 6988. arXiv: 1707.09170 [cond-mat.soft].

Sperling, L. H. *Introduction to Polymer Science*. 4th ed. John Wiley & Sons, 2006.

Tao, Y.-G., Götze, I. O., and Gompper, G. "Multiparticle collision dynamics modeling of viscoelastic fluids". *The Journal of Chemical Physics* **128** (2008), 144902. DOI: 10.1063/1.2850082. arXiv: 0802.2200 [cond-mat.soft].

Tashiro, Y. "On methods for generating uniform random points on the surface of a sphere". *Annals of the Institute of Statistical Mathematics* **29** (1977), 295. DOI: 10.1007/BF02532791.

Taslimi, F., Gompper, G., and Winkler, R. G. "Scaffold Structures by Telechelic Rodlike Polymers: Nonequilibrium Structural and Rheological Properties under Shear Flow". *Macromolecules* **47** (2014), 6946. DOI: 10.1021/ma501215t.

Teraoka, I. *Polymer Solutions. An Introduction to Physical Properties*. John Wiley & Sons, 2002.

Theodorou, D. N. and Suter, U. W. "Shape of Unperturbed Linear Polymers: Polypropylene". *Macromolecules* **18** (1985), 1206. DOI: 10.1021/ma00148a028.

Toneian, D. *OpenMPCD*. URL: https://openmpcd.org.

— "Multi-Particle Collision Dynamics Simulation of Viscoelastic Fluids". Diploma thesis. TU Wien, 2015.

Warner Jr., H. R. "Kinetic Theory and Rheology of Dilute Suspensions of Finitely Extendible Dumbbells". *Industrial & Engineering Chemistry Fundamentals* **11** (1972), 379. DOI: 10.1021/i160043a017.

Weeks, J. D., Chandler, D., and Andersen, H. C. "Role of Repulsive Forces in Determining the Equilibrium Structure of Simple Liquids". *The Journal of Chemical Physics* **54** (1971), 5237. DOI: 10.1063/1.1674820.

Weisstein, E. W. *Sphere Point Picking*. URL: http://mathworld.wolfram.com/SpherePointPicking.html.

Yamakawa, H. *Modern Theory of Polymer Solutions*. Electronic Edition. 2001. URL: http://www.molsci.polym.kyoto-u.ac.jp/archives/redbook.pdf (visited on 2019-01-18).

Yamakawa, H. and Takenao, Y. *Helical Wormlike Chains in Polymer Solutions*. 2nd ed. Springer, 2016. DOI: 10.1007/978-3-662-48716-7.

Yung, K. W., Landecker, P. B., and Villani, D. D. "An Analytic Solution for the Force Between Two Magnetic Dipoles". *Magnetic and Electrical Separation* **9** (1998), 39. DOI: 10.1155/1998/79537.

Ziherl, P. *Soft Matter Physics*. 2014. URL: http://www-f1.ijs.si/~ziherl/smt.pdf (visited on 2019-01-28).